Zarabi Golkhatmi, Sanaz; Asghar, Muhammad Imran; Lund, Peter D.

A review on solid oxide fuel cell durability : Latest progress, mechanisms, and study tools

Published in:
Renewable and Sustainable Energy Reviews

DOI:
10.1016/j.rser.2022.112339

Published: 01/06/2022

Document Version
Publisher's PDF, also known as Version of record

Please cite the original version:
Zarabi Golkhatmi, S., Asghar, M. I., & Lund, P. D. (2022). A review on solid oxide fuel cell durability : Latest progress, mechanisms, and study tools. *Renewable and Sustainable Energy Reviews*, *161*, 1-34. Article 112339. https://doi.org/10.1016/j.rser.2022.112339

Renewable and Sustainable Energy Reviews 161 (2022) 112339

Contents lists available at ScienceDirect

Renewable and Sustainable Energy Reviews

journal homepage: www.elsevier.com/locate/rser

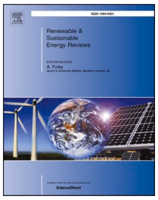

A review on solid oxide fuel cell durability: Latest progress, mechanisms, and study tools

Sanaz Zarabi Golkhatmi [a], Muhammad Imran Asghar [a,b,*], Peter D. Lund [a]

[a] *New Energy Technologies Group, Department of Applied Physics, Aalto University School of Science, P. O. Box 15100, FI-00076, Aalto, Espoo, Finland*
[b] *Faculty of Physics and Electronic Science, Hubei University, Wuhan, 430062, China*

ARTICLE INFO

Keywords:
Solid oxide fuel cell (SOFC)
Durability
Degradation mechanisms
Characterization techniques
Doping
Surface modification
Interface engineering

ABSTRACT

The commercial breakthrough of solid oxide fuel cells (SOFCs) is still hampered by degradation related issues. Most SOFCs that perform well do not possess good stability. To achieve a targeted degradation rate of 0.2%/1000 h important to a durable SOFC device, it is vital to identify the sources of degradation. So far, the longest stable performance was given by F1002-97, a short stack from Forschungszentrum Jülich GmbH, which reached 93,000 h of operation at 700 °C under 0.5 A cm^{-2} constant current density with a degradation rate of 0.5%/1000 h. In this review, we discuss the most detrimental degradation mechanisms for the core components of the SOFC, mainly poisoning, microstructural deformations, and strains. Electrochemical, chemical, and structural characterization tools for quantifying degradation mechanisms are also presented. The following section addresses the most recent progress in SOFC durability and the associated methods for analyzing degradation. These techniques include different doping techniques (including Mo, Nb, Co, Ce, Ta, Sn, etc.), surface modifications (e.g.infiltration, exsolution techniques, protective coatings), and interface engineering. Finally, the factors that inhibit the enhancement of SOFC durability are briefly discussed, such as inadequate knowledge of the degradation process and limitations in the material choices.

1. Introduction

The limited fossil fuel resources and their destructive impacts on the environment and climate in particular call for developing alternative sustainable energy sources [1–3]. In this regard, fuel cells are a promising power supply technology with significant efficiency, fuel flexibility nature, combustion-free operation, and almost zero-emission [1,4,5]. Fuel cells are also key elements in a hydrogen-based energy system.

A fuel cell converts the chemical energy in a fuel, such as H_2 and hydrocarbons, directly into electricity. The operation is comparable to batteries, except that fuel cells have gaseous electrodes; they do not require recharging and run as long as both fuel and oxidant are supplied to the electrodes [6–8]. Moreover, their efficiency is not limited by the Carnot cycle as in heat engines [9,10]. Generally, fuel cells are categorized by their electrolyte characteristics into six main groups: alkaline (AFC), phosphoric acid (PAFC), polymer electrolyte membrane (PEM), direct methanol (DMFC), molten carbonate (MCFC), and solid oxide (SOFC).

Among the different fuel cells, the SOFC is one of the most efficient technologies for power generation as it is flexible to fuel choice, noiseless, showing low CO_2 emissions, and has a potentially long lifetime of 40,000–80,000 h [8]. A SOFC typically employs yttrium-stabilized zirconia (YSZ) electrolyte. The cathode of the SOFC adsorbs oxygen molecules from the oxidant gas (air) and reduces them to negative oxygen ions. The chemical potential gradient passes these ions through the electrolyte to the anode fed by fuel. Then, the oxygen ions oxidize the diffused fuel catalytically leading to the generation of electrons. Finally, an external circuit transfers the released electrons to the cathode to complement the discharge process [11]. A schematic of a typical SOFC and its working principles is shown in Fig. 1.

The high working temperature of SOFC, necessary to reach an adequate ionic conductivity, provides excellent heat byproducts for combined cycle operations or co-generation of energy. Another merit is their solid-state electrolyte, which is manageable and does not cause corrosion to the cell or handling issues. Furthermore, SOFCs are cost-effective for mass production since they do not use expensive noble metals [7,8,13].

Considering SOFCs harsh operating conditions, such as high working temperatures, redox and thermal cycling, and poisonous atmosphere

---

[*] Corresponding author. New Energy Technologies Group, Department of Applied Physics, Aalto University School of Science, P. O. Box 15100, FI-00076, Aalto, Espoo, Finland.
E-mail address: imran.asghar@aalto.fi (M.I. Asghar).

https://doi.org/10.1016/j.rser.2022.112339
Received 4 October 2021; Received in revised form 18 January 2022; Accepted 28 February 2022

Abbreviations

Acronyms & Abbreviations	*Definition*
SOFC	Solid oxide fuel cell
AFC	Alkaline fuel cell
PAFC	Phosphoric acid fuel cell
PEM	Polymer electrolyte membrane fuel cell
DMFC	Direct methanol fuel cell
MCFC	Molten carbonate fuel cell
YSZ	Yttrium-stabilized zirconia
O–SOFC	Oxide-ion solid oxide fuel cell
GDC	Gadolinia-doped ceria
LSGM	$La_{0.8}Sr_{0.2}Ga_{0.8}Mg_{0.2}O_{3-\delta}$
H–SOFC	Proton conducting solid oxide fuel cell
BCZY	$BaCe_{0.7}Zr_{0.1}Y_{0.2}O_{3-\delta}$
LSM	$La_{1-x}Sr_{x}MnO_{3}$
LSCF	$La_{0.6}Sr_{0.4}Co_{0.2}Fe_{0.8}O_{3}$
NBCaCO	$NdBa_{1-x}Ca_{x}Co_{2}O_{5+\delta}$
BYC	$Ba_{2}YCu_{3}O_{6+\delta}$
BCFZY	$Ba_{x}Co_{0.4}Fe_{0.4}Zr_{0.1}Y_{0.1}O_{3-\delta}$
BFZB	$BaFe_{0.8}Zn_{0.1}Bi_{0.1}O_{3-\delta}$
PNOF	$Pr_{2}NiO_{3.9+\delta}F_{0.1}$
PBCT	$PrBaCo_{2-x}Ta_{x}O_{5+\delta}$
SDC	Samarium-doped ceria
SFM	$Sr_{2}FeMoO_{6-\delta}$
LSCM	$La_{0.7}Sr_{0.3}Cr_{0.5}Mn_{0.5}O_{3-\delta}$
CFCL	Ceramic Fuel Cells Limited
CHP	Combined Heats and Power
DOE	U.S. Department of Energy
ITM	Intermediate temperature metal
ASR	Area specific resistance
TPB	Triple-phase boundary
SIMS	Secondary Ion Mass Spectrometry
ORR	Oxygen reduction reaction
TEC	Thermal expansion coefficient
CGO	$Ce_{0.8}Gd_{0.2}O_{2-\delta}$
SSC	$Sm_{0.5}Sr_{0.5}CoO_{3-\delta}$
ScSz	$(ZrO_{2})_{0.90}(Sc_{2}O_{3})_{0.10}$
OCV	Open circuit voltage
ppb	Parts per billion
ppm	Parts per million
SS	Stainless Steel
LSCM	$La_{0.75}Sr_{0.25}Cr_{0.5}Mn_{0.5}O_{3-\delta}$
DTU	Denmark Technical University
CZBS	50 mol% CaO-20 mol% ZnO-20 mol% $B_{2}O3$-10 mol% SiO_{2}
TEM	Transmission electron microscopy
I–V	Current-voltage
EIS	Electrochemical impedance spectroscopy
DC	Direct Current
AC	Alternating current
LN	$La_{2}NiO_{4+\delta}$
PBSCF	$PrBa_{0.5}Sr_{0.5}Co_{1.5}Fe_{0.5}O_{5+\delta}$
LSCrN	$La_{0.6}Sr_{0.2}Cr_{0.85}Ni_{0.15}O_{3}$
SFGM	$Sr_{2}Fe_{1.3}Ga_{0.2}Mo_{0.5}O_{6-\delta}$
PNM	$PrNi_{0.5}Mn_{0.5}O_{3}$
XRD	X-ray diffraction
HTXRD	High-temperature XRD
FTIR	Fourier transform infrared spectroscopy
MS	Mass spectrometry
SFTM05	$Sr_{2}TiFe_{0.5}Mo_{0.5}O_{6-\delta}$
$SNCF_{x}$	$SrNb_{0.1}Co_{0.9-x}Fe_{x}O_{3-\delta}$
SNO	$Sr_{9}Ni_{7}O_{21}$
BFS	$BaFe_{0.95}Sn_{0.05}O_{3-\delta}$
XPS	X-ray photoelectron spectroscopy
ALD	Atomic layer deposition
NAP-XPS	Near ambient pressure-XPS
NEDO	New Energy and Industrial Technology Development Organization of Japan
SEM	Scanning electron microscopy
SE	Secondary electron
BSE	Back scattered electron
LSCrM	$La_{0.75}Sr_{0.25}Cr_{0.5}Mn_{0.5}O_{3-\delta}$
AFL	Anode functional layer
NBSCF	$NdBa_{0.5}Sr_{0.5}Co_{1.5}Fe_{0.5}O_{5-\delta}$
BSCF	$Ba_{0.5}Sr_{0.5}Co_{0.8}Fe_{0.2}O_{3-\delta}$
WDCM	Wet and dry cycling mode
AFM	Atomic force microscopy
FIB-SEM	Focused ion beam-SEM
TGA	Thermogravimetric analysis
DSC	Differential scanning calorimetry
DFT	Density functional theory
PBCO	$PrBaCo_{2}O_{5+\delta}$
CALPHAD	Calculation of phase diagrams
ESB	$Bi_{1.6}Er_{0.4}O_{3}$
icn-LSMESB	*in-situ* co-assembled nanocomposite LSM-$Bi_{1.6}Er_{0.4}O_{3}$
LCaF	$La_{0.65}Ca_{0.35}FeO_{3-\delta}$
FCC	face-centered cubic
LPG	liquid petroleum gas
LSCFM	$La_{0.6}Sr_{0.4}Co_{0.2}Fe_{0.7}Mo_{0.1}O_{3-\delta}$
Ce-GSCF	$Gd_{0.65}Sr_{0.35}(Co_{0.25}Fe_{0.75})_{0.9}Ce_{0.1}O_{3-\delta}$
BSF	$BaCo_{0.7}Fe_{0.3}O_{3-\delta}$
$EC_{x}BC$	$Eu_{1-x}Ca_{x}BaCo_{2}O_{5+\delta}$
SFNT	$SrFe_{0.8}Nb_{0.1}Ta_{0.1}O_{3-\delta}$
BCFZY	$Ba_{0.95}Ca_{0.05}Co_{0.4}Fe_{0.4}Zr_{0.1}Y_{0.1}O_{3-\delta}$
SC	$SrCoO_{3-\delta}$
PBC	$PrBa_{0.94}Co_{2}O_{5+\delta}$
LC	$LaCoO_{3-\delta}$
CFA	Co–Fe alloy
RP-SCFM	Ruddlesden–Popper structured oxide $Sr_{3}Co_{0.1}Fe_{1.3}Mo_{0.6}O_{7-\delta}$
NFA	Ni–Fe alloy
RP-PSNF	Ruddlesden-Popper $Pr_{0.32}Sr_{0.48}Ni_{0.2}Fe_{0.8}O_{3-\delta}$
ESB	$Bi_{1.6}Er_{0.4}O_{3}$
SNC	$SrNb_{0.1}Co_{0.9}O_{3-\delta}$
SSFTR7020	$Sm_{0.7}Sr_{0.2}Fe_{0.8}Ti_{0.15}Ru_{0.05}O_{3-\delta}$
SFHf	$SrFe_{0.9}Hf_{0.1}O_{3-\delta}$
SFCoM	$Sr_{1.95}Fe_{1.4}Co_{0.1}Mo_{0.5}O_{6-\delta}$
SLFC	Single-layer SOFCs

Variables & constants	*Definition & Unit*
ASR	Area specific resistance, Ω cm^{2}
P_{SO2}	Partial pressure of SO_{2}, Pa
P_{O2}	Partial pressure of O_{2}, Pa
TEC	Thermal expansion coefficient, K^{-1}
I	Current density, mA cm^{-2}
R_{P}	Polarization resistance, Ω
R_{Ω}	Ohmic resistance, Ω
R_{1}	Charge transport resistance, Ω
R_{2}	Catalytic reaction resistance, Ω
M	Molar, M
heating rate	°C/h
wt%	weight percentage
U	applied regime value for stability test
G	Galvanostatic regime for stability test, mA cm^{-2}
P	Potentiostatic regime for stability test, V
T	Temperature, °C
t	Duration, h
Power density	W m^{-2}/mW cm^{-2}
V	Voltage, V
A	Atmosphere

vol%	volume percent

Frequent Chemical Formula	*Full name*
$BaCeO_3$	Barium cerate(IV)
$BaZrO_3$	Barium Zirconate
Cr	Chromium
S	Sulfur
CO_2	Carbon Dioxide
Cr_2O_3	Chromium Trioxide
$CrO_2(OH)_2$	Chromium Dihydroxile
SO_2	Sulfur Dioxide
$SrSO_4$	Strontium Sulfate
Sr	Strontium
Co	Cobalt
$CoFe_2O_4$	Cobalt Iron Oxide
Fe	Iron
$La_2O_2SO_4$	Lanthanum Oxysulfates
$SrCrO_4$	Strontium Chromate
$SrCO_3$	Strontium Carbonate
$Sr(OH)_2$	Strontium Hydroxide
$SrZrO_3$	Strontium Zirconate
$BaCeO_3$	Barium Cerate(IV)
BaO	Barium Oxide
Y_2O_3	Yttrium Oxide
ZrO_2	Zirconium Oxide
Ni	Nickel
NiO	Nickel Oxide
CO	Carbon Monoxide
P	Phosphorous
As	Arsenic
Se	Selenium
Cl	Chlorine
Sb	Antimony
H_2S	Hydrogen Sulfide
Ni_xS_y	Nickel Sulfide
NiP	Nickel Phosphide
PH_3	Phosphane
AsH_3	Arsine
Ni_5As_2	Nickel Arsenide (V)
$Ni_{11}As_8$	Nickel Arsenide (VIII)
$NiCl_2$	Nickel Chloride
$LaCrO_3$	Lanthanum Chromate
Mn_3O_4	Manganese (II, III) Oxide
La_2O_3	Lanthanum (III) Oxide
Nd_2O_3	Neodymium Oxide
$NiFe_2O_4$	Nickel Ferrite
Sr_2SiO_4	Strontium Orthosilicate
$BaCrO_4$	Barium Chromate
$CuMn_2O_4$	Copper Manganese Oxide
CH_4	Methane
Li^+	Lithium-ion
Na^+	Sodium-ion
K^+	Potassium-ion
PrO_x	Praseodymium Oxide
TiS_2	Titanium Sulfide
FeS_2	Iron Sulfide
MoS_2	Molybden Sulfide
$Sr(OH)_2.8H_2O$	Strontium Hydroxide
$SrNiO_3$	Strontium Nitrate
Pd	Palladium
OH^-	Hydroxide ion
Mn	Manganese
Al_2O_3	Aluminium Oxide
Cr^{+6}	Chromium ion
Rh	Rhodium
Ag	Silver
Pt	Pelatinum
Au	Gold
Nb	Niobium
Ta	Tantalum
Sn	Tin
Ca	Calcium
Eu^{3+}	Europium ion
$O_o^{\times}$	RP-SCFM lattice oxygen
$V_o^{\bullet\bullet}$	RP-SCFM oxygen vacancy
Hf	Hafnium

[14], they require several properties for their components (cathode, electrolyte, anode, interconnect, sealant), including [7,15–17].

- Appropriate conductivity (Electrolyte must be an electronic insulator and providing a good ionic conductivity, while electrodes should show a promising electronic and ionic conductivity)
- Acceptable stability (Chemical, Thermal, Morphological, Mechanical)
- Good compatibility with other components (Chemically, Thermally, Mechanically)
- Porous structure for electrodes (for adequate gas transportation to reaction sites) and dense electrolyte (for preventing gas mixing)
- High electrical conductivity, perfect gas tightness, and high resistivity against oxidation, sulfation, and carbon deposition for interconnects
- Hermeticity and insulating nature for sealants

Besides, these requirements should be achieved in a cost-effective and easy-to-fabricate way. On account of these prerequisites, different materials are available for the SOFC application. In the case of oxide-ion SOFCs (O–SOFCs), electrolytes are composed of perovskite or fluorite structure with oxygen deficiency to provide oxygen pathways by oxygen vacancies. Zirconia-based (e.g., YSZ), ceria-based (e.g., gadolinia-doped ceria (GDC)), and lanthanum gallate-based (e.g., $La_{0.8}Sr_{0.2}Ga_{0.8}Mg_{0.2}O_{3-\delta}$ (LSGM)) [18] electrolytes are the most common examples for O–SOFCs. On the other hand, proton-conducting SOFCs (H–SOFCs) transport H^+ instead of O^{2-} and there is no generated water molecule at the anode side, which brings several advantages such as high performance at lower operating temperatures and better durability in using hydrocarbon fuels. For this type, $BaCeO_3$-, $BaZrO_3$-based perovskites, such as $BaCe_{0.7}Zr_{0.1}Y_{0.2}O_{3-\delta}$ (BCZY) [19], are the most popular electrolytes [20]. Cathodes are also different for O–SOFCs and H–SOFCs. O–SOFC cathodes are mainly perovskite- (ABX_3), like $La_{1-x}Sr_xMnO_3$ (LSM) and $La_{0.6}Sr_{0.4}Co_{0.2}Fe_{0.8}O_3$ (LSCF), and layered perovskite- ($AA'B_2O_{5+\delta}$), such as $NdBa_{1-x}Ca_xCo_2O_{5+\delta}$ (NBCaCO) [21] based cathodes, where A, A′, and B are cations but with different radius and X is an anion (mostly oxide) connected to cations [22]. Cathode function in H–SOFCs requires three charge carriers of O^{2-}, H^+, and e^- to show acceptable performance. Therefore, mixing the proton-conducting oxides with O^{2-} conductors can be the key to provide an effective electrode reaction [22]. $Ba_2YCu_3O_{6+\delta}$ (BYC) [23], $Ba_xCo_{0.4}Fe_{0.4}Zr_{0.1}Y_{0.1}O_{3-\delta}$ (BCFZY) [24,25], $BaFe_{0.8}Zn_{0.1}Bi_{0.1}O_{3-\delta}$ (BFZB) [26], $Pr_2NiO_{3.9+\delta}F_{0.1}$ (PNOF) [27], and $PrBaCo_{2-x}Ta_xO_{5+\delta}$ (PBCT) [28] are some of these examples. In terms of conventional anode material, there are generally Ni-, including Ni-YSZ [29], Ni-GDC [30], and Ni-Samarium-doped ceria (SDC)- based [31], and perovskite-based materials, such as $Sr_2FeMoO_{6-\delta}$ (SFM) [32], and $La_{0.7}Sr_{0.3}Cr_{0.5}Mn_{0.5}O_{3-\delta}$ (LSCM) [33].

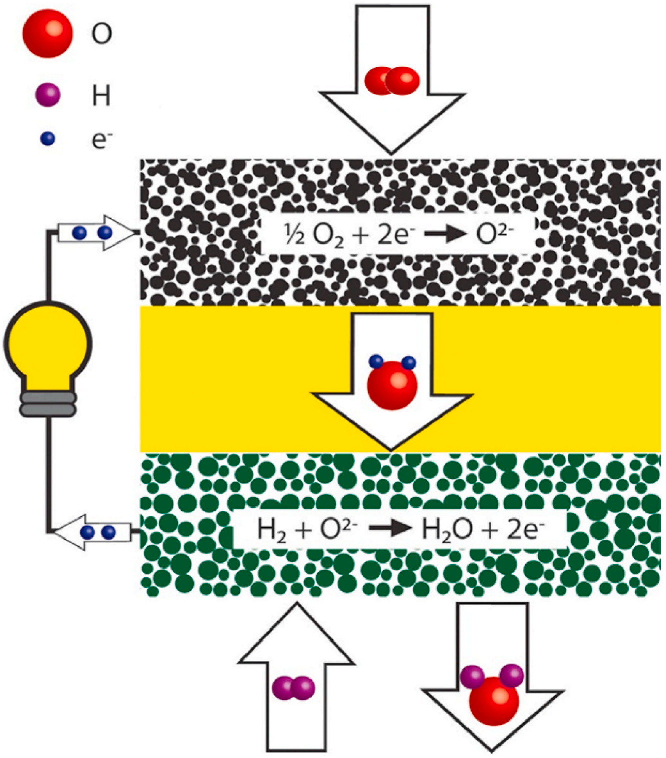

Fig. 1. Schematic of a typical SOFC and its working principles. Cathode, the top layer, reduces the Oxygen molecules of the oxidant gas to Oxygen ions. Then, the Oxygen anions (O^{2-}) pass through the electrolyte, the middle layer, to reach the anode, the bottom layer. The O^{2-} ions react with H_2, fed to the anode, and create water and generate electrons. Finally, these generated electrons are transferred to the cathode by the external circuit to complete the discharge process. Reprinted from Jouttijärvi et al. [12] (with minor edition) with permission. Copyright 2018, John Wiley and Sons.

Different companies have already begun the commercialization of SOFC for various purposes. For example, Bloom energy company (USA) has commercialized this technology for large stationary applications, while other companies such as JX Nippon Oil & Energy, Aisin (Japan), and Ceramic Fuel Cells Limited (CFCL) (Europe) have made the same effort on micro Combined Heats and Power (CHP) systems for small stationary applications [34]. In this regard, Ceres company (Europe) reported a degradation rate of ~1%/1000 h for its first pre-commercial small scale CHP [35]. However, high capital tariffs and expensive operating costs due to degradation issues are serious challenges for a commercial breakthrough of SOFC technology [36,37]. For instance, SOFC systems for stationary applications demand 40,000–80,000 h of service for market launch [38]. Several country departments, such as the U.S. Department of Energy (DOE), have set targets towards system capital costs and degradation rates to overcome these challenges. The degradation rate, which is the electrical potential lowering rate here [34], for 2020 was targeted at 0.2%/1000 h for SOFC stacks. In this regard, scientists of the field expect the average degradation rates of 0.5%/1000 h, 0.3%/1000 h, and 0.2%/1000 h for 2020, 2035, and 2050, respectively [36].

So far, the longest SOFC operation belongs to F1002-97, a short stack from Forschungszentrum Jülich GmbH, which reached 93,000 h of operation at 700 °C under 0.5 A cm^{-2} constant current density with 40% fuel utilization of wet H_2 and compressed air as oxidant [39]. This two-layer short stack consisted of a 500 μm-thick anode support (Ni-8YSZ; 8 mol% YSZ), a 7 μm-thick anode (Ni-8YSZ), a 10 μm-thick 8YSZ electrolyte, a 40 μm-thick LSCF cathode, and a 5 μm-thick GDC barrier layer. It also had a 5.5 mm intermediate temperature metal (ITM) interconnect with a MnO_x protective coating and glass sealants [40]. However, the average voltage degradation rate (0.5%/kh) crossed the given limit for SOFC commercialization [41], mainly due to the chromium (Cr) poisoned cathodes and interconnectors oxidation [42]. Besides, the stack was mostly run at a cell voltage of 0.7 V, which is much below the typical operating voltages for SOFCs [43]. There are also other stacks with long-term operations to study the durability performance of various SOFC components and design along with different working parameters [38], including ~ 40,000 h and 0.5–1%/kh by Mai et al., [44], 6000 h and ~1.4%/kh by Chou et al., [45] 5000 h and 0.75%/kh by Ido et al., [46] and 1000 h without any noticeable degradation by Thaheem et al. [47].

For achieving these durability targets, it is necessary to determine the origins of degradation and clarify the relevant mechanisms from the smallest working unit, which is the cell level. In the present study, we first briefly describe different SOFC configurations to better understand SOFC structures. Then, a comprehensive overview of the most critical degradation mechanisms in the main components of the SOFC, along with the study tools and limitations, are described, all in the cell level and lab scale. Finally, we discuss the most recent progress for enhancing SOFC stability.

2. SOFC structural configurations

Through different cell geometries for SOFC setup, planar and tubular designs are the most common configurations for practical applications, presented in Fig. 2 (a). The tubular cell consists of an array of sandwiched electrolyte and electrodes in a specific length and diameter. The planar design (radial or flat plate) includes a compact assembly of electrolyte and electrodes. The planar design has a simpler and cheaper fabrication procedure, higher power density, and low internal resistance due to its short current path. On the other hand, the tubular cell presents a more solid thermo-cycling performance, and it is easier to seal [48,49]. Both cell designs require sufficient mechanical strength to withstand the operation stresses provided by the support layer. The support layer has the largest thickness, and the thickness of other layers is minimized to avoid high internal resistance, enhance cell efficiency, and reduce costs. Generally, SOFCs have one support layer, and they can be designed as the anode-, cathode-, or electrolyte-supported [50,51], shown in Fig. 2 (b). Planar designs are mostly anode-supported, while tubular ones are fabricated in electrolyte-supported configuration [52]. In the planar SOFCs, the reactant gases diffuse into the porous microstructure from the center to the circumference. Unlike the planar ones, the fuel flow runs outside and the oxidant inside in a cathode-supported tubular cell.

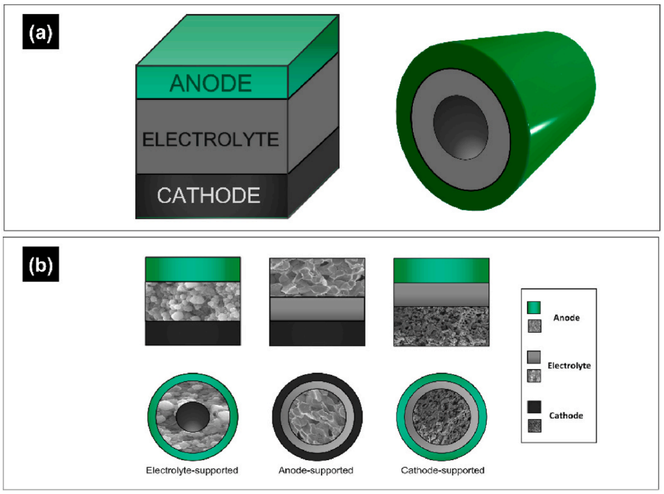

Fig. 2. SOFC geometries: (a) 3D model of the planar and tubular cell, (b) cross-sections of electrolyte-, anode-, and cathode-supported cells for both planar and tubular geometry.

For the anode-supported ones, the fuel flow goes inside, and the oxidant circulates outside in the tube during the operation [8,49,53].

Electrolyte-supported SOFCs are the oldest design as YSZ provides a robust support layer and is easier to fabricate. However, a thick electrolyte layer causes higher ohmic losses, which degrades the SOFC power density output. Regarding the electrode-supported cells, an anode-supported design is more favorable than a cathode-supported one, owing to its higher power densities, particularly at lower temperatures. The second generation is the anode-supported cells, with a 200–1500 μm anode thickness and a thin electrolyte. This design decreases electrolytic resistance and leads to better conductivity at lower temperatures. Since the electrolyte no longer provides mechanical support, other materials with higher ionic conductivity and lower mechanical strength can be replaced with the YSZ to improve the cell's output. Furthermore, anode-supported cells' fabrication process is simpler, and the anode microstructure is more controllable [50,51,54,55].

Although the industry is more interested in the anode-supported design, both anode- and electrolyte-supported cells are used in laboratory experiments. For instance, electrolyte-support allows for an easier independent analysis of each electrode process in a three-electrode operation, while the anode-support offers better output results [56].

Stacks also consist of several SOFC single cells joined to each other by interconnects. Interconnects act as a physical wall between the anode's reducing and cathode's oxidizing atmospheres. Planar and tubular stack designs are illustrated in Fig. 3. Moreover, planar design stacks require a sealant to avoid leakages or direct mixing of fuel and oxidant. Sealing, on the other hand, is typically not a major issue in tubular SOFCs [7].

It is worth noting that there is another geometry for SOFC stacks, the flat-tubular configuration, providing the features of both planar and tubular SOFCs into a single design, like high power density, good thermal robustness, and ease of sealing [58]. The Siemens-Westinghouse SOFC company invented this design to address the low power density of tubular cells [59–61]. Park et al. [62] reported a 5-cell stack with flat-tubular anode-supported cells without using metallic interconnect plates, showing a degradation rate of 0.69%/kh during 1093 h under a current load of 16 A at 750 °C. However, there are no records of their durability performance on the cell level [62].

3. Detailed degradation mechanisms

The severe working conditions of SOFC have several diverse degradation processes, which arise from each component and their interactions, making it challenging to fulfill the long-term stability requirements. Degradation is commonly characterized as loss of performance, and the degradation rate is generally stated as the voltage loss per 1000 h, especially in stacks. Change in area specific resistance (ASR) is another measure for reporting the degradation of single cells [63]. It should be noted that evaluating the degradation process in SOFC is quite complicated as long-term studies are needed, and the operation factors (temperature, fuel impurities, current density, etc.) affect the procedure [64]. Fig. 4 represents two photographs of degraded SOFCs after the performance. A summary of each cell component's main degradation mechanisms (cathode, electrolyte, anode) and a brief overview of stack elements (interconnects and sealants) is presented below.

3.1. Cathode

Cathode degradation mechanisms can be classified into three main groups [67]:

- *Poisoning (by Cr, S, CO_2, Humidity)*
- *Microstructural deformation*
- *Chemical and Thermal Strains (Delamination)*

The most rigorous degradation in LSCF cathodes is Cr poisoning, caused by the Cr evaporation from the unprotected metallic interconnects. Cr poisoning can happen in two potential ways for SOFC cathodes, chemical and electrochemical. In the chemical one, the volatile Cr species (CrO_3 or other gaseous kinds) directly counter the cathode surface and its segregated ions. Then, the resulted precipitated species not only corrupt the electrical properties but also hinder the gas pathways of the cathode. This mechanism increases the degradation effect of cathode material segregation as well. In the electrochemical mechanism, the triple-phase boundary (TPB) sites are inhibited by the deposition of reduced high valence volatile Cr species. These Cr_2O_3 or other low valence Cr kinds prevent the O_2 reduction at TPBs and O_2 diffusion in the cathode [68]. It is noteworthy that the operating conditions, including temperature, water vapor, and current density, can alter the Cr poisoning intensity. The temperature has the highest impact, and lower temperature causes more severe Cr poisoning. The humidity increase also increases the Cr poisoning effect since the $CrO_2(OH)_2$ is quite stable in this environment. The cathode degradation rate by this mechanism will rise with the current density increment [17].

Sulfur (S) poisoning in cathodes was first determined by Yukawa et al. [69] with Secondary Ion Mass Spectrometry (SIMS) and is not as well-known as Cr poisoning. They have figured out that the S deposition within cathode material was strongly associated with the cathode high overpotentials. A possible cause of this case is the trace amount of SO_2 in the air that may deposit by interacting with the cathode near the air inlet of cells. While the SO_2 content is just in the ppm scale, it still can affect the cell/stack performance and reduces the SOFC operation length [70]. In LSCF cathodes, S poisoning leads to the fine grain $SrSO_4$ precipitation in the grain boundaries of the cathode/electrolyte interface [71]. This

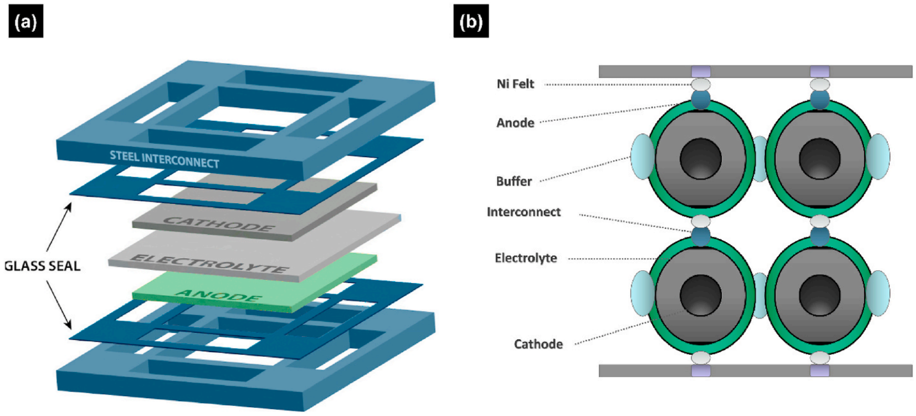

Fig. 3. Illustrations of (a) planar, adopted from Grayson, K [57]. with color modification, and (b) tubular design stacks, adopted from Hossain et al., [20] with modifications. Copyright 2017. Elsevier.

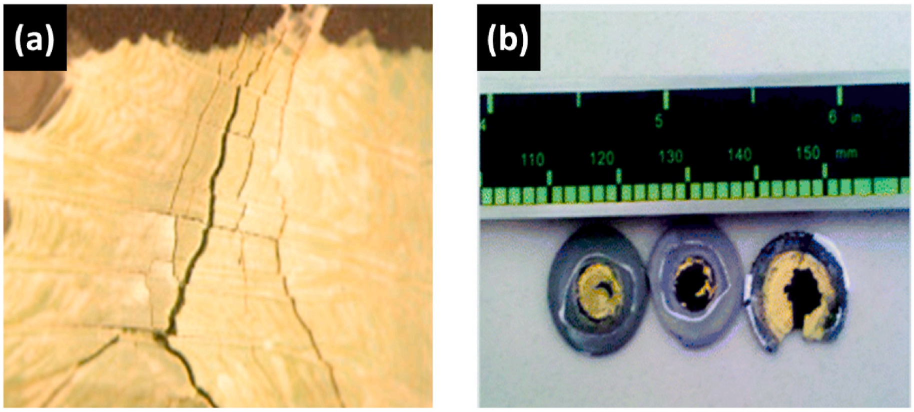

Fig. 4. (a) a cracked electrolyte after anodic re-oxidation, Reprinted from Batfalsky et al., [65] with permission. Copyright 2016. Elsevier. (b) Ni-YSZ|YSZ|LSM anode supported button cell after 120 h of operation in 50 ppm H_2S sour fuel. Reprinted from Cao et al., [66]. Copyright 2020. Royal Society of Chemistry.

$SrSO_4$ deposition can also happen on the cathode surface with a homogenous distribution [72]. Hence, the S poisoning causes Oxygen reduction reaction (ORR) degradation since the Sr and Co components of the cathode material are decreased by the formation of $SrSO_4$ and precipitation of $CoFe_2O_4$. The electrochemically active surface area is also reduced due to the formation of secondary phases such as $SrSO_4$, $La_2O_2SO_4$, Co oxide, and $Co_2Fe_2O_4$ among SO_2 adsorption by cathode surface particles. Fig. 5 presents a schematic of S poisoning in LSCF cathodes in dry conditions [73]. Several parameters, including temperature, P_{SO2}, Sr content, and P_{O2}, affect the S poisoning process. It is worth mentioning that S poisoning is more complex than Cr poisoning as in the first case, S oxidation and Co/Fe reduction are happening at the same time, but there is no oxidation reaction in Cr poisoning [70]. Perovskite surface can also adsorb the CO_2, causing carbonate formation on the surface, increased polarization, reduction in O_2 adsorption, and ORR activity. The cathode's electrocatalytic properties are also impressed by the competition between O_2 and CO_2 adsorption on the cathode surface, determining the catalytic efficiency [74].

The change in the cathode morphology is another degradation mechanism that occurs under the cathodic overpotential and alters the cathode microstructure. This phenomenon usually happens when the cathode has cations with much different mobility, leading to component separation, called "Kinetic Demixing" [17]. Sr segregation is a kind of kinetic demixing that can happen in cathode surface and cathode/electrolyte interface LSCF and LSC cathode materials [75–77]. Sr segregation in the surface can change the cathode surface chemistry, affecting the oxygen exchange kinetics and reducing ORR reactions [77, 78]. Furthermore, these Sr species can react with surrounding gaseous phases such as Cr, CO_2, and humidity, forming insulating layers of $SrCrO_4$, $SrCO_3$, and $Sr(OH)_2$ [79]. The $SrCrO_4$ formation also causes Sr deficiency at the A-site, which reduces ORR activity. Further, this Sr reduction in perovskite lattice degrades the electrical conductivity as well [79]. Sr enrichment in the interface can react with YSZ and results in insulating phases such as $SrZrO_3$, which induces the increment in the cell's ohmic resistance [75].

Particle coarsening in high-temperature SOFC can also cause performance degradation because the reduced absorbent surface area increases the polarization resistance [80]. The chemical strain is also a degradation mechanism in cathode material due to the oxygen non-stoichiometry. With the formation of oxygen vacancies in the lattice, the B-site cations' overall valance number reduces. This reduction enlarges the B-site ionic radius and causes lattice expansion, resulting in a thermal expansion coefficient (TEC) mismatch between the cathode and the electrolyte. If the mismatch becomes too large, the electrolyte will be broken by bending [17]. Besides, this difference in TEC can induce the applied thermal stress during the operation and results in component delamination. Delamination makes severe issues due to the prolonged current pathway, hindering charge conduction, and destruction of reaction sites. When delamination happens, the current is localized in an intact area. This current localization contributes to higher cathode loss of activation, and higher ohmic loss of electrolyte as well [81].

Surface engineering is a functional and economical technique to deal with cathode poisoning, using a protection layer against Cr diffusion. Doping is another strategy to address this issue, enhancing the chemical and structural stability of the cathode material towards poisonous species. These techniques are already discussed in the state-of-the-art section in detail. Operation conditions are essential in controlling and inhibiting the degradation process in cathodes as well. It is suggested to run the cell at moderate temperature and at low polarization to prevent any major over-potential and further deterioration of the cathode [67]. A functional interlayer such as $Ce_{0.8}Gd_{0.2}O_{2-\delta}$ (CGO) can slow down the Sr diffusion from the cathode through the electrolyte if the barrier is dense enough [82]. In the case of S poisoning, there are several ways to address this issue and enhance SOFC lifetime. S content can be reduced by applying a chemical filter for the air inlet of the SOFC system. Moreover, a trapping layer on the cathode surface can catch the SO_2 and prevents degradation. Some additives such as $Sm_{0.5}Sr_{0.5}CoO_{3-\delta}$ (SSC)

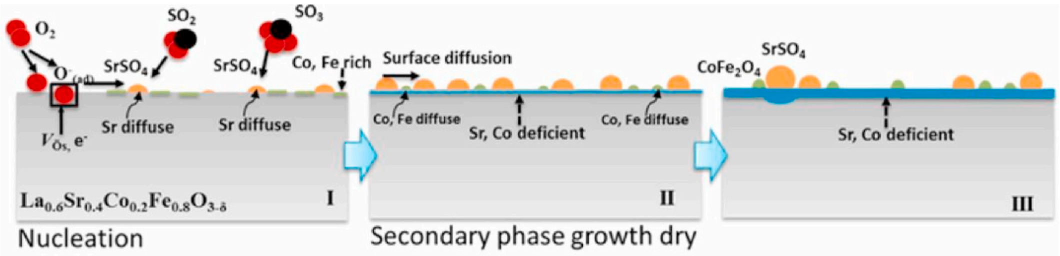

Fig. 5. Schematic of S poisoning mechanism and formation of $SrSO_4$ and $CoFe_2O_4$ secondary phases. Reprinted from Budiman et al., [73] with permission. Copyright 2019. IOP Publishing.

nanofibers, $BaCeO_3$ and BaO, modify the cathode by surface engineering and become more resistant to S poisoning [83–86].

3.2. Electrolyte

The main degradation mechanisms in the SOFC electrolyte can be listed as [37]:

- *Phase Transition, impurities, and dopant diffusion*
- *Mechanical failures*

During the SOFC operation at high temperatures and harsh atmosphere, a phase change in the electrolyte layer can affect the SOFC performance by reducing the ionic conductivity and phase stability, which eventually causes degradation. YSZ, as the most common electrolyte for SOFC, presents a competitive ion conductivity over a broad range of partial oxygen pressure, good stability under harsh operating conditions, and satisfying mechanical properties under elevated temperatures. However, several microstructural changes due to the long exposure at 1000 °C degrade the electrolyte conductivity and SOFC performance. The most notable phenomenon is the phase transformation from cubic to tetragonal zirconia, which strongly depends on the Y_2O_3 concentration in ZrO_2 [87,88]. Due to Hatturi et al. [89] research, 9.5YSZ was the optimized electrolyte because of its high conductivity and excellent stability compared with 8, 8.5, 9, 10YSZ electrolytes [89]. Ionic conductivity faced a decreasing trend with higher dopant content, as the emerging of point defects lowers the defect mobility [16]. Phase transition is also a challenge in Sc_2O_3-stabilized ZrO_2 (ScSZ) electrolyte, a proper candidate for low-to-intermediate temperatures operation, which experiences a cubic-rhombohedral-cubic phase transformation at lower temperatures [16,90]. As the rhombohedral phase has a weaker ionic conductivity, the cell faces an increase in the ASR, causing lower performance [16]. This transition causes unwanted residual stress in the SOFC stack as well [91].

Furthermore, chemical interactions between the electrolyte and its contacted components, especially cathode, are another source of degradation. The chemical interactions give rise to the formation interface and insulating secondary phases [92,93]. In the LSCF/YSZ systems, both the high-temperature sintering process and cathodic polarization cause Sr segregation and $SrZrO_3$ formation, which is undesirable for the SOFC performance and durability. In the case of LSCF/GDC systems, the Sr segregation rate is much slower and less destructive than the one in YSZ. However, limited and isolated Co accumulation happens here, which, of course, is not as damaging as Sr segregation. Fig. 6 (a) and (b) compare the interface reaction in both LSCF/YSZ and LSCF/GDC systems, respectively [92]. Due to the better chemical stability of GDC, a barrier layer from this material may enhance the stability and electrochemical properties of the YSZ-based systems. Still, a highly resistive Ce–Zr solid solution phase forms at the GDC/YSZ interface in elevated sintering temperature above 1300 °C, inducing a severe degradation in SOFC [94]. It should be mentioned that the ceria-based electrolytes may suffer from chemical stability and introducing electronic conduction as Ce^{4+} reduces to Ce^{3+} at low oxygen partial pressure, making an electrical short-circuit at once with dropping the overall efficiency and decreasing the open circuit voltage (OCV) [16,95]. The reaction between the LSGM electrolyte and cathode material is not similar to the one in YSZ or GCD electrolytes and generally takes place through the interdiffusion of cations rather than forming a secondary phase [96]. Considering the beneficial role of Co, Fe, and Ni interdiffusions for electrolyte performance, this small amount of interdiffusion is not detrimental.

Nevertheless, extreme interdiffusion will cause degradation in both cathode and electrolyte performance. Therefore, applying a ceria protection layer between the LSGM electrolyte and LSC cathode may stop the Co interdiffusion. But then again, the formation of an insulating phase can cause degradation [16]. Electrolyte/anode chemical reactions are less severe than electrolyte/cathode ones. Ni-YSZ, as the most common anode material, has no problems with the YSZ electrolyte. Nonetheless, the formation of a resistive layer may occur between LSGM and Ni-based anodes and causes SOFC degradation [16].

The last degradation mechanism in the SOFC electrolyte is mechanical failures resulting from thermal and chemical stresses. SOFCs are almost stress-free at high working temperatures, but the cooling down to room temperature causes residual stresses due to the difference in TECs of cathode/electrolyte or anode/electrolyte [93]. This residual stress introduces the crack initiation or delamination, which eventually leads to mechanical failure [97]. Fig. 7 illustrates an SEM micrograph of a partially delaminated YSZ electrolyte and NiO/YSZ anode [98]. Phase

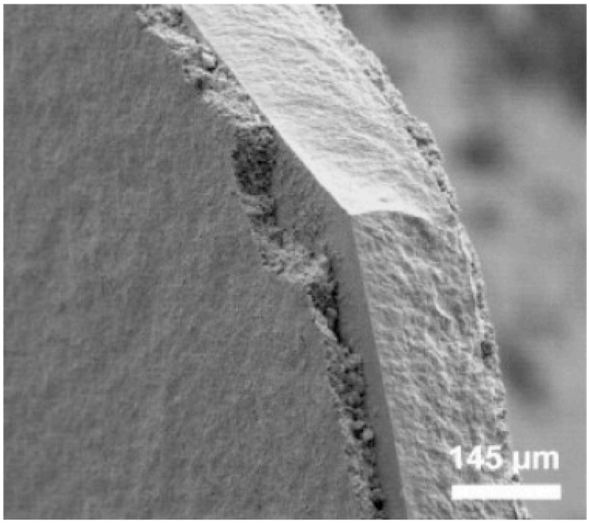

Fig. 7. Delamination SEM image of a partially delaminated anode layer on YSZ electrolyte. Reprinted from Selcuk et al., [98] with permission. Copyright 2001. Springer Nature.

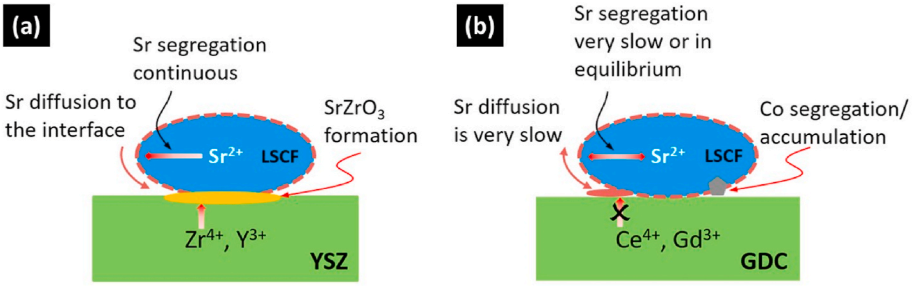

Fig. 6. Schemes of the surface segregation and interface reaction in (a) LSCF/YSZ and (b) LSCF/GDC cells. The red arrow indicates the Sr segregation, diffusion, and reaction direction. Reprinted from Sun et al., [92] with permission. Copyright 2021. Elsevier.

transformations are also responsible for residual stresses, like the phase changes of ScSZ that experiences a partial cubic to rhombohedral and back to cubic transformation through the heating range of 300–500 °C [91]. The difference in TEC between YSZ and GDC layers is also another example of delamination and mechanical degradation [94].

Another source of mechanical failure in the SOFC electrolyte is chemical stress induced by the chemical environment of the SOFC operation. The oxidation of Ni-based anodes and the resulted volume change is probably the most crucial example of chemical stress. The penetration of unwanted oxygen to the anode, either due to system leakage or uncontrolled fuel utilization, causes irreversible expansion of Ni-based anodes. Since there is a significant difference between the Ni and NiO volumes, this oxidization creates internal stress, tension in the electrolyte, crack formation, and eventually the system failure. The gas permeation through these cracks also speeds up the other degradation mechanism [93,99]. GDC reduction is another major cause of chemical stress as the GDC experiences a volume expansion and eventual cracking, along with the TEC mismatching between the other components [91,100,101].

3.3. Anode

Anode degradation mechanisms can be divided into three main categories:

- *Microstructural changes*
- *Coking and Poisoning*
- *Delamination*

The most common microstructural changes in Ni-based anodes are Ni coarsening, Ni migration, and Ni depletion, which are somehow connected to each other [102]. Ni coarsening is known as the most detrimental degradation mechanism in SOFC anode electrodes. The primary reason is surface diffusion along with the interface and is generally related to a kind of “Ostwald ripening” mechanism [103]. This coarsening arises from the tendency to lower the chemical potential by smoothing the particle surface and reducing the curvatures since the higher curvatures result in higher chemical potential [99,104]. Ni particle growth reduces both TBP sites (Fig. 8) and electrical conductivity, which weakens both performance and stability of the SOFC. Besides, the catalytic activity of the Ni decreases due to the loss of specific surface area in larger particles. Moreover, this mechanism deteriorates the Ni-YSZ contact and eventually causes the delamination of Ni from YSZ [105–107]. Ni coarsening can also result in Ni migration to the anode surface by evaporation/condensation process and diffusion. In the SOFC operating conditions, high temperature and water pressure, Ni, O_2, and H_2O react together and form $Ni(OH)_2$, taking place near the TPB region. Since $Ni(OH)_2$ has a lower melting point than the operation temperature, it would be evaporated, transferred to the surface, and then condensates to Ni atomic form. This Ni migration to the surface brings inconsistency in the Ni content of the anode and causes Ni depletion around the electrolyte/anode interface. This redistribution may affect the TPB length, particle size distribution, porosity, tortuosity and eventually causes the SOFC degradation. Further, Ni coarsening is responsible for Ni depletion, as the larger particles adsorb the smaller ones [67,102,108].

As previously mentioned, fuel flexibility is one of the advantages of SOFCs as they can internally reform the hydrocarbon fuels at elevated operating temperatures. However, there is the risk of anode coking as the produced Carbon Monoxide (CO) during the reforming process continues to react, referring to the Boudourd reaction [109–112]. This CO reacts with H_2 as well and results in more carbon formation. Several factors influence the coking rate, including steam/carbon ratio, anode composition, operation temperature, and current density. For instance, carbon deposition is inversely related to the steam/carbon ratio and applied current density. Anode coking covers the surface and blocks the TPBs and gas channels, and causes mechanical and electrochemical degradation. As the carbon deposition increases, so much pressure is created that can lead to the anode fraction [113]. Fig. 9 (a) and (b) show the SEM micrographs before and after carbon deposition on the surface of a Ni-based anode, respectively [110]. Kan et al. [114] showed that carbon formation occurs at the beginning of the cell operation. After the carbon deposition, amorphous carbon changes to graphitic carbon, damaging the single cell’s cohesive structure [114].

Apart from coking, hydrocarbon gaseous fuels are composed of different contaminants, including sulfur (S), phosphorous (P) [115,116], arsenic (As) [117], selenium (Se) [118], chlorine (Cl) [119], and antimony (Sb), may interfere with the anode and degrade the performance and stability of the SOFC [120]. The type and amount of these elements in the hydrocarbon fuel depend on the coal’s mine location and their process technique. The S poisoning from the hydrocarbon fuels in the anode is arisen from the interaction of H_2S anode, creating H_2 and elemental S. Ni particles have a strong tendency to adsorb this elemental S, which causes Nickel Sulfide (Ni_xS_y) deposition and blockage of active sites along with the redistribution of Ni at the interface [121]. Fig. 10 (a) illustrates S poisoning’s effect on Ni-based anode, taking place at two main steps [122]. Temperature, polarization, cell configuration among the H_2S concentration impact the degree of S poisoning [123]. P traces in coal lead to Nickel Phosphide’s development at the anode/electrolyte interface and brings irreversible performance loss to SOFC as these species hinder the active sites [124]. In addition to performance failure, the formation of NiP causes stress, resulted in the originating of microcracks in the Ni-free YSZ matrix and mechanical degradation in the anode, as in Fig. 10 (b) [115].

As is one of the especially concerned anode contaminants, as it is commonly spread in coals, easily reacts with H_2 to form arsine (AsH_3), and even small traces (10 ppb or less) are detrimental for SOFCs. Furthermore, this element is a notable poison for Ni catalysts due to its strong tendency to react with Ni. The formation of Ni_5As_2 and $Ni_{11}As_8$, determined by temperature, As concentration, flow rate, and exposure time, causes Ni coarsening and Ni migration to the anode surface. These processes induce the loss of electrical connectivity in the anode support and, finally, result in sudden failure. Before the failure, there is almost no sign of electrochemical degradation of the cell [126,127]. Se, another toxic impurity with higher volatility, is distributed in different coals in different concentrations. Se poisoning, which is quite like S poisoning,

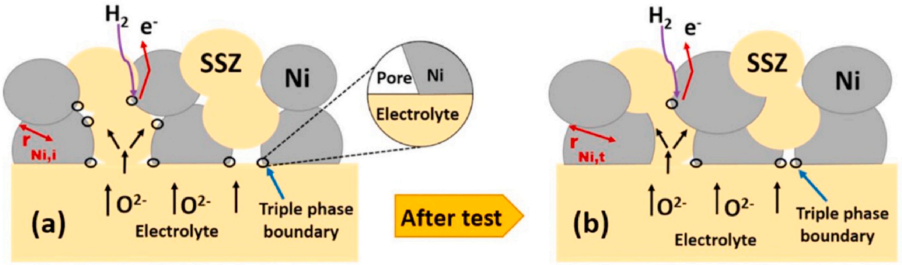

Fig. 8. Change in the TPB site caused by Ni coarsening. Reprinted from Khan et al., [103] with permission. Copyright 2018. Elsevier.

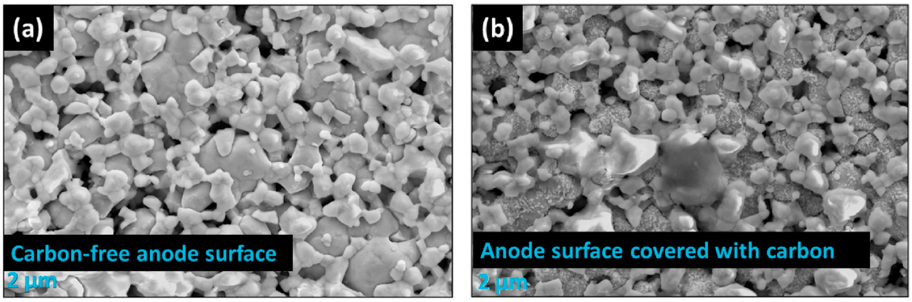

Fig. 9. SEM images of Ni-based anode surface (a) before and (b) after carbon deposition. Reprinted from Subotic et al., [110] with permission. Copyright 2016. Elsevier.

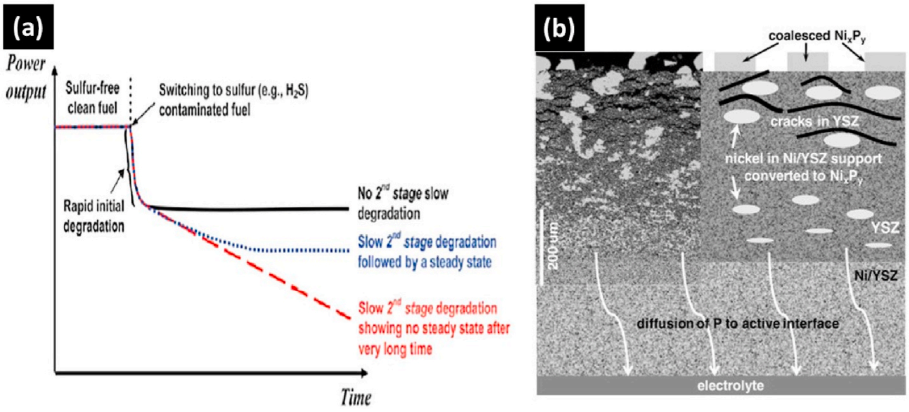

Fig. 10. (a) S poisoning effect on Ni-based anode upon exposure to H_2S, Reprinted from Cheng et al., [125] with permission. Copyright 2011. Royal Society of Chemistry; RSC Publishing. (b) Schematic diagram of the reaction of the Ni/YSZ anode with phosphorus in coal gas. Nickel phosphide phases form in outer portions of the anode support as illustrated by an SEM image of the anode-supported cell after 470 h operation on coal gas with 5 ppm PH_3 at 800 °C in the upper left corner. Surface diffusion of phosphorus to the active interface occurs as well, responsible for initial performance losses. Reprinted from Marina et al., [115] with permission. Copyright 2010. Elsevier.

originates from Se by Ni's surface adsorption and formation of Ni_3Se_2 at the anode/electrolyte interface. This solid phase inhibits the accessibility to active sites and causes SOFC degradation [118,126]. Cl poisoning is also a severe case since the SOFC practical fuels, like biofuels, contain Cl compounds in high concentrations. The presence of Cl, an electronegative species, can prevent the H_2 adsorption on the Ni surface, blocking the TBP region and limiting the electrochemical performance of SOFC [128]. This adsorption-desorption mechanism is found out to be a reversible process. Haga et al. [129] studied the microstructural change of Ni–Sc stabilized Zr anode by Cl poisoning. There was a considerable change in the microstructure after conducting the poisoning test by wet H_2 - 5 ppm Cl_2. Ni reaction with Cl_2 caused the $NiCl_2$ sublimation, which led to the continuous Ni depletion in the anode. The degradation rate of this test was 3%/1000 h, showing the importance of Cl poisoning [129].

Sb is another coal impurity with a wide application as a passivating agent for Ni catalysts in refineries. Cell degradation from Sb poisoning results from two processes, depending on the exposure length, Sb concentration, and applied current density. Ni surface adsorbs Sb, and the electrocatalytic activity of anode diminishes at the initial step, same as S and Se poisoning. This adsorption mechanism is reversible, and early reaction products only exist on the adsorption layer's surface. With a longer exposure duration, the late stage of the degradation, the severe one, begins with the broad formation of solid reaction products, especially NiSb. These products obstruct the electrical conduction pathways between particles (Percolation Loss), which irreversibly induces ohmic resistance. Furthermore, Sb poisoning leads to Ni coarsening, consumption, and migration to the surface, which are also unfavorable for anode performance [120,130].

Anode delamination is mainly due to oxidation cycling and thermal cycling. The first case causes volume changes in the anode, and the second one is because of the mismatch in TEC of the anode and the electrolyte [131]. Delamination is less common in anode than cathode due to the similar TEC of anode and electrolyte, but it still exists [81]. It should be noted that the Ni coarsening induces delamination because when the Ni particles grow bigger, the contact area with the electrolyte becomes smaller. Furthermore, delamination causes TPB reduction, which is one of the leading causes of degradation in SOFC [132].

3.4. *Interconnects*

The three degradation modes of interconnects are as follows:

- *Corrosion*
- *Cr vaporization*
- *Mechanical failures*

Interconnects are a fundamental element in SOFC stacks as they provide electrically conductive pathways among the single cells and aid in separating one cell's anode side fuel from the cathode side air of the next cell in the stack [82]. High-temperature SOFCs use ceramic interconnects developed from the semiconductor oxides. The most common of them are $LaCrO_3$-based interconnects, which are p-type semiconductor oxides. However, their application is restricted due to their challenging fabrication method, high price, and inadequate flexural strength [7]. Current SOFCs with lower operating temperatures (500–800 °C) use metallic interconnects instead of former ceramic ones owing to their lower cost, better electrical conductivity, and more straightforward fabrication processes [133]. Metal alloys such as Fe–Cr alloys, Cr alloys, Ni(Fe)–Cr-based heat resistant alloys, and austenitic and ferritic stainless steels (SS) are widely utilized as metallic interconnects. However, most metals are affected by oxygen, which causes corrosion. The corrosion not only weakens the mechanical stability of the interconnect but also reduces its electrical conductivity due to the emergence of insulating oxide phases like Cr_2O_3 and $(Mn,Cr)_3O_4$ [7,134,135]. Moreover, the simultaneous exposure of SOFC to fuel at one side and air at the other side in ferritic SSs is another cause of the corrosion, called the "dual atmosphere effect" [136]. This degradation is due to the different scale growth caused by the hydrogen transfer through the steel, accelerating the iron transfer and increasing its activity in growing iron oxides phases [137]. "Metal dusting" phenomenon, a serious kind of corrosion in metals and alloys in the carbon-supersaturated gaseous atmosphere at high temperatures, is another hazard to the metallic interconnectors while using carbon-containing fuel gases [138]. Metal dusting results in forming fine metal carbide or pure metal and carbon dust, causing a brittle structure and reducing the interconnector's mechanical strength [82,139].

Cr vaporization from interconnects causes Cr poisoning to the cathodes, one of the most severe degradation mechanisms in SOFCs responsible for a significant decrement in electrical conductivity by blocking the electrode's active TBP sites [7,140]. Furthermore, this Cr vaporization induces the Cr depletion in the interconnect, and this depletion below a specific threshold threatens its mechanical strength and structural integrity through the oxidation break-away [135,141]. Compared to other metallic interconnects, superalloys such as Ni–Cr- or Ni–Fe–Cr-base alloys provide a lower scale growth rate, leading to higher oxidation resistance behavior. Nevertheless, Ni-base alloys with enough Cr to obtain a high oxidation resistance show a high TEC, bringing the TEC mismatch between the other SOFC components and results in mechanical failure [7,142].

The Cr vaporization issue can be addressed by modifying whether the alloy composition [143,144] or surface conditions [141]. Stanislowski et al. [145] showed that the surface modification is more favorable due to Cr release results from different common Ni-, Cr-, and Fe-based alloys. These results presented that the Cr-dominant oxide generators need to be protected by protective coatings to become free of Cr evaporation [141]. Generally, 3 types of coating materials are available for SOFC interconnects, including reactive element oxides (e.g., La_2O_3, Nd_2O_3, Y_2O_3) [133,146], rare earth perovskites (e.g., LSM [147], $La_{0.75}Sr_{0.25}Cr_{0.5}Mn_{0.5}O_{3-\delta}$ (LSCM) [148]), and composite spinel oxides (e.g., Mn–Co-based [149–153], $NiFe_2O_4$ [154–156], Cu-based [157, 158]). So far, composite spinel oxides found out to be the most potential coating to save the interconnect from the Cr vaporization, enhance the electrical conductivity, and lower the TEC at the same time [149,153, 159,160].

3.5. Sealant

In general, sealants face the following modes of degradation:

- *mechanical failure and leakage*
- *corrosion*
- *poisoning*

Bonding or rigid sealants, e.g., glass ceramics, are sensitive to thermo-mechanical stress during the thermal cycles. This susceptibility causes non-linear behavior in thermal properties, including TEC, viscosity, and porosity, and changes over time, leading to TEC mismatch between the sealant and other stack components, mechanical failure, and eventually leakage [161–163]. Typically, leakage indicates that the anode receives less fuel than planned, which increases the stack's fuel consumption, causing fuel shortage, operating limitations, performance loss, and anode oxidation [164]. Hence, quantifying any changes in the stack leakages throughout the operation is valuable to identify them from other causes of stack voltage degradation, like increase in contact resistance, S poisoning, or measurement faults [165]. To lower the risk of mechanical failure and leakage rate, using non-crystallizing sealants, such as SiO_2–Al_2O_3–CaO–Na_2O–ZrO_2–Y_2O_3 systems, can be helpful since they are resistive to the considerable change in the TEC of material [161,166]. Another solution can be hybrid sealants to develop a seal that takes mechanical characteristics from the compressible core but, unlike typical compressive seals, has meager interfacial leak rates due to the compliant surface coating [167,168]. Fig. 11(a–d) illustrates the difference between a simple compressive seal and different types of hybrid seals. Fig. 11 (a) represents a regular mica-based compressive seal, which the most common cause of the leakage is the contact between the mica and the metal or ceramic. Using a compliant layer from binding sealants at the surface of the mica layer (shown in Fig. 11 (b)) can enhance the gas-tightness behavior by making a hybrid seal. Moreover, Fig. 11 (c) depicts another technique for creating a hybrid seal with mica and metal sealants by setting the mica powder in the interspace of a corrugated metal sealant. Also, it is possible to develop the sealant performance through the infiltration of the mica with a bonding sealant phase to enhance mica particle-to-mica-particle adhesion, as outlined in Fig. 11 (d) [164]. In this regard, Rautanen et al. [162] developed a hybrid sealant, glass powder-coated Thermiculite 866, with leakage rates of 0.1–0.3 mL m min $^{-1}$, 60–90% less than the uncoated sealant. This decreased leak rate was due to the conformability of the glass coating that covered the Thermiculite 866 surface defects and blockage of interfacial leak paths by the adjacent elements [162].

Although glass-based sealants show a better leakage resistivity, their impurities, like Si, can be poisonous to cathode and anode and hinder their surface reactions, causing performance degradation in the SOFC stack. In Si poisoning, Si deposits on the TPBs and cathode surface, inhibiting the oxygen reduction reaction [139]. Moreover, deposited Si can react with the cathode surface and change the surface composition by forming insulating phases. In fact, this form of poisoning is most commonly seen in Sr-containing perovskites at high temperatures, forming stable silicates (e.g., Sr_2SiO_4) and blocking the active surface sites [139,169]. In addition to impurities, their constructive cations, such as Ba^{2+} and Zr^{4+}, can become deleterious for the long-term performance of the SOFC. Ba^{2+} has a strong tendency to react with Cr from the ferritic interconnects and create unwanted and insulating $BaCrO_4$ [170]. On the other hand, Zr^{4+} leans to form bulk crystallization in the glass or glass-ceramic sealants, causing the growth of microcracks and weak mechanical stability in long-term performance [171]. Also, the presence of alkali cations (Li^+, Na^+, K^+) in the glass- and glass-ceramic-based sealants makes them more likely to react with other cell components. They can induce cathode Cr poisoning by speeding the Cr vaporization of interconnects [139,172,173].

There are several techniques to control the sealants corrosion, such as lowering the Si content, making Ba^{2+}-, alkaline- and alkaline earth metals-free sealants, and controlling the Zr^{4+} amount [82,170,171]. In this regard, Kiebach et al. [170] from DTU developed a CaO and ZnO-rich glass composed of 50 mol% CaO, 20 mol% ZnO, 20 mol% B_2O3, and 10 mol% SiO_2, named CZBS. This CZBS glass showed no degradation or sealant-related leakage for over 400 h under dual-phase atmospheres (Air/H_2) at 750 °C (for first 100 h) and 850 °C for the rest of the operation.

4. Characterization techniques

The advancement of SOFCs to fulfill the durability targets needs a developed understanding of material properties and their interactions. Using different characterization methods to study the SOFC materials and how they behave before and after operations helps in advancing this field. Furthermore, this requirement leads to the development of various types of state-of-the-art characterization equipment, which are adaptable to the extreme operating conditions of SOFCs. These advanced methods, known as *in-situ* techniques, help us study the materials while operating as a SOFC. *In-situ* TEM, *in-situ* Raman spectroscopy, and infrared imaging are in this category [174]. In addition to characterization techniques, numerical modeling is a leading approach to study and investigate the SOFC behavior for optimizing, controlling, and enhancing energy efficiency and durability performance [175,176]. This section will cover the different structural and electrochemical characterization techniques along with the numerical modeling for studying and developing SOFC durability and stability performance. A summary

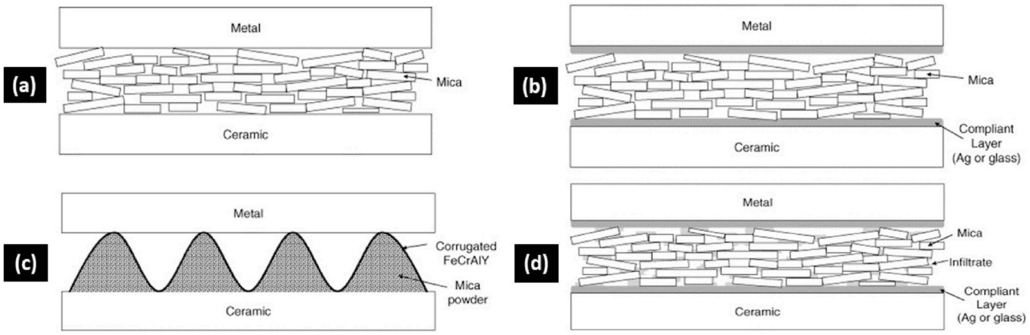

Fig. 11. (a) a simple compressive mica sealant, (b) hybrid sealant with ceramic/metal compliant layer and mica. (c) hybrid sealant with corrugated metal and mica powder. (d) hybrid seal with infiltrated mica and ceramic/metal compliant layer. Reprinted from Jeffrey W. Fergus, [164] with permission. Copyright 2005. Elsevier.

of these characterization techniques is given in Table 1.

4.1. Electrochemical characterization

Electrochemical characterization is an essential tool for the degradation evaluation of SOFC. The most common techniques for this purpose are current-voltage (I–V) measurements, electrochemical impedance spectroscopy (EIS), and long-term galvanostatic or potentiostatic stability tests. These measurements are carried out in a fuel cell reactor with the desired operating temperature, fuel, and oxidant [177]. The degradation study in the I–V and C–V measurements and EIS is usually based on the comparison of the SOFC performance before and after the durability test under the current conditions and atmospheres [178]. Furthermore, these techniques demonstrate the effectiveness of a method to prevent degradation by comparing the SOFC performance before and after applying that specific method, such as coating and doping.

4.1.1. Current-voltage measurement

The current-voltage (I–V) measurement technique evaluates the SOFC performance by applying a direct current (DC) sweep through the SOFC from 0 to a given current density, and a potentiostat/galvanostat device measures the resulting DC potential. In the I–V curve, the irreversible losses, including reaction rate, resistance, and gas transport, decrease the voltage output from its theoretical value [176]. The degradation rate is calculated by comparing the initial results and the results obtained after the operation of the SOFC. For instance, Wang et al. [179] used the I–V measurements to study the effect of porous and dense $CuMn_2O_4$ coating for the interconnect on the Cr poisoning. Fig. 12 presents the I–V curves and the corresponding power density of three different anode-supported cells of LSM|LSM-8YSZ|Ni-8YSZ at 0 h and 48 h after cell performance at 800 °C in dry air. The results indicated that the cell with the dense spinel coating had the highest power density and lower voltage loss, owing to Cr-poisoning prevention.

4.1.2. Electrochemical impedance spectroscopy

In the electrochemical impedance spectroscopy (EIS) measurements, the cell is subjected to a low magnitude alternating signal, calculating the impedance as a function of the alternating current (AC) source. In general, a Nyquist plot demonstrates the Impedance spectra by showing the imaginary part on the Y-axis and the real part on the X-axis at different frequencies. The intercept on the real axis at higher frequencies (>1 kHz) represents the cell's ohmic resistance, including interconnect and wires. At the lower frequencies (<1 kHz), this interception corresponds to the total cell resistance, which is the sum of the ohmic and electrode polarization resistances. This relationship is applicable in studying the dynamic electrode process, ORR activity, double layer capacitance, grain diffusion, and other similar phenomenons [180–182]. The electrode polarization resistance, which includes the charge- and mass-transfers, can reflect the degradation behavior of the SOFC by comparing the polarization resistance values before and after the cell performance under different operation terms. The EIS measurements can be performed both in Open Circuit Voltage (OCV) and under load conditions [183].

Li et al. [182] studied the effect of a dense $La_2NiO_{4+\delta}$ (LN) coating on the Cr tolerance of the $PrBa_{0.5}Sr_{0.5}Co_{1.5}Fe_{0.5}O_{5+\delta}$ (PBSCF) double perovskite by EIS. Fig. 13 (a) and (b) exhibit the Nyquist plots of pure and coated cathodes at 400 mA cm^{-2} at 750 °C for 1200 min, respectively. There is a significant reduction of low-frequency resistance (R_L) after applying the LN coating, indicating that LN coating will effectively facilitate the cathode's oxygen surface function due to its superior oxygen surface exchange property. Fig. 13 (c) and (d) represent the rise of the Polarization resistance (R_P) and Ohmic resistance (R_Ω) as a function of aging time at 750 °C under a cathodic polarized current of 400 mA cm^{-2} for 1200 min. There is a parabolic mode in the R_P increment of PBSCF cathode, demonstrating that the Cr deposition takes place at the beginning of the polarization. Moreover, R_P's ascending trend for the coated cathode is much slower than the pure one, showing the cathode's enhanced Cr toleration [182].

Wei et al. [184] examined the role of reduced $La_{0.6}Sr_{0.2}Cr_{0.85}Ni_{0.15}O_3$ containing exsolved Ni nanoparticles with GDC (LSCrN@Ni-GDC) (Fig. 14 (a)) in the prevention of carbon formation by EIS measurement. The EIS was performed on Ni–GDC anode-supported cells with and without the LSCrN@Ni-GDC catalyst layer at 750 °C using 50% CO_2–50%CH_4 as fuel. The Nyquist plot (Fig. 14 (b)) demonstrates a smaller anode polarization resistance for the LSCrN@Ni-GDC cell, owing to the LSCrN@Ni-GDC CH_4 pre-reforming characteristic, which prevented carbon formation and saved the gas pathways from blockage [185].

In another work, EIS was used to investigate the degradation phenomena of the $Sm_{0.5}Sr_{0.5}CoO_{3-\delta}$ (SSC) fibrous cathode with encapsulated $Sm_{0.2}Ce_{0.8}O_{1.9}$ (SDC) particles (SSC-SDC). To do this, researchers compared the EIS data of SSC-SDC half-cell before and after applying a cathodic polarization (500 mA cm^{-2}, 700 °C, 120 h). The results revealed that charge transport (R_1) and surface catalytic reaction (R_2) resistances increased from 0.034 Ω to 0.076 Ω–0.090 Ω and 0.134 Ω, respectively. This degradation was due to the Sr enrichment and Co deficiency on the surface, which insulated the fibers. Moreover, particle coarsening and grain growth reduced the TPB areas and caused unfavorable performance [186].

4.1.3. Calendar life test

The calendar life test performs the durability test under constant operating conditions, such as voltage or current density [189]. For instance, Xu et al. [74] performed a durability test for an anode-supported flat-tube cell with 30 cm^2 of cathode effective are for almost 400 h under a 16 A cell current at 750 °C to test the CO_2-tolerance of a Ga-doped perovskite cathode $Sr_2Fe_{1.3}Ga_{0.2}Mo_{0.5}O_{6-\delta}$ (SFGM). First, the anode-supported single cell of SFGM cathode was operated in pure air for 97 h. Then, a 5% CO_2-containing air purged in, and the operation

Table 1
A summary of characterization techniques in the evaluation of SOFC's durability and stability.

Characterization Tool	In-situ/ ex-situ	Result	Adv.	Disadv.
Electrochemical				
I–V measurements	In-situ	Power density	Conclusive performance metric	Intrinsically nonspecific, Lack of information in the degradation process
EIS	In-situ	Resistance of cell components	Transport properties and role of each component in ohmic losses	Lack of information in the degradation process
Calendar life test	In-situ	Current/ Voltage changes during the time	Degradation rate	Lack of information in the degradation process
Chemical (Spectroscopy techniques)				
Raman Spectroscopy	Both	Electrical conductivity, doping, phase, and compositional information of materials and adsorbates	Degradation processes such as phase separation, coking, and S poisoning	Limited sampling area [174]
XRD	Both	Changes in the crystal structure	Phase changes, poisoning, and formation of secondary phases	Limited sampling area
FT-IR	Ex-situ	Surface chemistry of components	Adsorbed species and surface reactions [187]	Experimentally challenging
XPS	Both	Material chemistry and structure	Impurity analysis	Providing elemental information instead of molecular
SIMS	Ex-situ	Detailed surface chemistry	Sensitive impurity analysis (1–1000 ppm) [188]	Locally destructive, Lack of quantitative results
Structural (Macroscopy techniques)				
TGA/DSC	Ex-situ	Thermal decomposition of component	Structural stability	Lack of information in the degradation process
Dilatometry	Ex-situ	Thermal expansion	Structural stability	Lack of information in the degradation process
Tensile test	Ex-situ	Tensile strength	Structural stability	Lack of information in the degradation process
Bending test	Ex-situ	Flexural strength	Structural stability	Lack of information in the degradation process
Structural (Microscopy techniques)				
SEM and EDS	Ex-situ	Morphological and elemental details	Formation of secondary phases, poisoning	Unable to detect impurities in ppm
TEM	Ex-situ	Diffraction patterns and crystal structure	Structural changes	Challenges in sample preparation
AFM	Ex-situ	Surface roughness	Poisoning and formation of secondary phases	Single scan image size

continued for 291 h. There was a small reduction in the cell voltage after switching to CO_2-containing air as CO_2 filled the ORR actives sites and decreased the discharge performance (Fig. 15 (a)). Even after this voltage reduction, SFGM performance was stable during the next 291 h. This excellent CO_2 resistivity was due to the weaker affinity of SFGM towards the chemical adsorption of CO_2. Fig. 15 (b) compares the competitive adsorption of CO_2 and O_2 on the surface of SFGM [74].

In another study, researchers demonstrated the superior contaminant tolerance of a novel hybrid catalyst of $PrNi_{0.5}Mn_{0.5}O_3$ (PNM) with exsoluted PrO_x nanoparticles for the LSCF cathode (Fig. 16 (a)) by conducting a long term-stability test. Fig. 16 (b) compares the durability performance of three different single cells of bare LSCF, 0.1 M, and 0.3 M hybrid-LSCF under 7 V at 750 °C for 600 h wet H_2 and direct Crofer contact. The results represented an exceptional durability behavior in the 0.3 M hybrid catalyst coating (0.04%/h as degradation rate) along with the enhanced power density. The improved durability performance against Cr poisoning and moisture was due to the presence of the dense conformal PNM coating, while the PrO_x nanoparticles accelerated ORR kinetics and boosted the power density [79].

4.2. *Chemical and structural characterizations*

Chemical and structural characterizations are valuable methods for understanding the origin of the degradation behavior of SOFC. There are multiple analytical techniques useful to characterize the "postmortem" status of different SOFC elements when the cell has been cooled down to room temperature and disassembled, called *ex-situ* characterization [190]. On the other hand, *in-situ* characterization methods study the samples during the electrochemical operation at elevated temperatures with the desired atmosphere. These *in-situ* techniques connect the phase transitions, composition changes, and other physical transformations to the performance degradation of SOFC, evaluated by voltammetry and EIS [190,191]. This section will cover the role of these spectroscopic techniques, such as Raman spectroscopy, X-ray diffraction (XRD), Fourier transform infrared spectroscopy (FTIR), and mass spectrometry (MS), in studying the degradation of SOFCs' performance.

4.2.1. *Chemical characterization (Spectroscopy techniques)*

4.2.1.1. Raman spectroscopy. Raman spectroscopy is a unique tool for studying SOFC degradation behavior. It is not an electron-based technique and so does not need a vacuum environment, allowing the *in-situ* studies of samples under the harsh operating conditions of SOFC. There are several studies on using *in-situ* Raman spectroscopy for detecting coking [192–197]. Kirtley et al. [196] used the *in-situ* Raman spectroscopy to evaluate the carbon formation rate on Ni/YSZ anodes, which there were exposed to dry CH_4 for 10 min under OCV at 730 °C. The Raman Spectra of Ni cermets in Fig. 17 (a) shows no peak from 1200 to 1700 cm^{-1} before the exposure. After a few seconds of CH_4 initiation, a vibrational band at 1556 cm^{-1} occurs in the Raman spectrum, attributed to the "G" peak of highly ordered graphite. This graphite signal proceeds to increase during the next ~7–8 min before hitting an asymptotic limit (Fig. 17 (b)). Other phenomena, including the formation of the surface

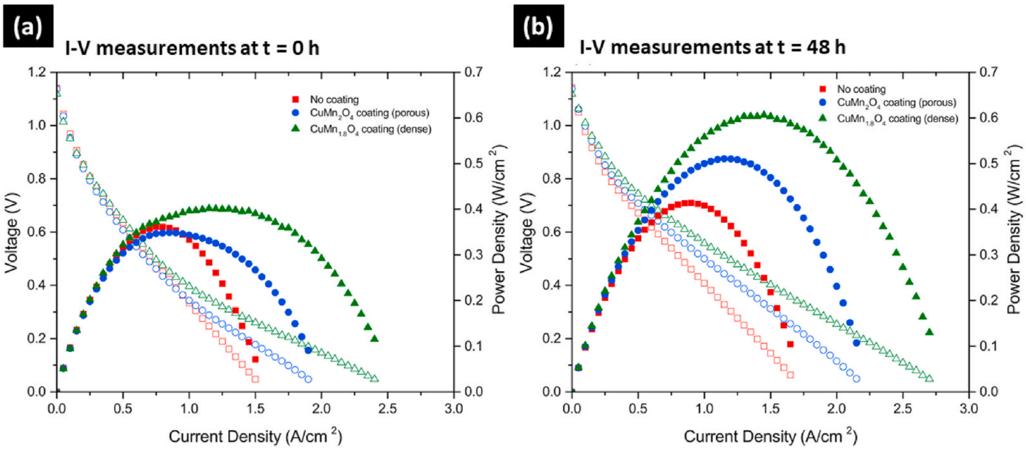

Fig. 12. I–V curves and the corresponding power density of LSM|LSM-8YSZ|Ni-8YSZ anode-supported cells (a) before and (b) after 48 h cell performance at 800 °C in dry air to study the effect of CuMn$_2$O$_4$ spinel coating on the Cr poisoning. Reprinted from Wang et al., [179] with permission. Copyright 2018. Elsevier.

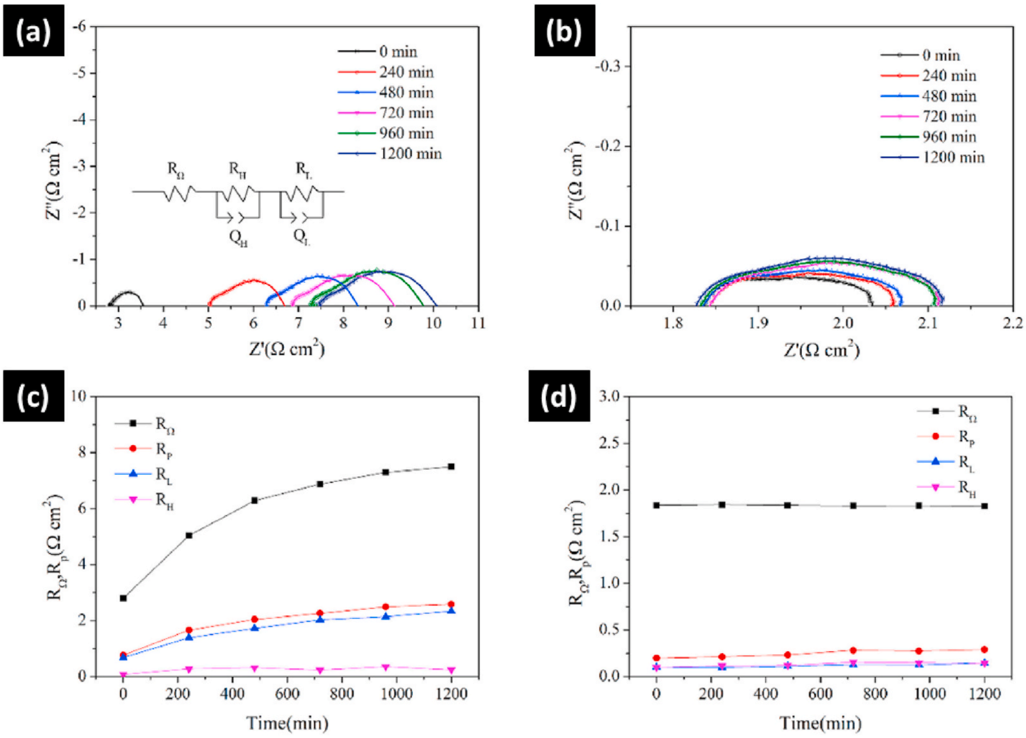

Fig. 13. EIS results of cathodes with a current density of 400 mA cm^{-2} at 750 °C for 1200 min in the presence of SUS430 interconnect for Cr-poisoning evaluation: (a, c) PBSCF and (b, d) LN-coated PBSCF. Reprinted from Li et al., [182] with permission. Copyright 2018. Elsevier.

layer in electrolytes [198,199], S [200–202], and Cr poisoning [79,203], are discoverable using *in-situ* Raman spectroscopy. Fig. 17 (c) illustrates a schematic of the *in-situ* Raman spectroscopy arrangements [125].

Ex-situ Raman spectroscopy is a practical technique to study the phase stability, oxidation degrees, degradation of different SOFC elements, species migration through the SOFC structure, and poisoning [174,203], mostly for coking and S poisoning [205–207]. Niu et al. [204] used the *ex-situ* Raman spectroscopy to investigate the coking and S poisoning resistance of double perovskite $Sr_2TiFe_{0.5}Mo_{0.5}O_{6-\delta}$ (SFTM05) anode. As it is obvious in the anode's Raman spectra (Fig. 17 (d)), there are no signs of S poisoning due to the absence of 460, 622, 1001 cm^{-1} peaks for $SrSO_4$, 335, and 380 cm^{-1} peaks for TiS_2, 340, and 370 cm^{-1} peaks for FeS_2, and 380 and 410 cm^{-1} peaks for MoS_2. Moreover, the Raman spectrum indicates no carbon deposition as carbon's three primary peaks are not detected in the spectrum [204].

4.2.1.2. Fourier-transform infrared spectroscopy. Fourier-transform infrared (FT-IR) spectroscopy is another spectroscopic method to study the SOFC degradation by providing direct analysis of adsorbate molecules and adsorbent solid surfaces, which leads to a complete estimation of surface structure changes in SOFC components, like S [208], Cl [209], CO_2 [210,211], and humidity [212] poisonings [208]. For instance, Zhu et al. [213] studied the CO_2 resistivity of $SrNb_{0.1}Co_{0.9-x}Fe_xO_{3-\delta}$ ($0 \leq x \leq 0.9$) (SNCF$_x$) with the FT-IR technique by exposing the powders to high purity CO_2 (99.999%) at 600 °C for 1 h. Fig. 18 (a) and (b) present the FT-IR spectra of SNCF$_x$ powders before and after CO_2 exposure, respectively. Comparing the intensity of 1440 cm^{-1} and 860 cm^{-1} peaks, which are the characteristic vibrational bands of carbonate groups, provides a CO_2-resistive behavior for SNC, SNCF0.5, and SNF.

4.2.1.3. X-ray diffraction. X-ray diffraction (XRD) is an effective

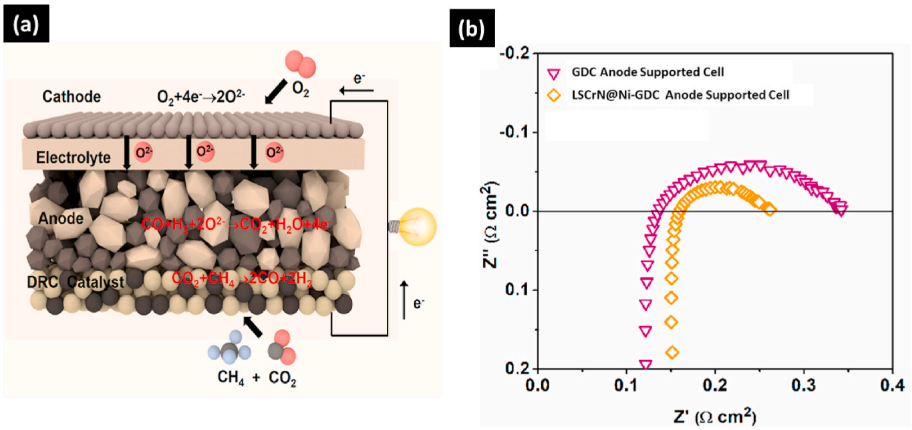

Fig. 14. (a) Schematic diagram of LSCrN@Ni-GDC in an anode-supported oxide-conducting SOFC, (b) EIS data of GDC anode-supported cell with and without LSCrN@Ni-GDC catalyst layer at 750 °C with 50%CO_2–50%CH_4 as fuel. Reprinted from Wei et al., [184] with permission. Copyright 2021. Elsevier.

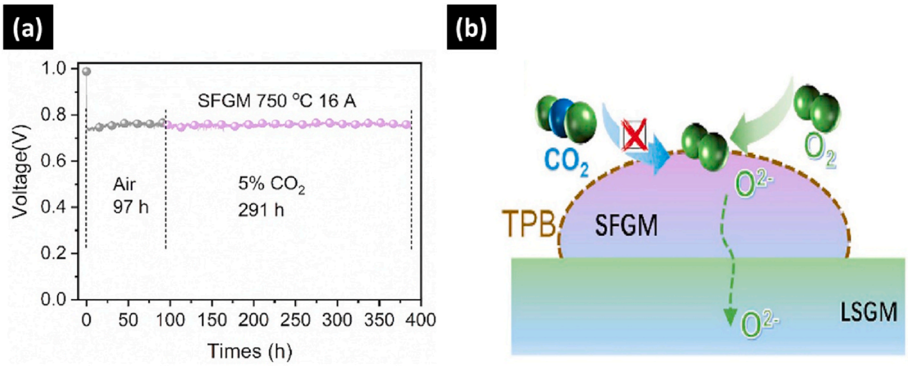

Fig. 15. (a) Durability test of an anode-supported single cell of SFGM cathode, (b) Schematic illustration of competitive chemical adsorption of CO_2 and O_2 on the surface of SFGM cathode. Reprinted from Xu et al., [74] with permission. Copyright 2020. Elsevier.

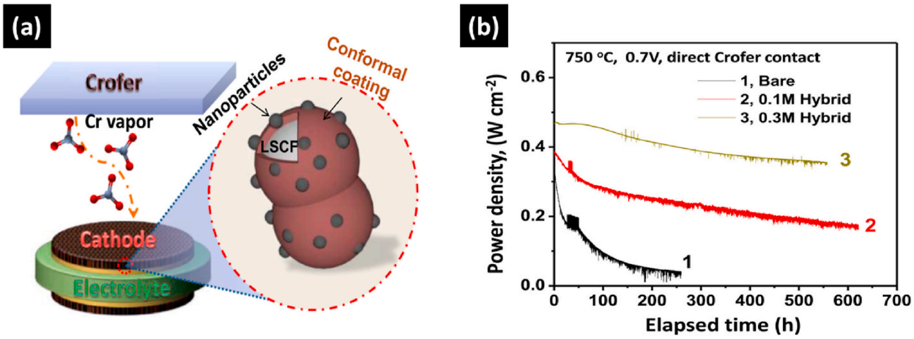

Fig. 16. (a) Schematic of the hybrid catalyst of PrNi0.5Mn0.5O3 (PNM) with exsoluted PrO_x nanoparticles for the LSCF cathode, (b) long-term durability test for three different single cells of bare LSCF, 0.1 M, and 0.3 M hybrid-LSCF under 7 V at 750 °C for 600 h with wet H_2 and direct Crofer contact. Reprinted from Chen et al., [79] with permission. Copyright 2018. Elsevier.

technique to examine the changes in the crystal structure of electrochemical cell materials, available in both *ex-situ* and *in-situ* modes [214]. XRD is practical for studying the chemical stability and compatibility of SOFC different components [204,215,216]. Furthermore, unit cell growth and changes in TEC [217], phase changes and impurities [215], poisoning [182,218], and formation of secondary phases such as Sr segregation [219] are observable via this mode. Niu et al. [204] used the *ex-situ* XRD to study the chemical compatibility of the $Sr_2TiFe_{0.5}Mo_{0.5}O_{6-\delta}$ (STFM05) anode with LSGM and SDC electrolytes. The SFTM05-LSGM and SFTM05-SDC were first calcinated at 1000 °C for 10 h in 5% H_2/Ar atmosphere. XRD patterns in Fig. 19 (a) revealed no noticeable peaks other than the SFTM05, LSGM, and SDC peaks. These peaks did not face any shifts, indicating no significant chemical reactions between the components and the chemical compatibility of the SFTM05 anode with LSGM and SDC electrolytes. This specification is essential to preserve the long and stable operation of the SOFC. In another study, [219] researchers investigated the effect of humidity on the process of Sr segregation in $Sr_9Ni_7O_{21}$ (SNO) cathode via *ex-situ* XRD technique over time. At first, the XRD test was carried out on the as-synthesized SNO powder. Then, the sample powder was placed in a humid environment for 1 week. The XRD patterns of the as-synthesized and moisturized samples are depicted in Fig. 19 (b,c). As it is obvious in

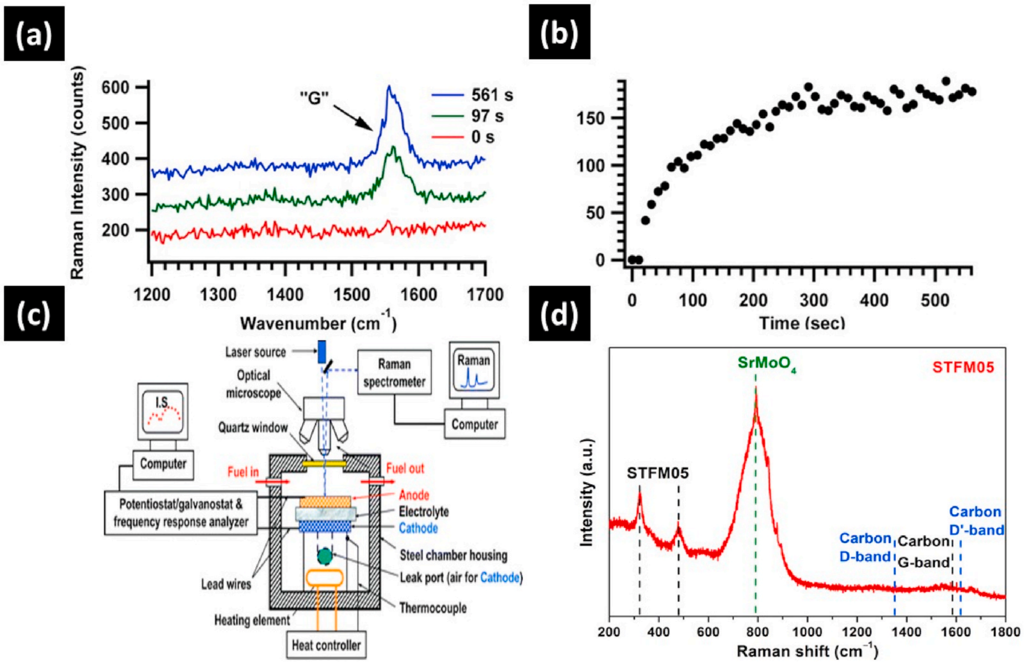

Fig. 17. In-situ Raman Studies of Carbon Removal from High-Temperature Ni–YSZ Cermet Anodes by Gas-Phase Reforming Agents 730 °C, (b) The intensity of "G" peak during the exposure, Reprinted from Kirtley et al., [196] with permission. Copyright 2013. American Chemical Society. (c) Schematic for the in-situ Raman microspectroscopy measurement system coupled with electrochemical measurement equipment, Reprinted from Cheng et al., [125] with permission. Copyright 2011. Royal Society of Chemistry. and (d) Raman spectroscopy of the STFM05 anode surface after stability performance. Reprinted from Niu et al., [204] with permission. Copyright 2018. Elsevier.

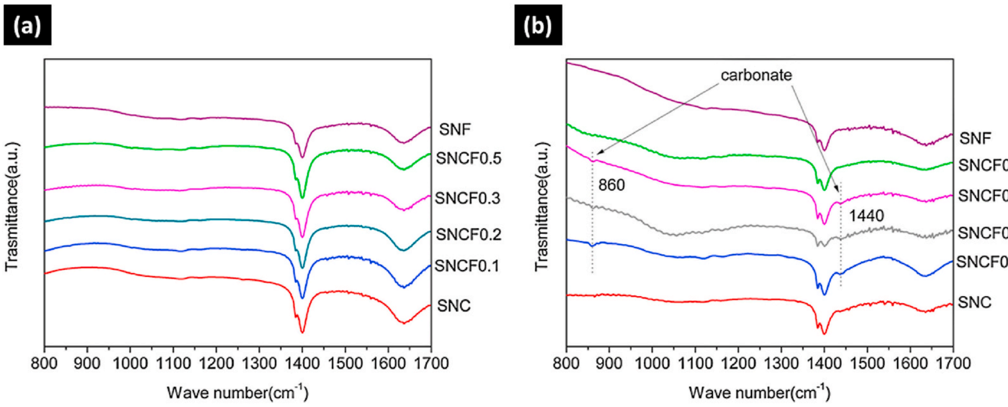

Fig. 18. FT-IR spectra of different SNCF powders (a) before and (b) after exposure to CO_2 at 600 for 1 h. Reprinted from Zhu et al., [213] with permission. Copyright 2015. Elsevier.

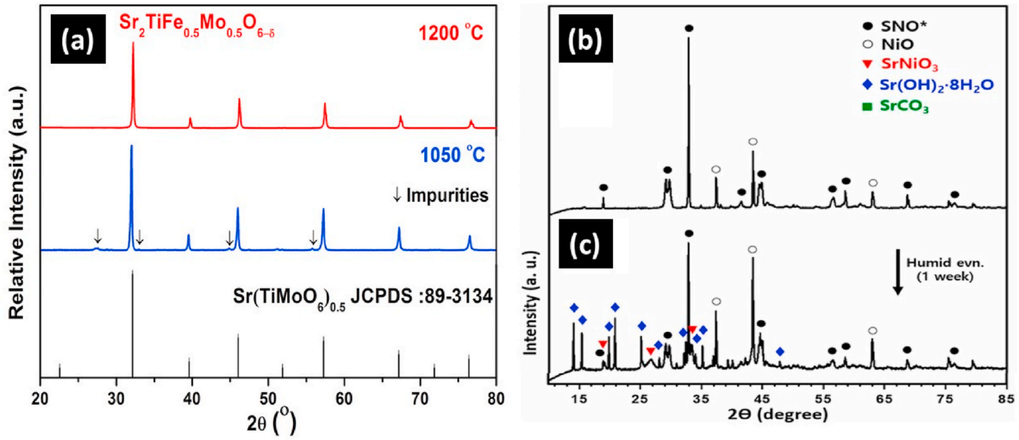

Fig. 19. (a) Room-temperature XRD patterns of the STFM05 sample after sintering at 1200 °C for 10 h in 5% H_2/Ar,. [204]. Reprinted from Niu et al., [204] Copyright 2018. Elsevier. XRD patterns of (b) as-synthesized SNO (Sr:Ni ratio of 35:65); (c) the SNO placed in the humid environment for 1 week [219]. Reprinted from Hong et al., [219]. Copyright 2019. Electrochemical Society.

Fig. 19 (c), two new peaks of $Sr(OH)_2.8H_2O$ and $SrNiO_3$ are emerged, implying the Sr segregation from SNO due to the presence of moisture and formation of $Sr(OH)_2.8H_2O$ [219].

In-situ XRD, also called high-temperature XRD measurements, is a valuable technique for observing the crystal structure transformations with temperature and studying the structure stability of the SOFC component in the working temperature [220]. For instance, Dong et al. [221] studied the structural stability of the $BaFe_{0.95}Sn_{0.05}O_{3-\delta}$ (BFS) cathode at higher temperatures. The *in-situ* XRD measurement results collected in the temperature range of 100–800 °C are shown in Fig. 20. There is a multiple-to-single phase transition, which occurs around 500 °C due to Fe ions' thermal reduction. Subsequently, this single phase shows proper stability for further heating up to 800 °C, demonstrating a thermodynamically stable state within the cell activity's temperature range [221].

4.2.1.4. X-ray photoelectron spectroscopy. X-ray photoelectron spectroscopy (XPS) is another important tool to examine the surface chemistry of the SOFC components, which is critical to governing the stability and can be performed in both *ex-situ* and *in-situ* modes. This characterization method is suitable for studying the Sr segregation [222–224], carbon deposition [225,226], the formation of secondary phases [227,228], and chemical stability [229,230]. Jang et al. [226] used the XPS *ex-situ* analysis to show the effect of Pd nanoparticles on the coke resistivity of Ni anode. The XPS analysis was conducted on a bare and a Pd-coated Ni anode after the methanol cell test. As shown in XPS spectra in Fig. 21 (a,b), the amount of carbon considerably decreased after applying 600 cycles of Pd nanoparticles coating by the atomic layer deposition (ALD) method [226].

In another study [231], the transformation of the surface structure of the $La_{0.6}Sr_{0.4}CoO_{3-\delta}$ electrodes was characterized by near-ambient pressure (NAP)-XPS at high temperatures while running impedance spectroscopy to measure the surface activity of the material at the same time. To collect the *in-situ* XPS spectra during the EIS measurements, 0.5 mbar O_2 was added into the NAP-XPS chamber, and the temperature was raised to 780 °C stepwise. The XPS results revealed the Sr segregation and formation of a secondary Sr-rich oxide phase at the surface at 450–500 °C due to the emergence of a third species in both Sr 3d and O 1s spectra (Fig. 22). This Sr oxide phase covered the electrochemically active sites of the Co surface, causing LSC degradation [231].

4.2.1.5. Secondary Ion Mass Spectrometry. The Secondary Ion Mass Spectrometry (SIMS) technique is able to detect the concentration distribution of contaminations, including poisoning (such as S and Cr) [73,232] and secondary phases [223,233,234], in a high-sensitivity depth direction for studying the poisoning resistivity properties of SOFC components. New Energy and Industrial Technology Development Organization of Japan (NEDO) is among the first groups to use SIMS to detect cathode S poisoning for their SOFC durability project [70]. Develos-Bagarinao et al. [235] research is an example of using *ex-situ* SIMS to clarify the physical origin of the cathode/interlayer of interfacial resistances of how GDC cathode/interlayer microstructure affects long-term durability. First, they carried out the SIMS elemental depth profiling on as-grown LSC thin film deposited on GDC-buffered (100)- and (111)-oriented YSZ, shown in Fig. 23 (a) and (b), respectively. Then, additional SIMS analysis was performed on the similar samples after annealing at 600 °C for ~ 160 h, represented in Fig. 23 (c) and (d) for LSC/GDC/YSZ(100) and LSC/GDC/YSZ(111), respectively. The profiles demonstrated a wide cation (Zr and Y) diffusion across the LSC/GDC interface on the YSZ(100) substrate after the annealing due to the nanocolumnar microstructure of the GDC interlayer. This cation interdiffusion caused the formation of the yttrium-doped $SrZrO_3$ (SZY) secondary phase with a blocking effect in the interface. In contrast, LSC/GDC/YSZ(111) before and after profiles are almost identical without any prominent Y or Zr peaks, indicating no SZY formation as the GDC layer is dense and prevents the interdiffusion [235].

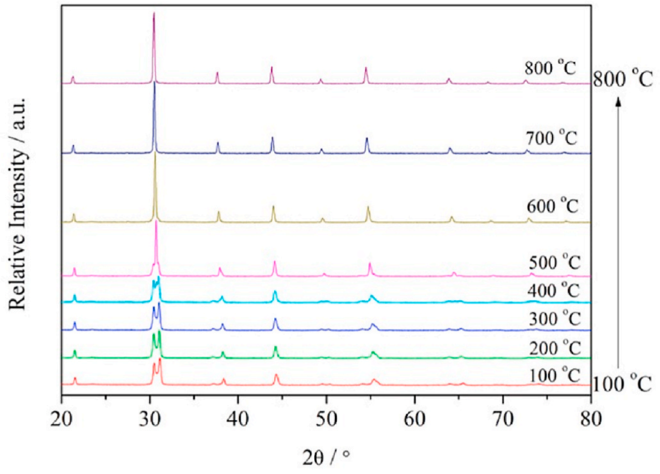

Fig. 20. In-situ XRD patterns of BFS over the temperature range between 100 and 800 °C in the air. Reprinted from Dong et al., [221]. Copyright 2016. Elsevier.

4.2.2. Structural characterization (Microscopy techniques)

Microstructural changes have a significant role in affecting the degradation process of SOFCs; hence, microscopy techniques are valuable for a detailed study of SOFC microstructure by providing both 2D and 3D images of the component structure [12,236]. Researchers use microscopic analyses, including AFM, SEM, and TEM, in pre- and post-test as well as *in-situ* modes to perform a comprehensive study on degradation mechanisms.

In general, electron microscopy studies, including scanning electron microscopy (SEM) and Transmission electron microscopy (TEM), are conducted by directing a high-energy focused electron beam on the sample surface, which generates different electron signals with different energies to providing a 2D image. Fig. 24 illustrates the interaction of the electron beam with the sample. Secondary electron (SE) and backscattered electron (BSE) signals are widely used in the SEM.

4.2.2.1. Scanning electron microscopy. Secondary electrons (SEs) present information about the surface characteristics as they are low-energy electrons (< 50 eV) and the scanning electron microscopy (SEM) detector can only find them if they are emitted close enough to the sample's surface. Different degradation mechanisms like Cr [237] and S poisoning [238], coking [239], Ni agglomeration [240,241], Sr segregation are detectable using SE - SEM. Fig. 25(a–g) shows the SE - SEM images of various SOFC components deteriorated by the mentioned mechanisms after long-term operation. Fig. 25 (a) and (b) demonstrate the fresh LSM cathode, and Cr poisoned LSM cathode after a potentiostatically operation at 0.7 V for 1217 h operation at 700 °C. The LSM cathode catalyst has a porous structure with fine particles. However, after the long-term operation, the particles become much denser due to Cr poisoning, visible as light grey angular crystals on the LSM surface [237]. In Fig. 25 (c) and (d), which are the SE - SEM images of $La_{0.75}Sr_{0.25}Cr_{0.5}Mn_{0.5}O_{3-\delta}$ (LSCrM) anode, S poisoning roughened the smooth surface of the electrode after ~ 5 h of H_2S poisoning process at 850 °C in H_2-50 ppm H_2S atmosphere [242]. In the case of coking, Lee et al. [239] exposed the Ni-coated GDC electrolyte to CH_4 for 3 h at 610 °C in order to investigate the susceptibility of Ni surfaces to carbon formations. As shown in Fig. 25 (e), carbon deposition appeared on the exposed Ni surfaces [239]. Moreover, Ni agglomeration, as one of the degradation mechanisms for SOFC anode, is observable in the SE−SEM cross-sections of the anode-electrolyte interfaces for a pristine and degraded cell in Fig. 25 (f) and (g), respectively. The degraded cell, operated by a constant power around 4.5 W at 700 °C with a fuel

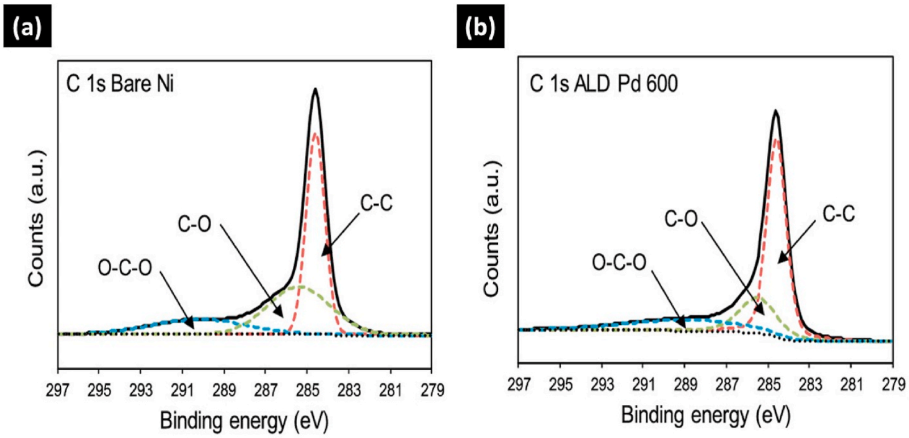

Fig. 21. (a) Chemical states of carbon on the surface after cell operation with methanol at 450 °C for the bare Ni anode, and (b) A-Pd 600 samples with the fitting of C–C, C–O, and O–C–O groups. Reprinted from Jang et al., [226] with permission. Copyright 2020. American Chemical Society.

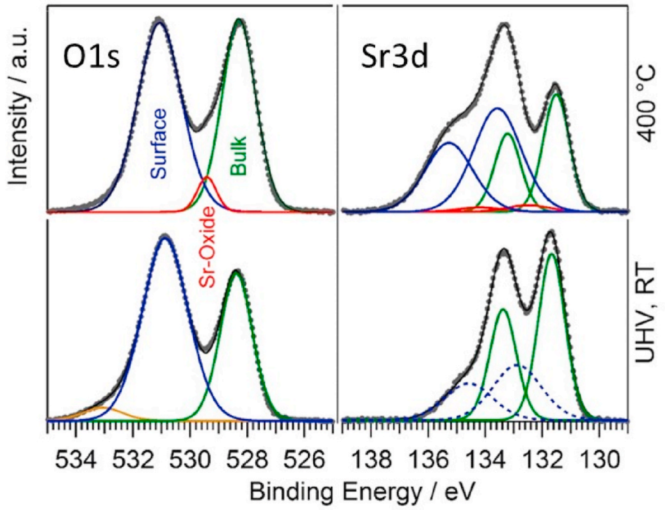

Fig. 22. XPS spectra of the virgin's surface state, water-treated sample directly after introduction into UHV system (a) at room temperature, and (b) the initial state at 400 °C in 0.5 mbar O_2. For both O 1s and Sr 3d, the green line corresponds to the perovskite bulk signal of LSC. The blue line represents the surface signal of the perovskite. The further red peaks of the degraded state result from a third Sr-oxide compound forming on the surface. Before heating, surface hydroxyls were observed—see component at ca. 533 eV in O 1s spectra before heating (yellow line in (a)). Reprinted from Optiz et al., [231] with permission. Copyright 2018. Springer Nature.

utilization of 60%, went through a severe power-drop (to 450 mW) after 237 h. This performance loss was due to Ni oxidation and agglomeration, which caused Ni expansion and eventually induced the anode/electrolyte delamination and depletion of percolation pathways [243].

In BSE, primary electrons interact elastically with the objective surface and scatter to a large angle towards 1 μm depth in the sample. BSEs energy is more than 50 eV, and the resulted image provides an accurate composition contrast; a higher atomic number leads to a brighter image [12,244]. BSE-SEM is another tool for investigating Ni agglomeration [103,245], secondary phase formation, and other common degradations. For instance, Khan et al. [103] evaluated the morphological changes of a Ni-SSZ anode functional layer (AFL) during accelerated aging by performing a long-term operation at 900 °C for 1000 h in an H_2–3%H_2O atmosphere with a single anode-supported flat-tubular SOFC. Fig. 26 (a) and (b) demonstrate how Ni particles expanded after 1000 h of operation [103]. In another study using BSE-SEM, Lee et al. [246] studied the durability of double perovskite structured $NdBa_{0.5}Sr_{0.5}Co_{1.5}Fe_{0.5}O_{5\text{-}\delta}$ (NBSCF) cathode in comparison with the single perovskite structures $Ba_{0.5}Sr_{0.5}Co_{0.8}Fe_{0.2}O_{3\text{-}\delta}$ (BSCF). They performed the durability test in the wet and dry cycling mode (WDCM), which consisted of supplying dry air for 12 h and afterward switched to wet air (10 vol% H_2O) for 10 h in a galvanostatic mode under 0.18 A cm^{-2} at 650 °C. Fig. 26(c–d) and (e-f) illustrate the fresh and post-mortem BSE-SEM images of BSCF and NBSCF cathodes, respectively. Despite the well-durable behavior of NBSCF, there was a serious agglomeration in the BSCF cathode due to the particle growth and presence of Sr enriched phases [246].

4.2.2.2. *Transmission electron microscopy.*

Unlike the SEM technique, the electron beam passes through the sample in the transmission electron microscopy (TEM) as the sample is ultrathin and electron transparent. TEM provides a higher resolution and the ability to study the crystal structure of the specimen. In this regard, Chen et al. [247] used the TEM to examine the effect of gas humidity on LSM/YSZ cathodes' degradation. Fig. 27 (a) and (b) represent the unoperated and the operated cells in H_2-20% H_2O atmosphere at 800 °C for 120 h in a constant current density of 0.75 A cm^{-2}, respectively. Before the operation, there was no sign of nanoscale MnO_x, SrO_x, or La_2O_3 secondary phases, and the TBP area remained intact. However, after the process, TBPs hosted the nano-voids, propagating inward along the LSM/YSZ interface. Moreover, amorphous material filled the voids region due to the formation of secondary phases originating from the mobile OH^- and Mn ion species [247].

4.2.2.3. *Atomic force microscopy.*

Atomic force microscopy (AFM) is another essential tool in evaluating surface roughness and morphology to examine the degradation process at the components' surface, such as Si poisoning, Sr segregation, and formation of secondary phases like $SrZrO_3$. [223,248,249]. He et al. [75] used the AFM technique to study the LSCF/YSZ interfaces before and after polarization at 750 °C and 1000 mA cm^{-2}. Fig. 28 (a) illustrates the interface after 1 h polarization, without any marks on the YSZ electrolyte surface. However, a considerable amount of crater-shape marks was observable after 12 h of polarization Fig. 28 (b). These marks became deeper and larger after 100 h of polarization in Fig. 28 (c), which indicated the formation of the $SrZrO_3$ phase on the YSZ electrolyte surface [75].

4.2.2.4. *Focused ion beam-scanning electron microscopy.*

In addition to the 2D images, it is essential to have 3D images for studying the degradation of SOFCs. The focused ion beam-scanning electron microscopy (FIB-SEM), a cut-and-image technique, provides flawless volumetric data and opens the doors for generating 3D images of SOFC

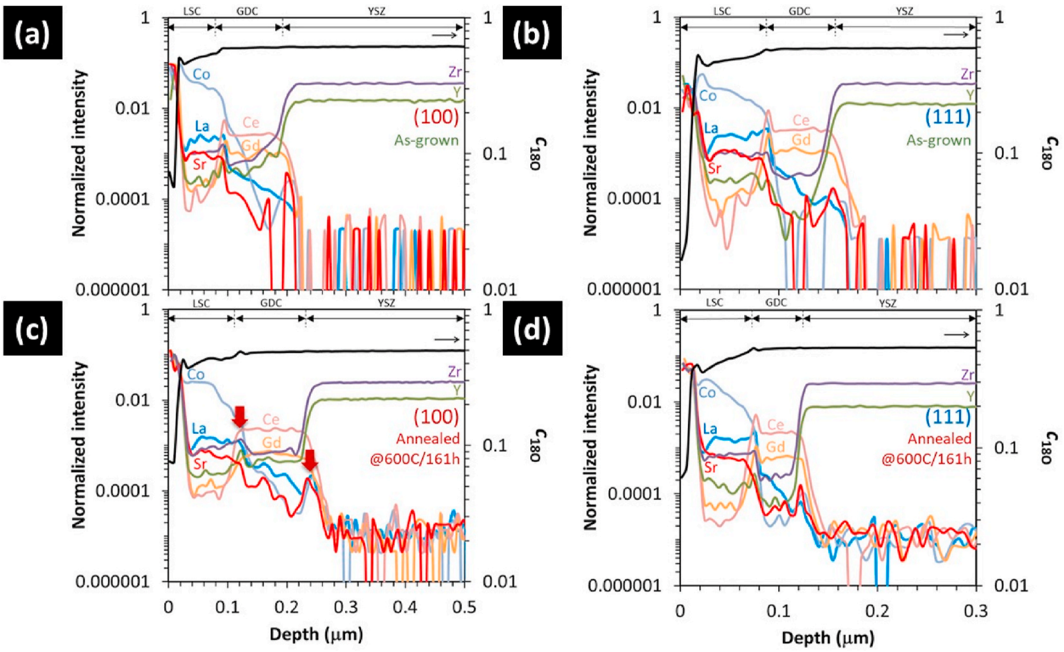

Fig. 23. SIMS elemental depth profiles showing the normalized intensities of the metal cations (primary y-axis) and the corrected fraction of the 18O isotope tracer (secondary y-axis) for (a) as-grown LSC/GDC/YSZ (100), and (b) as-grown LSC/GDC/YSZ (111). (c) and (d) depict the corresponding SIMS elemental depth profiles after annealing in air at 600 °C for 161 h. Arrows indicate peaks located at interfaces. Reprinted from Develos-Bagarinao et al., [235] with permission. Copyright 2020. Elsevier.

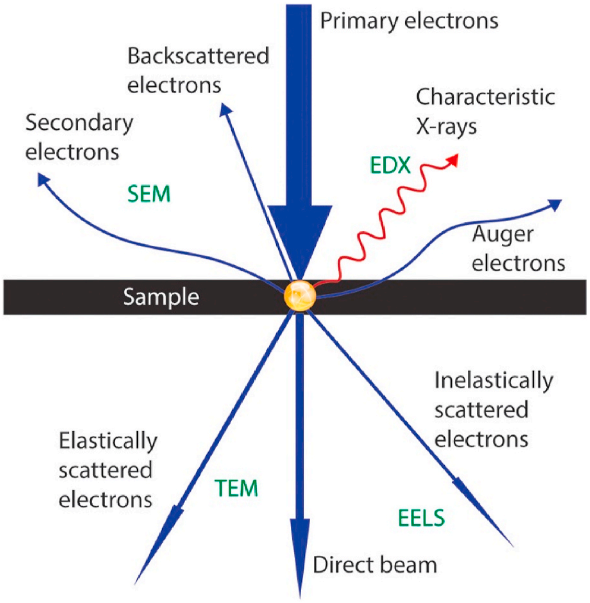

Fig. 24. Interactions between the electron beam and the sample. Scanning electron microscopy (SEM) analyses secondary and backscattered electrons, whereas transmission electron microscopy (TEM) focuses on transmitted electrons. Reprinted from Jouttijärvi et al., [12] with permission. Copyright 2018. John Wiley and Sons.

microstructure. There is a schematic configuration of FIB-SEM and a low-magnification image of a SOFC with a trench in Fig. 29(a–b) [250]. Several studies used this 3D reconstruction technique to examine the Sr segregation [251], Ni agglomeration [105,252], S poisoning [253], and other deterioration processes in the SOFCs [12,250]. For example, Wankmuller et al. [254] studied the formation of insulating $SrZrO_3$ phase for GDC/YSZ electrolyte. They combined the 2D FIB-SEM images of primary and secondary phases at 1100, 1200, 1300, and 1400 °C with a 3D FIB-SEM reconstruction (1300 °C). Fig. 29(c–d) demonstrates the direct contact between the pore phase and $SrZrO_3$. This direct contact caused the $SrZrO_3$ formation at the interface due to Sr gas diffusion during the cathode sintering [254].

4.2.3. Structural characterization (Macroscopy techniques)

4.2.3.1. Thermogravimetric analysis and differential scanning calorimetry. A different technique from spectroscopic ones to estimate the structural stability and formation of secondary phases caused by different degradation mechanisms, such as Cr poisoning and Sr segregation, is Thermogravimetric analysis (TGA) [219,255,256]. This analysis can be performed in different atmospheres to provide the desired condition for testing the stability and durability of a SOFC component. For instance, a lump of fused Cr_2O_3 can bring the required conditions to study cathode's Cr poisoning behavior [257]. After setting the desired parameters, the stability and poisoning resistivity can be estimated by analyzing the weight changes of the component [258,259]. The differential scanning calorimetry (DSC) is also helpful in examining the degradation, such as the formation of Sr phases, by showing the phase transition endothermic/exothermic peaks [260,261].

4.2.3.2. Dilatometry. Thermal expansion behavior is one of the key factors in SOFC's long-term durability to ensure the TEC compatibility of SOFC components as well as structural thermal stability. Dilatometry measurement is a functional tool to analyze the linear thermal expansion dynamic of the SOFC components at high temperatures [262,263]. Niu et al. [204] used the dilatometry measurements in the H_2 atmosphere to choose the most thermally compatible anode for LSGM electrolyte in cell fabrication [204]. In another work, Khan et al. [264] studied the effect of thermal cycling on the SOFC cathode degradation by dilatometry technique. A palette of LSCF-GDC cathode was analyzed with a dilatometer in the temperature range of 400–800 °C and a heating rate of 200 °C/h for 10 thermal cycles. The dilatometry data illustrated a decreasing trend in the cathode TEC as the thermal cycling proceeded, suggesting an irreversible deformation and eventually causing

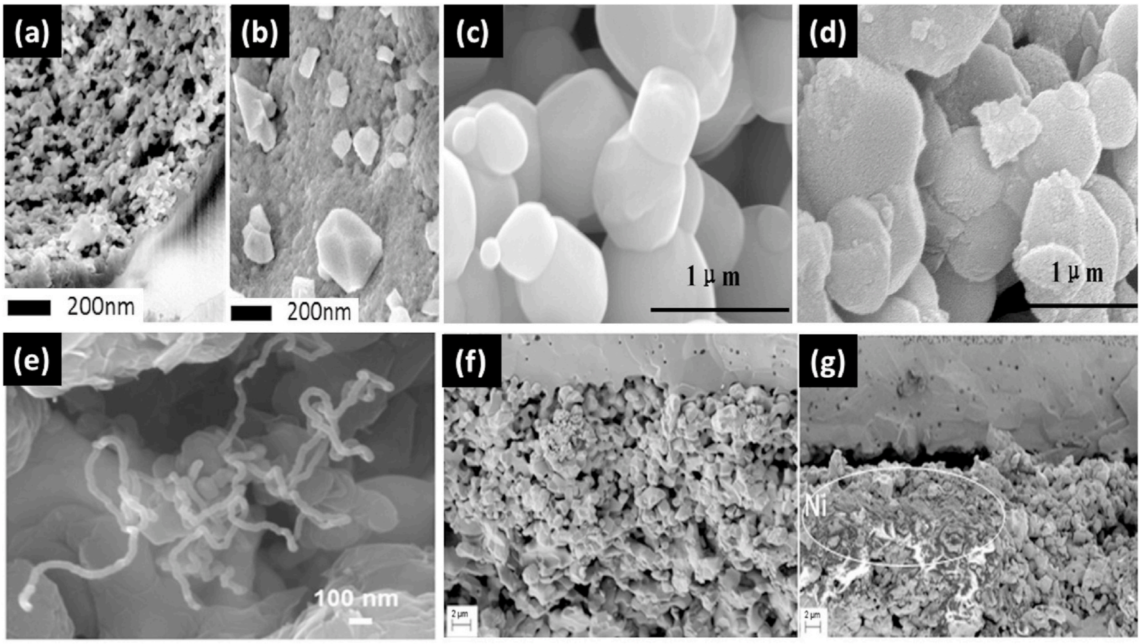

Fig. 25. SE - SEM micrographs of (a) and (b) Cr poisoning in LSM cathode, Reprinted from Tucker et al., [237] with permission. Copyright 2017. Elsevier. (c) and (d) S poisoning in LSCrM anode, Reprinted from Li et al., [242] with permission. Copyright 2017. Elsevier. (e) carbon formation in Ni electrodes after the performance test in CH_3, Reprinted from Lee et al., [239] with permission. Copyright 2016. Elsevier. and (f) and (g) Ni agglomeration in anode/electrolyte interface. Reprinted from Torrell et al., [243] with permission. Copyright 2017. Elsevier.

delamination and cell degradation [264].

4.2.3.3. Tensile strength measurement. Studying mechanical stability is one of the major concerns in SOFCs since poor mechanical strength in the electrolyte, interconnects, or sealants cause gas leakage and mechanical failure [67]. One of the most common methods to estimate the bonding strength is the tensile test [265]. As an example, Li et al. [266] evaluated the effect of Al_2O_3 fibers on the mechanical properties of compressive seals. Fig. 30 (a) depicts the tensile curves of pure (F0), 20 wt% fiber (F20), and 50% wt% fiber (F50) sealants, which F0 and F50 showed the highest tensile strength and ductility, respectively. Tensile strength clearly dropped, while flexibility improved as fiber content increased for fiber-reinforced seals [266]. In another research, the tensile test examined the mechanical properties of 3YSZ electrolyte with 75 μm thickness. Fig. 30 (b) exhibits the photos of the samples after the tensile test. Results revealed that the mechanical stability of a 75 μm thickness of a 3YSZ electrolyte is comparable with a 150 μm-8YSZ electrolyte [267].

4.2.3.4. Flexural strength measurement. Another essential mechanical feature of SOFC components is flexural strength, which defines their ability to withstand bending loads by a three- or four-point bending test. Fig. 31 (a) presents a schematic of a three-point bending test in which d, D, and L are the diameter of the loading tool, the diameter of the identical support cylinders, and the distance between the centers of the cylinders, respectively [268]. Morales et al. [269] used the three-point bending test to determine the effect of using AFLs (NiO-SDC) on anode-supported microtubular SOFCs by conducting a three-point bending test. The results of mechanical and electrochemical tests (shown in Fig. 31 (b)) of three cell configurations with different numbers of AFLs revealed that the cell with a single-layer AFL of 50:50 wt% NiO: SDC and a thickness of 12 μm performed best (0.52 W cm^{-2}) at 650 °C with hydrogen as fuel and air as oxidant [269].

4.3. Modeling

As a cost-effective method, modeling is a notable way to better understand the SOFC performance, which leads to optimizing and controlling the SOFC efficiency and lifespan. A 4xn optimization matrix, in respect to electrolyte, anode, cathode, and interconnect, defines the SOFC performance to obtain desirable properties, including proper chemical compatibility, prominent electrical conductivity and catalytic activity, as well as thermal and mechanical stability [139,270–273]. Moreover, a complete study of the SOFCs' phenomena demands a multidisciplinary methodology. Chemical processes, electrical conduction, ionic conduction, gas-phase mass movement, and heat transfer all occur at the same time and are intimately coupled. Hence, implementing conservation and constitutive laws and the kinetics of the chemical reactions is essential. Besides, it is consequential to consider the different factors of degradation mechanisms to adopt the modeling strategy in SOFC deterioration issues, such as microstructural changes, poisoning, formation of secondary phases, etc. [274,275]. Table 2 summarizes some of the different modeling techniques for investigating the SOFC failure mechanisms.

There are several numerical studies for optimizing the SOFC components' microstructure to enhance durability [103,278,288,289]. Various computational methods, such as two particle method, finite element model, phase-field model, etc., are available to study the Ni coarsening process [290]. For instance, Zhu et al. [276] studied how microstructure transformations of Ni-YSZ anode and YSZ electrolyte affect the SOFC degradation behavior by a Multiphysics model with the coupling of gas transports, electrochemical reactions, and electrical current conductions. They found that Ni coarsening causes more than 1%/1000 h degradation rate in the long-term cell performance. They also recognized a reduction in YSZ conductivity, from 5.45 S m^{-1} to 4.30 S m^{-1} in the first 500 h of SOFC performance due to its cubic-to-tetragonal phase transformation [276]. Another detrimental microstructural change is the formation of secondary phases and cation segregation in cathodes. In this regard, *Choi* et al. [223] used the density functional theory (DFT), which enables the prediction and analysis of material properties using quantum mechanical principles, to calculate the charge distribution and Oxygen vacancy formation energies to minimize the Sr segregation in SSC cathode. Similarly, a combined DFT and molecular-based theoretical technique was applied to calculate the

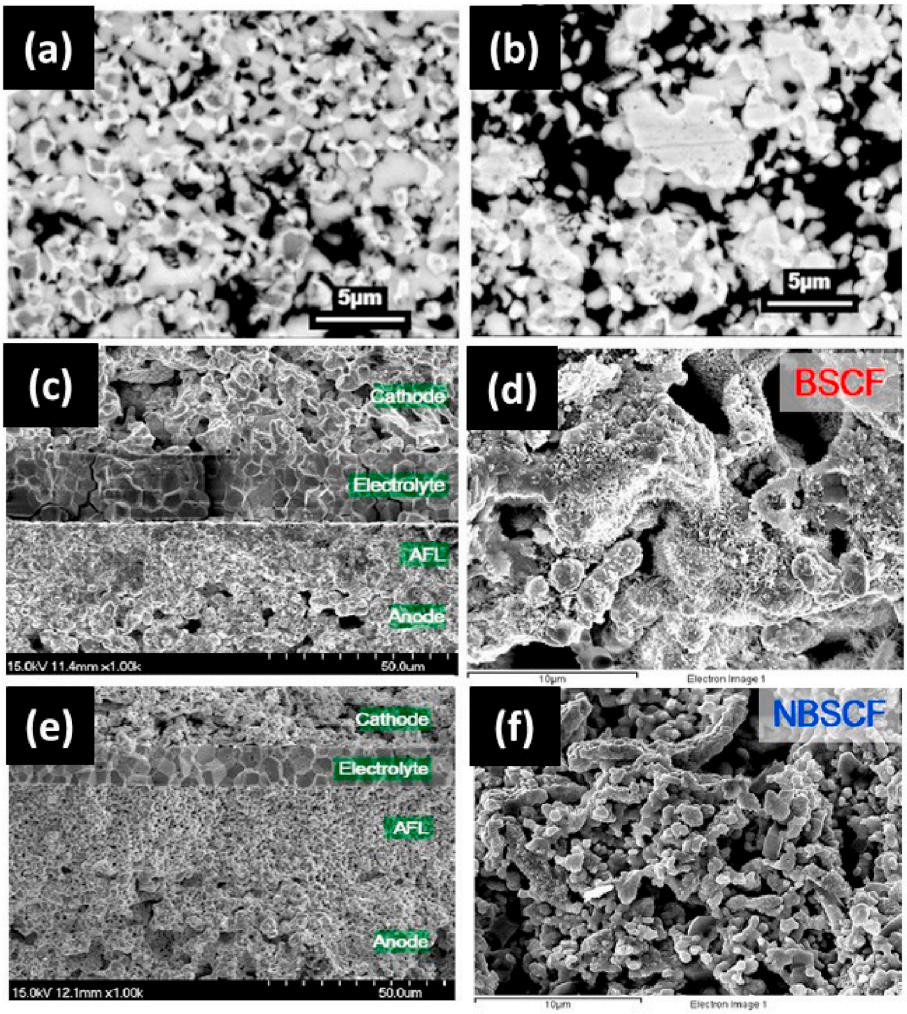

Fig. 26. BSE-SEM images of (a–b) Ni agglomeration in Ni-SSZ anode AFL before and after 1000 h of aging, Reprinted from Khan et al., [103] with permission. Copyright 2018. Elsevier. (c–d) Sr segregation in BSCF cathode, and (e–f) resistivity to Sr segregation in NBSC cathode. Reprinted from Lee et al., [246] with permission. Copyright 2016. Elsevier.

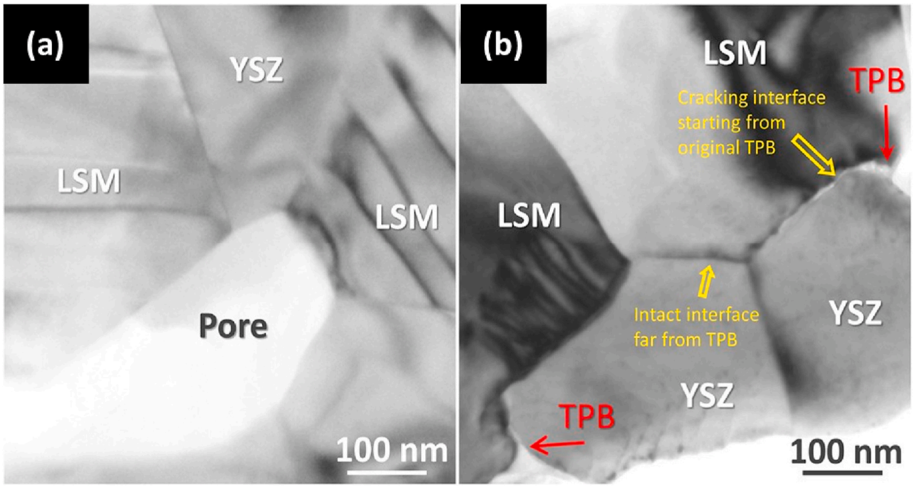

Fig. 27. Representative TEM image of (a) the original TPB region and the LSM/YSZ interface in the fresh cell and (b) the active layer of cell operated for 120 h. The interfacial defects initiate from the original TPBs, while the LSM/YSZ interface and YSZ/YSZ grain boundaries initially remain intact. Reprinted from Chen et al., [247] with permission. Copyright 2019. Elsevier.

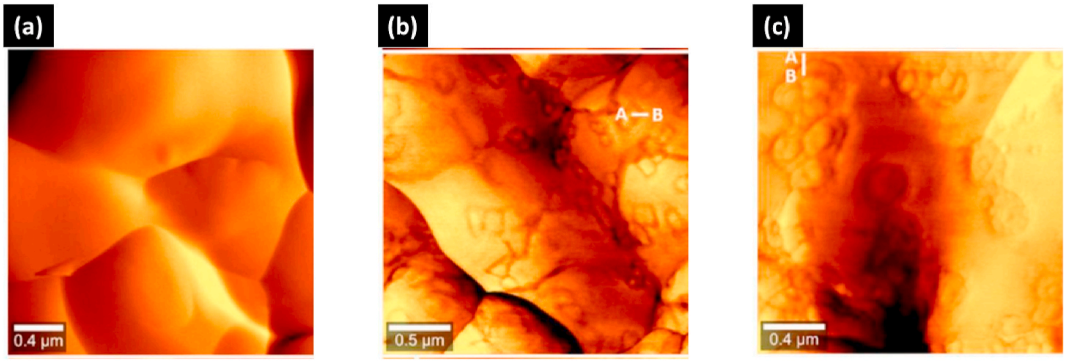

Fig. 28. AFM micrographs of the YSZ electrolyte surface in contact with directly assembled LSCF electrode after polarization at 750 °C and 1000 mA cm^{-2} for (a) 1 h, (b) 12 h, and (c) 100 h. LSCF electrode was removed by acid treatment. Reprinted from He et al., [75] with permission. Copyright 2018. IOP Publishing.

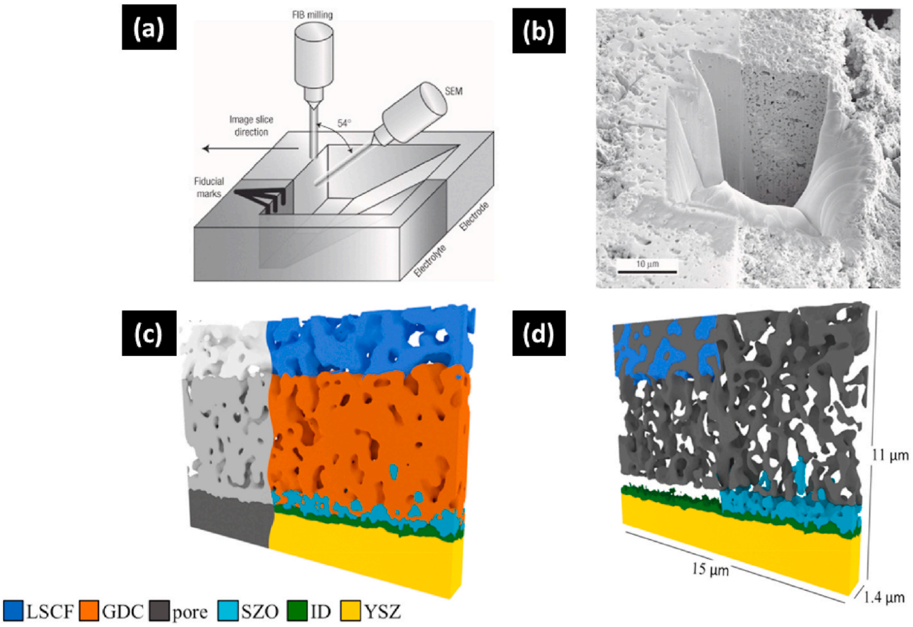

Fig. 29. (a) schematic of FIB-SEM analysis, (b) The fuel cell was first cut and polished, leaving a cross-sectional surface with the anode, electrolyte, and cathode exposed. The FIB was then used to mill a rectangular trench into this surface in the anode's vicinity. A series of SEM images were acquired from one of the trench sidewalls as the FIB 'shaved' away material from this surface. Reprinted from Wilson et al., [250] with permission. Copyright 2006. Springer Nature. Visualization of reconstructed 3D structure (GDC sintering temperature of 1300 °C). (c) Representation of the whole structure (10.7 × 14.7 × 1.4 μm^3) showing the gain in information achieved by the presented method. (d) LSCF, pore phase, SZO, ID, and YSZ revealing direct contact between the pore phase and SZO. The contact between SZO and the pores shows that a Sr gas diffusion through the pores during cathode sintering leads to SZO formation at the interface. There is no contact between the pore phase and ID or YSZ, revealing that SZO is formed during sintering developing a layer between pore and ID. Reprinted from Wankmuller et al., [254] with permission. Copyright 2017. Elsevier.

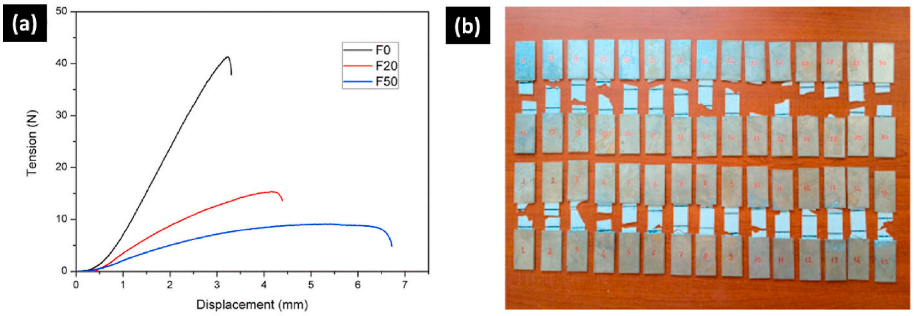

Fig. 30. (a) The tensile curves of pure and Al_2O_3 fiber-reinforced sealants. Reprinted from Li et al., [266] with permission. Copyright 2019. Elsevier [266]. (b) Photograph of 3YSZ samples after conducting the tensile test. Reprinted from Celic et al., [267] with permission. Copyright 2015. Elsevier [267].

energetics for oxygen vacancy formation in $PrBaCo_2O_{5+\delta}$ (PBCO) cathode for a better understanding of Ba segregation [277]. Furthermore, modeling and numerical studies are also used to determine carbon resistivity [278,291,292], S [122,279,280,291,293], and Cr poisoning [279], along with the thermal stress [281–283] and mechanical strength [294]. Darvish et al. [295] studied the Cr poisoning effects in a humidified atmosphere on the phase stability of the LSM/YSZ system by the CALPHAD (calculation of phase diagrams) approach. Thermodynamic simulation results demonstrated the destructive effect of Cr-containing humidified air on the perovskite phase stability and electronic conductivity. This detrimental impact is due to the diffusion of volatile Cr^{+6} species, CrO_3 and $CrO_2(OH)_2$, into the perovskite structure and substitute at B-sites, causing a decrease in Mn concentration and formation of Mn oxides secondary phases on the TBPs of LSM

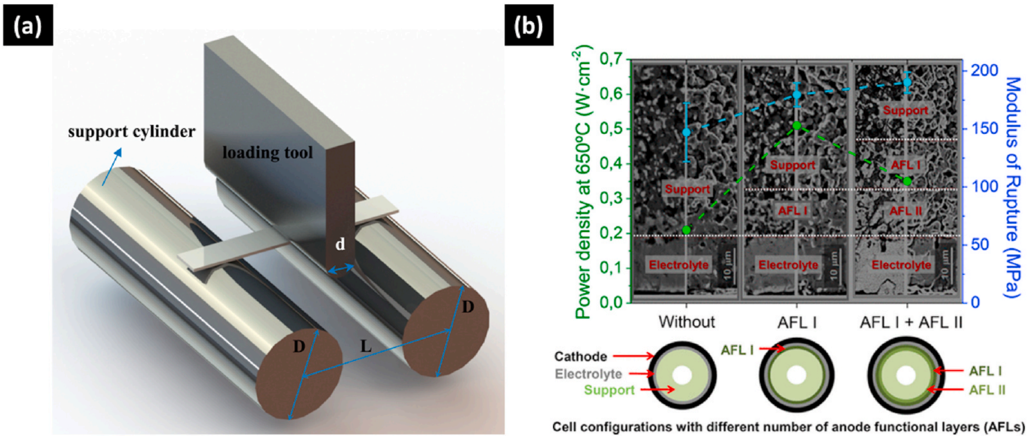

Fig. 31. (a) schematic of three-point bending test. Reprinted from Timurkutluk et al., [268] with permission. Copyright 2018. Elsevier [268]. (b) mechanical and electrochemical results of three cells with different numbers and compositions of anode functional layers. Reprinted from Morales et al., [269] with permission. Copyright 2018. American Chemical Society [269].

Table 2
A summary of different modeling techniques to study degradation mechanisms in SOFCs.

Study case	Modeling Method	Degradation Mechanism	Ref.
microstructural evaluation of Ni-YSZ anode, YSZ electrolyte, and SS430 interconnect	Multiphysics modeling	Ni coarsening (anode), phase transformation (electrolyte), and oxidation (interconnect)	[276]
double perovskite PBCO cathode	DM and DFT simulation	cation segregation (Ba^{2+})	[277]
GDC/SSC cathode	DFT	cation segregation (Sr^{2+})	[223]
porosity optimization of porous GDC electrolyte	finite element and Multiphysics modeling	carbon deposition	[278]
anode supported SOFC with Ni-cermet anode	lumped volume model	S poisoning	[122]
LSM cathode	CALPHAD method	combined Cr and S poisoning	[279]
LSCF	CALPHAD method	secondary phase formation and S poisoning	[280]
planar anode-supported cell	finite element method and Multiphysics modeling	mechanical failure	[281]
planar anode-supported SOFC with functionally graded electrodes	Multiphysics model	thermal stress and mechanical failure	[282]
2D functionally graded electrodes	Multiphysics model (COMSOL software)	thermal stress and mechanical failure	[283]
Ni catalyst with transition metal doping (Cu, Rh, Pd, Ag, Pt, Au)	DFT	S poisoning	[284]
Full-stack SOFC	Multiphysics modeling (FLUENT software)	creep strain and mechanical failure	[285]
Full-stack SOFC	Multiphysics modeling (COMSOL software)	Ni coarsening in the anode, Cr poisoning in the cathode, and corrosion in the interconnect	[286]
Glass composite sealant/ Crofer 22APU interconnect diffusion couple.	Multiphysics modeling (COMSOL software)	Thermal stress and leakage	[287]

cathode [295]. In another report, Hwang et al. [284] studied the thermodynamic stability of the Ni-based alloys against S poisoning by DFT. They examined the doping role of transition metals (Cu, Rh, Pd, Ag, Pt, and Au) into a Ni catalyst on adsorption of S compounds and H_2S decomposition. Multiphysics modeling is also a valuable method to evaluate the mechanical performance of SOFCs. Guo et al. [285] conducted a thermo-mechanical analysis using a multiphysics model to study the impact of creep on the mechanical degradation of all SOFC components during 10,000 h. The results showed that the creep strain is minor for electrolyte/cathode, so it is possible not to consider it for mechanical assessments [285]. In another work, Rizvandi et al. [286] developed a 3D multiscale full-stack model considering Ni particle coarsening in the anode, Cr poisoning in the cathode, and corrosion in the interconnect as deterioration phenomena. The model can assess the operation of 38,000 h within 1.4 h, and it is verified by the experimental data for a steady-state functioning of an 18-cell Jülich Mark-F stack [285].

5. Durability, the state-of-the-art

Many efforts have been made to improve SOFC performance, but only a few attempts reached exceptional results in both power density and stability, simultaneously [295–298]. Most of the state-of-the-art published literature on SOFC with high power densities over 2 W cm^{-2} in the temperature range of 650–800 °C did not address the stability issues or only reported a short-term durability test, without any harsh conditions that causing degradation [295,298–303], listed in Table 3. To date, many review papers had discussed the high performance of solid oxide fuel cells in the power density area. However, there is no comprehensive review covering the recent developments in SOFC stability. Therefore, this section reviews the most recent attempts to enhance SOFC stability. Table 4 presents some of the most recent literature in the field of SOFC stability improvement.

Perovskite oxides are one of the attractive materials for SOFC research due to their mixed ionic and electronic conductivity and high catalytic activities [304]. Their ABX_3 mixed structure contains rare earth and alkaline earth metals at the A-site and transition metals at the B-sites, where A-site cations are bigger in size than B-site cations and have the same size as X-site anions, shown in Fig. 32 [305]. In general, the ideal perovskite has a face-centered cubic (FCC) structure at room temperature. However, this structure can become distorted as a result of the formation of oxygen/cationic vacancies formation and angles readjustment between cations and oxygen. A-sites deficiencies result in cationic vacancies, which give rise to a better ionic conductivity for keeping the overall charge of the structure neutral. On the other hand,

Table 3

A summary of published literature of high power density SOFCs without significant durability. U, T, t, and G represent the applied regime value, temperature, duration, and Galvanostatic regime.

Cell design (anode|electrolyte |cathode)	Test condition oxidant/ fuel	Conductors	Temperature (°C)	Power density (W cm^{-2})	Stability regime/U/T/t	Ref.
SDCN40*|SCSZ**|PrO_x	oxygen/H_2	O^{2-}	700	2.00	–	[300]
Ni-YSZ|YSZ/ESB***| LSM-ESB	air/wet H_2	O^{2-}	700	2.08	–	[298]
Ni–YSZ|YSZ|icn-LSMESB****	dry air/wet H_2	O^{2-}	750	2.00	–	[302]
Ni-YSZ|YSZ|GDC|LSC-GDC	air/H_2	O^{2-}	650	3.01	G/300 mA cm^{-2}/650 °C/ 25 h	[299]
anodized aluminum oxide|Ni-YSZ|YSZ|GDC| LSCF-YSZ	air/H_2	O^{2-}	650	2.5	G/200 mA cm^{-2}/600 °C/ 5.5 h	[301]
NiO-YSZ|YSZ|GDC|LCaF****-GDC	synthetic air/wet H_2	O^{2-}	800	4.4	–	[303]

*Ni and Sm-doped ceria, ** SCSZ: Sc_2O_3 stabilized zirconia, *** ESB: $Bi_{1.6}Er_{0.4}O_3$, **** icn-LSMESB: in situ co-assembled nanocomposite LSM-$Bi_{1.6}Er_{0.4}O_3$, ***** $La_{0.65}Ca_{0.35}FeO_{3-\delta}$.

multivalent elements for the B-site are selected according to their potential for redox reactions, based on oxygen/anion partial pressure over the SOFCs operation [304,306–308].

Incorporation of high valance transition metals, such as Mo, Nb, Co [309], and Ta [310–312], on the B-site of perovskite electrodes, leads to a stable cubic structure. This feature can be considered as one of the answers to the perovskites' stability issues, including inferior chemical stability and considerable volume changes [308], especially in the symmetric design of solid oxide fuel cells [310,313,314]. To point out, BSCF is a high potential cathode material at low temperatures, owing to its high energy output and oxygen diffusion rate. Substitution of Mo in the cubic structure of BSCF can enhance its stability in reducing atmospheres and make it a suitable electrode for both anode and cathode in a symmetrical solid oxide fuel cell. A long-term stability test in a constant voltage of 0.7 V at 700 °C revealed no change in the power density after 115 h in a humidified H_2 atmosphere, and it remained at 418 mW cm^{-2} [254]. Mo doping is also used for the LSCF symmetrical electrode to develop both structural stability and catalytic activity [315]. Moreover, this Mo substitution with Fe reduced the TEC from 16.6 to 12.9 $\times$ 10^{-6} K^{-1} and made it more compatible with LSGM electrolyte. A stability test of $La_{0.6}Sr_{0.4}Co_{0.2}Fe_{0.7}Mo_{0.1}O_{3-\delta}$ (LSCFM) single cell was performed under a constant 0.05 A at 850 °C in liquid petroleum gas (LPG) for 40 h, and the voltage output ($\sim$ 0.9 V) was almost steady during that time. Hence, this LSCFM electrode can tolerate carbon deposition and S poisoning as well [316].

Another approach to enhance the redox stability of SOFC is Ce doping. HTXRD analysis from RT to 1000 °C confirmed the promising thermal stability of the hybrid $Gd_{0.65}Sr_{0.35}(Co_{0.25}Fe_{0.75})_{0.9}Ce_{0.1}O_{3-\delta}$ (Ce-GSCF) electrode when no other phases emerged in the results. Furthermore, Ce doping decreases the GSCF TEC and enhances the thermo-mechanical stability of the electrode. The Ce-GSCF symmetrical single cell showed no degradation after 180 h operation at 0.7 V in 700 °C and humidified H_2, proving the GSCF perovskite material's improved stability [228].

A third method is to use Sn as a metal dopant in $BaCo_{0.7}Fe_{0.3}O_{3-\delta}$ (BCF) oxide to preserve its cubic structure and provide strong exchange surface properties and oxygen bulk diffusion [317,318]. Xia et al. [319] investigated the long-term stability of a novel BSF cathode-Sn doped ($Bi_{0.5}Si_{0.5}Fe_{0.9}Sn_{0.1}O_{3-\delta}$) material. After the 100 h of continuous testing at 0.6 V and 650 °C, the degradation rate was 1%, from 468 mW cm^{-2} to 463 mW cm^{-2}. The SEM images after the stability tests showed no cracks or delamination. This stable morphology resulted from compatible cathode TEC (12.9 $\times$ 10^{-6} K^{-1}) with the CGO (13.2 $\times$ 10^{-6} K^{-1}) electrolyte. Sn doping increased the average binding energy of BSF and led to a smaller TEC than the conventional BSF [319]. Likewise, TEC can be optimized through Ca doping as well. A study by Xiang et al. [320] reported that a layered perovskite $Eu_{1-x}Ca_xBaCo_2O_{5+\delta}$ (EC_xBC) could show a low TEC with a 0.2 Ca fraction. By introducing Ca^{2+} ions into the Eu^{3+} sites, the oxidation states of cobalt ions can increase to preserve electrical neutrality, raising the polarization force of the cobalt ions. This increased polarization force weakened the ionicity of Co–O bonds, leading to reducing the TEC (16.9 $\times$ 10^{-6} K^{-1}) and making it more compatible with the electrolyte. The slow degradation of power output (2.3%) in 0.5 V and 700 °C for 100 h had arisen from the TEC compatibility of the components, which prevented the thermomechanical strains [320].

The doping technique can also be used for enhancing CO_2 tolerance in cathodes. The selected dopants should have (1) high acidity, (2) high valence state, and (3) high average bonding energy [321]. In research by Zhang et al. [322], Hf was used to improve the stability of $SrFeO_{3-\delta}$. The cathode was exposed to 1% vol CO_2 for 60 h for the evaluation of CO_2 tolerance. The ASR polarization values barely increased during the process, indicating that the CO_2 adsorption occurred without perovskite's surface structural destruction. Additionally, the ASR polarization returned quickly to the original value after the CO_2 flow switched off, showing that the CO_2 adsorption is reversible at active ORR sites. This improved chemical stability was due to the doping of redox-inactive Hf cation at the Fe site of SF [322]. This strategy was used with alkaline metals by Rehman et al. [323] for $SrFe_{0.8}Nb_{0.1}Ta_{0.1}O_{3-\delta}$ (SFNT) cathode, resulting in the *in-situ* formation of alkali metal carbonates at the surface with the highest performance cobalt-free single-phase cathode that has been published to date (0.12 Ωcm^2 ASR at 600 °C). The stability test evaluated the CO_2 tolerance of the SFNT-Li doped cathode in 10% CO_2 at 600 °C for 50 h. The degradation rate was $\sim$ -8.1 $\times$ 10^{-12} W cm^{-2} h^{-1}, making this cathode a promising component in the CO_2 environment. This boosted performance has arisen from the O_2 released during alkaline metal carbonation, increasing the oxygen partial pressure and forming an *Oxygen cloud* at the cathode surface. This cloud facilitated the surface exchange process towards CO_2 and protected the cathode surface [323].

Moreover, Ga-doping can contribute to improving the structural stability of Fe-based perovskite cathodes [324]. Recently, a Ga-doped SFM cathode was reported that possessed an acceptable CO_2 tolerance. In this cathode, B-site Fe was substituted by Ga, which reduced the SFGM affinity towards CO_2 chemical adsorption. The durability test was performed under 16A at 750 °C, 97 h in air, and 291 h in 5% CO_2. Regardless of the slight decrease in output voltage, results indicated a promising stable performance [73].

Ca doping can also improve CO_2 tolerance by partially replacing it with Ba in Ba-containing cathodes. This replacement results in stabilizing the perovskite structure and lowering the Ba enrichment at the cathode surface. The output voltage of Ca-containing $Ba_{0.95}Ca_{0.05}Co_{0.4}Fe_{0.4}Zr_{0.1}Y_{0.1}O_{3-\delta}$ (BCFZY) cathode decreased slightly after switching from air to air-1% CO_2 and maintained steady for 30 h under 400 mA cm^{-2} at 700 °C [325].

In addition to perovskite material, doping can improve the spinel-based SOFCs as well. In a recent work by Thaheem et al. [297], a Cu doped $(Mn, Co)_3O_4$ spinel cathode achieved a significant power density (2 W cm^{-2} at 800 °C) and excellent stability performance at the same time. The output voltage stayed steady during 300 h of the test under

Table 4

Some of the most recent research in improving the durability and stability of SOFC's components. G and P regimes represent galvanostatic and potentiostatic test modes, respectively. Moreover, U, T, t, and A represent the applied regime value, temperature, duration, and atmosphere.

Cell Design (Anode|Electrolyte |Cathode)	Test Condition Regime/U/T/t/A	Stability Evaluation			Conductor	Degradation/Solution	Ref.
		Performance Parameter	Initial Value	Final Value			
NiO-GDC| GDC|$Sm_{0.5}Sr_{0.5}CoO_{3-\delta}$	G/600 mA cm^{-2}/600 °C/ 250 h H_2	Voltage output (V)	0.728	0.721	O^{2-}	Delamination of Cathode Materials/Core-shell structure	[336]
		Power Density (mW cm^{-2})	1130	1127			
BSCFM|GDC|YSZ|GDC| BSCFM	P/0.7 V/700 °C/115 h H_2	Current Density Output (mA cm^{-2})	170	~ 170	O^{2-}	Carbon Deposition/Mo doping	[254]
		Power Density (mW cm^{-2})	418	418			
SSFTR7020|SDC|SSFTR7020 ($Sm_{0.7}Sr_{0.2}Fe_{0.8}Ti_{0.15}Ru_{0.05}O_{3-\delta}$)	G/0.43 mA cm^{-2}/800 °C/ 200 h H_2	Voltage Output (V)	0.65	~ 0.68		Ni Coarsening/Surface modification with Ru	[331]
		Power Density (mW cm^{-2})	~ 400	~ 476	O^{2-}		
NiO-YSZ|YSZ|GDC| $Sr_2Fe_{1.3}Ga_{0.2}Mo_{0.5}O_{6-\delta}$	G/16 A/750 °C/388 h (97 h in air and 291 h in 5 vol% CO_2)	Voltage Output (V)	~ 0.7	~ 0.7		CO_2 Poisoning/Ga doping at Fe sites	[73]
		Power Density (mW)	12000	12000	O^{2-}		
NiO-YSZ|YSZ|LSM-nanoYSZ	G/0.25 A cm^{-2}/750 °C/230 h H_2	Total Resistance (Ω cm^2)	0.460	0.468		Ni Coarsening/Surface Modification with nanoYSZ	[337]
		Voltage Output (V)	0.904	0.909	O^{2-}		
		Power Density (mW cm^{-2})	628	614			
NiO-BZCYYb-1711| BZCYYb-4411| BCaCFZY	G/400 mA cm^{-2} at 700 °C/ 35 h (oxidant: air + 1 vol% CO_2)	Voltage Output (V)	0.8	~ 0.8	H^+	CO_2 Poisoning/Ca doping	[344]
SSFTR72|SDC|SSFTR72 ($Sm_{0.8}Sr_{0.2}Fe_{0.8}Ti_{0.15}Ru_{0.05}O_{3-\delta}$)	G/300 mA cm^{-2}/800 °C/ 240 h H_2	Voltage Output (V)	~ 0.72	~ 0.72	O^{2-}	Mismatching TEC and Delamination/Surface modification with Ru Exsolution	[332]
LSCFM|SDC|LSGM|SDC|LSCFM ($La_{0.6}Sr_{0.4}Co_{0.2}Fe_{0.7}Mo_{0.1}O_{3-\delta}$)	G/0.025 V/700 °C/25 h Liquid Petroleum Gas	Voltage Output (V)	~ 0.75	~ 0.75	O^{2-}	S Poisoning/Mo doping	[316]
SFHf|SDC|SFHf ($SrFe_{0.9}Hf_{0.1}O_{3-\delta}$)	Polarization/600 °C/60 h air + 60 h in 1 vol% CO_2	ASR (Ω cm^2)	0.193	0.356	O^{2-}	CO_2 Poisoning/Hf doping	[322]
NiO-YSZ|NiO-YSZ|YSZ|LSCD|PrO_x-PNM ($PrNi_{0.5}Mn_{0.5}O_3$)	P/0.7 V/750 °C/600 h H_2+3% H_2O + direct Crofer contact	Power Density (mW cm^{-2})	460	459.73	O^{2-}	Cr Poisoning and $SrCrO_4$ formation/Surface modification with protection layer	[78]
Ni-YSZ|YSZ|CGO|SPN-A-PBC ($PrBa_{0.94}Co_2O_{5+\delta}$)	P/0.6 V/700 °C/120 h H_2	Current Density Output (mA cm^{-2})	~ 1700	~ 1700		Cathode Decomposition/ Surface engineering by Exsolution	[333]
		Power Density (mW cm^{-2})	1100	~ 1100	O^{2-}		
SFCoM|LSGM|GDC|LSCF ($Sr_{1.95}Fe_{1.4}Co_{0.1}Mo_{0.5}O_{6-\delta}$)	G/0.85 A cm^{-2}/750 °C/200 h H_2+C_3H_8 50 sccm	Voltage Output (V)	0.75	0.75	O^{2-}	Carbon deposition/Co doping	[345]
		ASR (Ω cm^2)	0.278	~ 0.278			
NiO-YSZ|YSZ|GDC| La, Pr, Nd, Sm, and Sr -LSM	P/0.7 V/700 °C/100 h H_2	Current Density Output (mA cm^{-2})	~ 0.46	~ 0.46	O^{2-}	Sr segregation/Multi doping with La, Pr, Nd, Sm, and Sr	[346]
Ni-SDC|YSZ|PBSCF ($PrBa_{0.5}Sr_{0.5}Co_{1.5}Fe_{0.5}O_{5+\delta}$)	G/0.254 A cm^{-2}/650 °C/ 120 h 97 vol% CH_4 + 3 vol% H_2O	Voltage Output (V)	0.73	~ 0.73	O^{2-}	Carbon deposition/Surface modification by infiltrating SDC to the anode	[347]
NiO-YSZ|YSZ|CGO| PBCaC ($Pr_{0.94}Ba_{0.7}Ca_{0.3}Co_2O_{5+\delta}$)	P/0.6 V/120 h/650 °C/ H_2+3% H_2O	Current Density Output (mA cm^{-2})	~ 1350	~ 1350	O^{2-}	Mismatching TEC in cathode/ Ca dopant	[348]
		Power Density (mW cm^{-2})	~ 800	~ 800			
NiO-BZCYYb|BZCYYb|LBCCF-BZCYYb ($La_{0.5}(Ba_{0.75}Ca_{0.25})_{0.5}Co_{0.8}Fe_{0.2}O_{3-\delta}$)	G/400 mA cm^{-2}/650 °C/ 100 h/humidified H_2 and dry air with 80 mL min^{-1}	Voltage Output (V)	0.76	0.76	H^+	Sr segregation/Ca doping	[349]
Ni–CeZr|Ni-YSZ|YSZ|YSZ-LSM|YSZ	P/0.6 V/850 °C/100 h/ humidified H_2 (for the first 20 h) and N_2+ ~ 17% Ethanol	Current Density Output (mA cm^{-2})	~ 100	~ 100	O^{2-}	Carbon deposition/Zr doping for ceria in Ni-ceria anode	[350]
Co@SFCoM|LSGM| GDC|LSCF	G/850 mA cm^{-2}/750 °C/ 200 h/C_3H_8 with 50 sccm	Voltage Output (V)	0.75	0.75	O^{2-}	Carbon deposition/Surface modification of anode with Co exsolution	[345]
Ni–YSZ/YSZ/GDC/BFP05	G/500 mA cm^{-2}/750 °C/50 h/H_2 with 100 mL min^{-1} and air + 2% CO_2	Voltage Output (V)	0.7	~ 0.7	O^{2-}	CO_2 poisoning/Pr doping	[11]

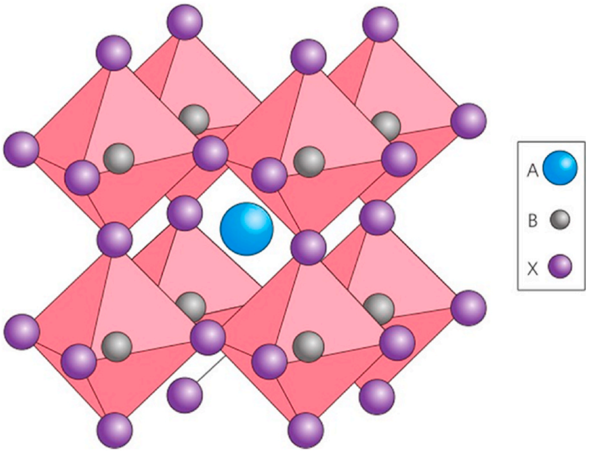

Fig. 32. Simple Perovskite structure with ABX_3 formula. Reprinted from Green et al. [305] with permission. Copyright 2014, Springer Nature.

constant 150 mA cm^{-2} at 750 °C [297]. The co-doping approach can also be a propitious approach for developing SOFC performance. Yun et al. [296] achieved one of the remarkable results by introducing both Dy and Y to B_2O_3 and combining it with conventional LSM, with a peak power density of 2.23 W cm^{-2} at 700 °C. The cell's output voltage was stable under 1 A cm^{-2} for 100 h at 700 °*C*, resulting from the cathode's stabilized structure [296]. Using co-doping in the $SrCoO_{3\text{-}\delta}$ (SC) cathode also reveals good resistance against CO_2 with a peak power density of 1563 W cm^{-2} at 650 °C. The co-doping was carried out by introducing Nd^{+3} to A-site and Nb^{+5} to B-site. The ASR values of $N_{0.2}$SNC before (0.08 Ωcm^2) and after (0.20 Ωcm^2) placing in 5% CO_2-air flow for 300 min showed a proper CO_2 tolerance performance, resulting from the relatively low oxygen vacancy concentration of $N_{0.2}$SNC that prevented the cathode from the carbonate formation on the surface by CO_2 [255].

Dopants can improve anode stability as well. A novel perovskite material was prepaid via introducing Ta on the B-sites of LSF, leading to a good stability performance after a 55 h test under constant 0.4 A cm^{-2} with H_2-50 ppm H_2S at 800 °C. Since Ta doping stabilizes the LSF lattice against decomposition in a reducing atmosphere, $LSFT_{0.5}$ would be secure from S poisoning and coking [310].

A different method to develop solid oxide fuel cell stability is surface engineering and microstructure optimization [326,327]. Exsolution is a surface modification approach by forming a solid solution incorporating catalytically active metal into the host lattice matrix under an oxidizing atmosphere. Later in the reducing conditions, the metal particles are exsolved on the surface of the host material [328]. This method prevents nanoparticles' agglomeration on the surface and provides a better surface distribution than conventional techniques [329,330]. Researchers discovered that surface engineering by a thin film conformal coating of a perovskite material with distinct nanoparticles in LSCF cathodes can hinder the Sr enrichment and segregation; thereby, enhancing the stability performance. A conformal coating of PNM with exsoluted PrO_x nanoparticles on a conventional LSCF cathode, designed by Chen et al. [78], showed a degradation rate of 0.04%/h, operating at 0.7 V with humidified H_2 and direct Crofer contact at 750 °C for more than 500 h. This duration is 10 times higher than the bare LSCF. The Sr-free nature of this coating made it less active against Cr contaminants, and at the same time, the PrO_x nanoparticles provided a significant amount of oxygen vacancies to boost the cell performance [78].

Moreover, a symmetrical SOFC is designed using Ru nanoparticles' *in-situ* exsolution with a considerable ASR of 0.11 Ωcm^2. Due to the stability tests under 0.43 A cm^{-2} for 200 h under wet H_2 at 800 °C, this electrode also exhibited perfect durability towards Ni coarsening in the reducing environment by maintaining its output voltage during the test [331,332]. In another report, $PrBa_{0.94}Co_2O_{5+\delta}$ (PBC) double perovskite was decorated by the PBC nanorods with good stability properties, and the morphology has not faced any changes during 120 h under 0.6 V at 700 °C [333], as it is represented in Fig. 33.

Surface modification with $PrO_{2-\delta}$ nanoparticles was also been applied for the LSCF cathode. The enhanced surface activity led to the $Sr_xCo_yO_z$ formation (Fig. 34), and the resulted LSCF/$Sr_xCo_yO_z$/$PrO_{2-\delta}$ heterostructure improved the cathode stability against Cr poisoning. This tailored cathode exhibited a competitive stability performance under 0.9 A cm^{-2} for 100 h at 600 °C [334]. In another research, Ozmen et al. [335] used the nano-ceria for catalyst infiltration of the LSM-GDC|YSZ|NiO-YSZ anode-supported cell via a single step deep-coating method to form a uniform and discrete decoration in the electrodes' active layer, close to the electrolyte interface. The infiltrated cell reached a reduction of up to 33% in the polarization resistance (0.275 Ω cm^2) compared to a bare sample (0.405 Ω cm^2) after ~300 h of EIS measurement at 750 °C using 300 sccm wet H_2 as fuel and 300 sccm air as oxidant under a constant current of 0.325 A cm^{-2}. The stability performance is improved as this technique limits infiltration/co-firing processes and minimizes nanocatalysts' morphology changes while maintaining an optimal concentration of catalytically active nanoparticles inside the active electrode region [335].

Core-shell structure cathodes are also a potential method to achieve better SOFC performance. One of the exceptional results belongs to Lee et al. [295], reaching 2 W cm^{-2} in power density at 550 °C and outstanding stability performance with a degradation rate of 0.00017 V h^{-1} at 550 °C under constant 1 A cm^{-2} for over 250 h by their core/shell-fiber-structured BSCF-GDC cathode. This outstanding performance was mainly owing to the tailored microstructure of the cathode [295]. Recently, the SSC cathode was optimized with a novel core-shell structure by the *in-situ* growth of homogenous SSC nanoparticles without using the conventional multi-step infiltration technique. The stability studies under a constant current density of 600 mA cm^{-2} in 600 °C for 200 h revealed that the voltage output (0.728 V) had

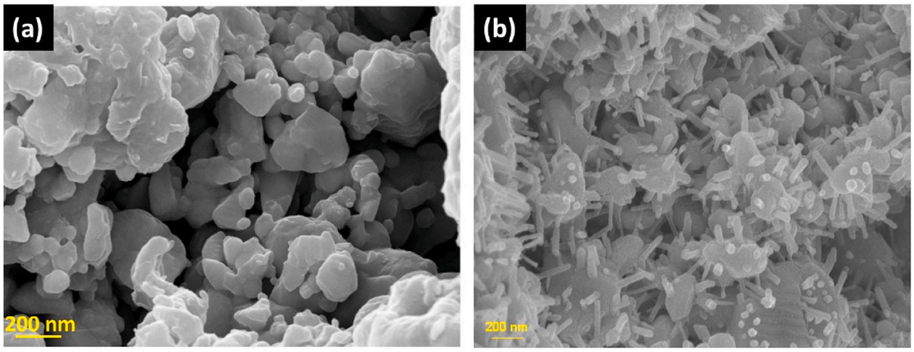

Fig. 33. SEM images of (a) A-PBC precursor composed of many irregular microscale particles, and (b) SPN-A-PBC cathode surface after 120 h stability test under 0.6 V at 700 °C. Reprinted from Lu et al., [333] with permission. Copyright 2019, Elsevier.

Fig. 34. Schematic diagram of the process of tailoring SOFC electrode microstructures by surface modification. Reprinted from Wang et al., [334]. Copyright 2020, American Chemical Society.

not changed during the test. This progress was attributable to the robust and continuous formation of SSC nanoparticles on the SSC backbone [336].

Muhoza et al. [337] used the surface engineering strategy for LSM-YSZ cathode by the infiltration of high surface area YSZ nanoparticles. This cathode's stability study was performed under constant 0.25 A cm^{-2} at 750 °C for over 230 h, and the result was 0.23%/100 h in the voltage output. The stable nature of YSZ nanoparticles inhibited the cathode decomposition and prevented YSZ scaffold particle reaction, saving the TPB sites and reducing the degradation rate [337]. SFM Cr resistance was also enhanced by $LaCoO_{3-\delta}$'s (LC) infiltration, which prevented SFM and Cr's direct contact. This cathode's polarization resistance remained steady under 400 mA cm^{-2} at 800 °C with a Cr source for 220 h [338]. LC was also used to enhance the Cr resistivity of BSCF-GDC with the exact mechanism and showed a stable low resistance under a current density of 400 mA cm^{-2} at 750 °C for 115 h with SUS430 interconnect [339]. Alloy nanoparticles can modify the electrode surfaces as well. A new double perovskite material for both anode and cathode is fabricated with the *in-situ* exsolution of Co–Fe alloy (CFA) nanoparticles on the surface of RP-SCFM (Ruddlesden–Popper structured oxide $Sr_3Co_{0.1}Fe_{1.3}Mo_{0.6}O_{7-\delta}$). When performing as the anode under the constant 400 mA cm^{-2} at 800 °C for almost 250 h in H_2-50 ppm H_2S, this electrode possessed a high resistance against S poisoning and coking. The S tolerance mechanism of this electrode is described in Fig. 35 $(OH)_o^\bullet$ is generated by the combination of water (from H_2 oxidation (2)) and RP-SCFM lattice oxygen ($O_o^\times$). Then, the generated $(OH)_o^\bullet$ species are stored in the oxygen vacancies ($V_o^{\bullet\bullet}$) of RP-SCFM (3). In the meantime, S species are formed from the adsorbed S on the surface of CFA nanoparticles (4), which can react with $(OH)_o^\bullet$ and be converted to S_2 and H_2 at the CFA nanoparticles/RP-SCFM interface (5). Thus, S poisoning would be minimized [340].

In another work, Ni–Fe alloy (NFA) nanoparticles were used to decorate the RP-PSNF (Ruddlesden-Popper $Pr_{0.32}Sr_{0.48}Ni_{0.2}Fe_{0.8}O_{3-\delta}$) electrode. The resulting anode exhibited an enhanced coking resistance under the constant 250 mA cm^{-2} at 800 °C in humidified C_3H_8 for 60 h since the output voltage has not changed. There was no carbon deposition on the anode surface after the durability test as well. This performance was due to the protection role of exsolved NFA nanoparticles anchored on the surface, which prevented the anode from coarsening [341].

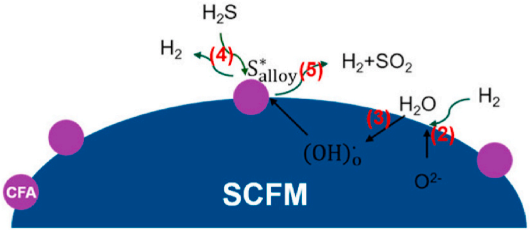

Fig. 35. Schematic showing the S tolerance of the RP-SCFM-CFA anode. H_2-50 ppm H_2S was used as fuel. Reprinted from Qiu et al., [340] with permission. Copyright 2020. American Chemical Society.

Interface engineering between cathode and electrolyte is another interesting technique to improve SOFC stability behavior and power density [342]. In research by Kim et al. [343], GDC/SSC-infiltrated cell showed a high tolerance to thermal degradation after a 200 h test under 0.4 A cm^{-2} at 650 °C. The modified cathode/electrolyte interface by forming a thin-film-like GDC interlayer with smaller grains size than that of the GDC matrix was the main reason for this improved stability [343]. This method was also used for tailoring the YSZ interface with $Bi_{1.6}Er_{0.4}O_3$ (ESB) nanopowder via screen printing technique, resulting in 2.1 W cm^{-2} at 700 °C. The stability evaluation resulted in an unchanged output voltage after 150 h of a test under 100 mA cm^{-2} at 700 °C since the interlayer blocks the elemental interdiffusion between layers [298]. One of the most recent strategies in this technique is to use the TEC offset strategy to eliminate the TEC mismatch between the cathode and the electrolyte. In this regard, Zhang et al. [262] made a $SrNb_{0.1}Co_{0.9}O_{3-\delta}$ (SNC) (TEC of 19–24 × 10^{-6} K^{-1} from room temperature to 800 °C) cathode composite with $Y_2W_3O_{12}$, which has a negative TEC of 7 × 10^{-6} K^{-1} from room temperature to 1100 °C. Furthermore, they induced an interfacial phase reaction between these two phases to provide better adhesion. This procedure not only leads to the development of the $SrWO_4$ interphase and the exsolution of Sr from the perovskite bulk phase but also creates A-site cation deficiency in the perovskite structure. This composite cathode exhibited an average TEC of 12.9 × 10^{-6} K^{-1} at 100–800 °C, extremely similar to that of the SDC electrolyte (~12.3 × 10^{-6} K^{-1}) and considerably lower than of the bare SNC (~20.5 × 10^{-6} K^{-1}) and other co-based perovskites. The electrochemical performance of the symmetric cell with the composite cathode and SDC electrolyte from the EIS measurement exhibited impressive stability after 200 h of test with a signal amplitude of 10 mV under open-circuit conditions at 600 °C in air and presented a constant R_p of 0.075 Ω cm^2 during the test. While the bare SNC electrode faced a significant performance degradation by increasing from 0.24 Ω cm^2 to 0.37 Ω cm^2. The synergetic effects of the lowered TEC, perovskite phase modification, and thermo-mechanical stability all contribute to the SOFC composite cathode's superior electrochemical performance and indicate a new route for future SOFC electrode design [262].

Apart from the traditional three-layer SOFCs, single-layer SOFCs (SLFC) have been presented as a new class, emerged in 2000 by Chen et al. [351] with Sr doped-$LaInO_3$ perovskite [352]. A conventional SLFC consists of a composite material composed of an electronic conductor or semiconductor and an ionic conductor. This core component supports both electrode reactions on the cell's opposing edges and enables ion transportation across the cell [353]. There are various material options for SLFC by compositing electronic/semiconductor wide band-gap oxides (e.g., $Li_xNi_yZn_{1-x-y}O$) and ionic conductors (e.g., samarium- or gadolinium-doped ceria and perovskite materials) [354]. SLFCs appear to be promising since they will not face chemical, mechanical, and thermal incompatibility issues as in conventional three-layer SOFCs [355]. However, not much research has been done on the long-term stability and durability of these SLFCs so far, and most of the stability studies are short-term [352,355–357]. In this regard, Deng et al. [358] investigated the electrochemical durability of double perovskite $Sr_2Fe_{1.5}Mo_{0.5}O_{6-\delta}$-SDC composite as an SLFC at 550 °C in a galvanostatic test mode under 156 mA cm^{-2} with H_2 as fuel. This material, which had an 841 mW cm^{-2} as maximum power density at 550 °C, presented a stable output voltage above 0.94 V during 24 h of the test [358]. In another study, Gao et al. [359] performed a galvanostatic durability test at 550 °C for around 70 h under 100 mA cm^{-2} current density to justify the promising performance of SDC-$La_{0.25}Sr_{0.75}Ti_1O_{3+\delta}$-$Ni_{0.8}Co_{0.15}Al_{0.05}LiO_{2-\delta}$ composite with 222 mW cm^{-2} power density at 550 °C. This SLFC was maintained in a stable cell voltage for 68 h during the operation as the single component structure prevented delamination caused by a mismatch in thermal expansion coefficients between electrodes and electrolyte [359].

6. Conclusions

Solid oxide fuel cells need to overcome the durability and stability challenges to meet a commercial breakthrough. However, degradation studies are absent as most state-of-the-art publications focus on achieving higher power densities. These efforts on improving the performance will not be practical without optimizing the lifespan of SOFCs through degradation research. This review focused on the degradation mechanisms of the electrodes and electrolyte, the latest progress in durability and stability improvements of SOFCs, how they excel in the degradation, and the different characterization techniques for studying the field. Overall, the electrodes (both anode and cathode) are more vulnerable to degradation as they are more exposed to a stimulating atmosphere which causes poisoning. The most serious poisonings in cathode and anode are Cr poisoning and coking, respectively. They also suffer from microstructural deformations along with chemical and thermal strains. For the electrolyte, the degradation mainly occurs as phase transition, dopant diffusion, and mechanical failure. The most recent reports in advancing the degradation behavior have shown several techniques for this purpose, including using dopants for perovskite and spinel-based electrodes, surface engineering via exsolution, using a coating and infiltration, microstructural optimization (e.g., core-shell structure), and interface modification (like applying a thin film between the electrolyte and cathode).

Furthermore, characterization plays a critical role in better understanding the degradation mechanisms giving new insight to overcome the durability issues. Here, the study tools were categorized into electrochemical, chemical, and structural characterization. The first one contains I–V measurement, EIS, and calendar life tests. The chemical and structural characterization groups include Raman spectroscopy, FT-IR, XRD, XPS, SIMS, TGA, DSC, dilatometry, and microscopy techniques. These techniques are conducted in situ, ex situ, or both modes, depending on the characterization type, to provide the information as detailed as possible. Modeling is also another cost-effective method to understand the SOFC performance better.

It is possible to achieve a better knowledge in degradation of SOFC via modern characterization techniques as there is a lack of in-depth knowledge of degradation mechanisms. Degradation processes in SOFCs are complicated and depend on many parameters simultaneously. For instance, the role of temperature is still undefined. There are several reports about enhancing the durability with increasing temperature, leading to uncertainty about the destructive act of high temperatures [360]. Besides, the short-term behavior cannot be interpolated into long-term behavior as the degradation process is non-linear [361–363]. Furthermore, the absence of proper *in-situ* characterization tools that can work during the electrochemical process of SOFC at high temperatures hinders deeper understanding of the degradation mechanisms. Another challenge is the limited choice of materials for SOFC components due to the severe working conditions. The difficulty is finding a material with the desired properties for the cathode/electrolyte/anode (mentioned before) whilst having good compatibility with the SOFC harsh working conditions and other components at the same time [364].

Regardless of these fundamental limitations, the lack of systematic standards to study the durability and stability of the SOFCs is strongly felt. For instance, there is no set of standards for long-term/short-term operation durations or no particular range for the applied study techniques in current density or voltage amplitude in the lab scale. It is necessary to set guidelines and criteria to compare the degradation results accurately.

This review will help overcoming the limitations identified by proposing new materials and using modern fabrication methods for SOFC components.

Declaration of competing interest

The authors declare that they have no known competing financial interests or personal relationships that could have appeared to influence the work reported in this paper.

Acknowledgment

The authors are thankful to Academy of Finland (Grant No. 13329016, 13322738) for the financial support. Dr. Asghar also thanks the Hubei Overseas Talent 100 program.

References

[1] Arshad MS, Raza R, Ahmad MA, Abbas G, Ali A, Rafique A, et al. An efficient Sm and Ge co-doped ceria nanocomposite electrolyte for low temperature solid oxide fuel cells. Ceram Int 2018;44:170–4.
[2] Abd Aziz AJ, Baharuddin NA, Somalu MR, Muchtar A. Review of composite cathodes for intermediate-temperature solid oxide fuel cell applications. Ceram Int 2020;46:23314–25. https://doi.org/10.1016/j.ceramint.2020.06.176.
[3] Zakaria Z, Abu Hassan SH, Shaari N, Yahaya AZ, Boon Kar Y. A review on recent status and challenges of yttria stabilized zirconia modification to lowering the temperature of solid oxide fuel cells operation. Int J Energy Res 2020;44:631–50.
[4] Fan L, Zhu B, Su P-C, He C. Nanomaterials and technologies for low temperature solid oxide fuel cells: recent advances, challenges and opportunities. Nano Energy 2018;45:148–76.
[5] Song Y, Chen Y, Wang W, Zhou C, Zhong Y, Yang G, et al. Self-assembled triple-conducting nanocomposite as a superior protonic ceramic fuel cell cathode. Joule 2019;3:2842–53.
[6] Kirubakaran A, Jain S, Nema RK. A review on fuel cell technologies and power electronic interface. Renew Sustain Energy Rev 2009;13:2430–40. https://doi.org/10.1016/j.rser.2009.04.004.
[7] Mahato N, Banerjee A, Gupta A, Omar S, Balani K. Progress in material selection for solid oxide fuel cell technology: a review. Prog Mater Sci 2015;72:141–337. https://doi.org/10.1016/j.pmatsci.2015.01.001.
[8] Stambouli AB, Traversa E. Solid oxide fuel cells (SOFCs): a review of an environmentally clean and efficient source of energy. Renew Sustain Energy Rev 2002;6:433–55. https://doi.org/10.1016/S1364-0321(02)00014-X.
[9] Abdalla AM, Hossain S, Azad AT, Petra PMI, Begum F, Eriksson SG, et al. Nanomaterials for solid oxide fuel cells: a review. Renew Sustain Energy Rev 2018;82:353–68.
[10] Chan SH. A review of anode materials development in solid oxide fuel cells. J Mater Sci 2004;39:4405–39.
[11] Gou Y, Li G, Ren R, Xu C, Qiao J, Sun W, et al. Pr-doping motivating the phase transformation of the BaFeO3-δ perovskite as a high-performance solid oxide fuel cell cathode. ACS Appl Mater Interfaces 2021.
[12] Jouttijärvi S, Asghar MI, Lund PD. Microscopic techniques for analysis of ceramic fuel cells, vol. 7. Wiley Interdiscip Rev Energy Environ; 2018. p. e299.
[13] Zakaria Z, Awang Mat Z, Abu Hassan SH, Boon Kar Y. A review of solid oxide fuel cell component fabrication methods toward lowering temperature. Int J Energy Res 2020;44:594–611. https://doi.org/10.1002/er.4907.
[14] Price R, Cassidy M, Grolig JG, Longo G, Weissen U, Mai A, et al. Upscaling of Co-impregnated La0. 20Sr0. 25Ca0. 45TiO3 anodes for solid oxide fuel cells: a progress report on a decade of academic-industrial collaboration. Adv Energy Mater 2021;11:2003951.
[15] Sun C, Hui R, Roller J. Cathode materials for solid oxide fuel cells: a review. J Solid State Electrochem 2010;14:1125–44.
[16] Fergus JW. Electrolytes for solid oxide fuel cells. J Power Sources 2006;162:30–40. https://doi.org/10.1016/j.jpowsour.2006.06.062.
[17] Kendall K, Kendall M. High-temperature solid oxide fuel cells for the 21st century: fundamentals, design and applications. Elsevier; 2015.

[18] Li G, Gou Y, Qiao J, Sun W, Wang Z, Sun K. Recent progress of tubular solid oxide fuel cell: from materials to applications. J Power Sources 2020;477:228693. https://doi.org/10.1016/j.jpowsour.2020.228693.

[19] Xu X, Bi L, Zhao XS. Highly-conductive proton-conducting electrolyte membranes with a low sintering temperature for solid oxide fuel cells. J Membr Sci 2018;558:17–25. https://doi.org/10.1016/j.memsci.2018.04.037.

[20] Hossain S, Abdalla AM, Jamain SNB, Zaini JH, Azad AK. A review on proton conducting electrolytes for clean energy and intermediate temperature-solid oxide fuel cells. Renew Sustain Energy Rev 2017;79:750–64. https://doi.org/10.1016/j.rser.2017.05.147.

[21] Yoo S, Jun A, Ju Y, Odkhuu D, Hyodo J, Jeong HY, et al. Development of double-perovskite compounds as cathode materials for low-temperature solid oxide fuel cells. Angew Chem 2014;126:13280–3.

[22] Zhang Y, Knibbe R, Sunarso J, Zhong Y, Zhou W, Shao Z, et al. Recent progress on advanced materials for solid-oxide fuel cells operating below 500 C. Adv Mater 2017;29:1700132.

[23] Zhang Z, Xie D, Ni J, Ni C. Ba2YCu3O6+δ-based cathode material for proton-conducting solid oxide fuel cells. Ceram Int 2021;47:14673–9. https://doi.org/10.1016/j.ceramint.2021.01.242.

[24] Duan C, Tong J, Shang M, Nikodemski S, Sanders M, Ricote S, et al. Readily processed protonic ceramic fuel cells with high performance at low temperatures. Science 2015;349:1321–6. 80-.

[25] Ren R, Wang Z, Xu C, Sun W, Qiao J, Rooney DW, et al. Tuning the defects of the triple conducting oxide BaCo 0.4 Fe 0.4 Zr 0.1 Y 0.1 O 3− δ perovskite toward enhanced cathode activity of protonic ceramic fuel cells. J Mater Chem 2019;7:18365–72.

[26] Xia Y, Xu X, Teng Y, Lv H, Jin Z, Wang D, et al. A novel BaFe0.8Zn0.1Bi0.1O3−δ cathode for proton conducting solid oxide fuel cells. Ceram Int 2020;46:25453–9. https://doi.org/10.1016/j.ceramint.2020.07.015.

[27] Li G, Gou Y, Ren R, Xu C, Qiao J, Sun W, et al. Fluorinated Pr2NiO4+δ as high-performance air electrode for tubular reversible protonic ceramic cells. J Power Sources 2021;508:230343. https://doi.org/10.1016/j.jpowsour.2021.230343.

[28] Wang D, Xia Y, Lv H, Miao L, Bi L, Liu W. PrBaCo2-xTaxO5+δ based composite materials as cathodes for proton-conducting solid oxide fuel cells with high CO2 resistance. Int J Hydrogen Energy 2020;45:31017–26. https://doi.org/10.1016/j.ijhydene.2020.08.094.

[29] Tu B, Yin Y, Zhang F, Su X, Lyu X, Cheng M. High performance of direct methane-fuelled solid oxide fuel cell with samarium modified nickel-based anode. Int J Hydrogen Energy 2020;45:27587–96. https://doi.org/10.1016/j.ijhydene.2020.07.070.

[30] Sciazko A, Komatsu Y, Shimura T, Shikazono N. Multiscale microstructural evolutions of nickel-gadolinium doped ceria in solid oxide fuel cell anode. J Power Sources 2020;478:228710. https://doi.org/10.1016/j.jpowsour.2020.228710.

[31] Rahumi O, Sobolev A, Rath MK, Borodianskiy K. Nanostructured engineering of nickel cermet anode for solid oxide fuel cell using inkjet printing. J Eur Ceram Soc 2021;41:4528–36. https://doi.org/10.1016/j.jeurceramsoc.2021.03.017.

[32] Xi X, Liu J, Fan Y, Wang L, Li J, Li M, et al. Reducing d-p band coupling to enhance CO2 electrocatalytic activity by Mg-doping in Sr2FeMoO6-δ double perovskite for high performance solid oxide electrolysis cells. Nano Energy 2021;82:105707. https://doi.org/10.1016/j.nanoen.2020.105707.

[33] Cai W, Zhou M, Cao D, Yan X, Li Q, Lü S, et al. Ni-doped A-site-deficient La0.7Sr0.3Cr0.5Mn0.5O3-δ perovskite as anode of direct carbon solid oxide fuel cells. Int J Hydrogen Energy 2020;45:21873–80. https://doi.org/10.1016/j.ijhydene.2020.05.266.

[34] Yokokawa H. Towards comprehensive description of stack durability/reliability behavior. Fuel Cell 2015;15:652–68.

[35] McPhail SJ. The yellow pages of SOFC technology. International Status of SOFC deployment 2017; 2017.

[36] Whiston MM, Azevedo IML, Litster S, Samaras C, Whitefoot KS, Whitacre JF. Meeting US solid oxide fuel cell targets. Joule 2019;3:2060–5.

[37] Skafte TL, Hjelm J, Blennow P, Graves CR. Quantitative review of degradation and lifetime of solid oxide cells and stacks. In: 12th Eur. SOFC SOE Forum, European Fuel Cell Forum; 2016. p. 8–27.

[38] Blum L, Fang Q, Groß-Barsnick SM, , de Haart LGJ (Bert), Malzbender J, Menzler NH, et al. Long-term operation of solid oxide fuel cells and preliminary findings on accelerated testing. Int J Hydrogen Energy 2020;45:8955–64. https://doi.org/10.1016/j.ijhydene.2020.01.074.

[39] Menzler NH, Sebold D, Sohn YJ, Zischke S. Post-test characterization of a solid oxide fuel cell after more than 10 years of stack testing. J Power Sources 2020;478:228770. https://doi.org/10.1016/j.jpowsour.2020.228770.

[40] Blum L, De Haart LGJ, Malzbender J, Margaritis N, Menzler NH. Anode-supported solid oxide fuel cell achieves 70 000 hours of continuous operation. Energy Technol 2016;4:939–42.

[41] Zhang Y-C, Jiang W, Tu S-T, Wang C-L, Chen C. Effect of operating temperature on creep and damage in the bonded compliant seal of planar solid oxide fuel cell. Int J Hydrogen Energy 2018;43:4492–504. https://doi.org/10.1016/j.ijhydene.2018.01.048.

[42] De Haart LGJB, Beale SB, Deja R, Dittrich L, Duyster T, Fang Q, et al. Forschungszentrum jülich–current activities in SOC development. ECS Trans 2021;103:299.

[43] Fang Q, de Haart U, Schäfer D, Thaler F, Rangel-Hernandez V, Peters R, et al. Degradation analysis of an SOFC short stack subject to 10,000 h of operation. J Electrochem Soc 2020;167:144508.

[44] Mai A, Iwanschitz B, Schuler JA, Denzler R, Nerlich V, Schuler A. Hexis' SOFC system galileo 1000 N–lab and field test experiences. ECS Trans 2013;57:73.

[45] Chou Y-S, Stevenson JW, Choi J-P. Long-term evaluation of solid oxide fuel cell candidate materials in a 3-cell generic short stack fixture, part I: test fixture, sealing, and electrochemical performance. J Power Sources 2014;255:1–8. https://doi.org/10.1016/j.jpowsour.2013.12.067.

[46] Ido A, Asano K, Morita H, Yamamoto T, Mugikura Y. Degradation analysis of SOFC performance (1)—severe operation with high fuel utilization. ECS Trans 2019;91:801.

[47] Thaheem I, Joh DW, Noh T, Lee KT. Highly conductive and stable Mn1.35Co1.35Cu0.2Y0.1O4 spinel protective coating on commercial ferritic stainless steels for intermediate-temperature solid oxide fuel cell interconnect applications. Int J Hydrogen Energy 2019;44:4293–303. https://doi.org/10.1016/j.ijhydene.2018.12.173.

[48] Jamil SM, Othman MHD, Rahman MA, Jaafar J, Ismail AF, Li K. Recent fabrication techniques for micro-tubular solid oxide fuel cell support: a review. J Eur Ceram Soc 2015;35:1–22.

[49] Patcharavorachot Y, Arpornwichanop A, Chuachuensuk A. Electrochemical study of a planar solid oxide fuel cell: role of support structures. J Power Sources 2008;177:254–61.

[50] Kluczowski R, Kawalec M, Krauz M, Świeca A. Types, fabrication, and characterization of solid oxide fuel cells. In: Model. Des. Constr. Oper. Power gener. With solid oxide fuel cells. Springer; 2018. p. 21–47.

[51] Hsieh YD, Chan YH, Shy SS. Effects of pressurization and temperature on power generating characteristics and impedances of anode-supported and electrolyte-supported planar solid oxide fuel cells. J Power Sources 2015;299:1–10.

[52] Fang X, Zhu J, Lin Z. Effects of electrode composition and thickness on the mechanical performance of a solid oxide fuel cell. Energies 2018;11:1735.

[53] Hodjati-Pugh O, Dhir A, Steinberger-Wilckens R. The development of current collection in micro-tubular solid oxide fuel cells—a review. Appl Sci 2021;11:1077.

[54] Huang K, Singhal SC. Cathode-supported tubular solid oxide fuel cell technology: a critical review. J Power Sources 2013;237:84–97.

[55] Droushiotis N, Grande FD, Dzarfan Othman MH, Kanawka K, Doraswami U, Metcalfe IS, et al. Comparison between anode-supported and electrolyte-supported Ni-CGO-LSCF micro-tubular solid oxide fuel cells. Fuel Cell 2014;14:200–11.

[56] Buccheri MA, Singh A, Hill JM. Anode-versus electrolyte-supported Ni-YSZ/YSZ/Pt SOFCs: effect of cell design on OCV, performance and carbon formation for the direct utilization of dry methane. J Power Sources 2011;196:968–76.

[57] Grayson K. Novel sealants to significantly improve the lifetime and performance of solid oxide fuel cells Mo-sci corporation. https://mo-sci.com/novel-sealants-improve-solid-oxide-fuel-cells/. [Accessed 3 September 2021].

[58] Park B-K, Lee J-W, Lee S-B, Lim T-H, Park S-J, Song R-H, et al. A flat-tubular solid oxide fuel cell with a dense interconnect film coated on the porous anode support. J Power Sources 2012;213:218–22. https://doi.org/10.1016/j.jpowsour.2012.04.025.

[59] Khan MZ, Iltaf A, Ishfaq HA, Khan FN, Tanveer WH, Song R-H, et al. Flat-tubular solid oxide fuel cells and stacks: a review. J Asian Ceram Soc 2021:1–26.

[60] Behling NH. Chapter 6 - history of solid oxide fuel cells. In: Behling NHBT-FC. Elsevier; 2013. p. 223–421. https://doi.org/10.1016/B978-0-444-56325-5.00006-5.

[61] Park S, Sammes NM, Song K-H, Kim T, Chung J-S. Monolithic flat tubular types of solid oxide fuel cells with integrated electrode and gas channels. Int J Hydrogen Energy 2017;42:1154–60. https://doi.org/10.1016/j.ijhydene.2016.08.212.

[62] Riegraf M. Investigation of sulfur poisoning of Ni-based anodes in solid oxide fuel cells. 2019.

[63] Slodczyk A, Torrell M, Hornés A, Morata A, Kendall K, Tarancón A. Understanding longitudinal degradation mechanisms of large-area micro-tubular solid oxide fuel cells. Electrochim Acta 2018;265:232–43.

[64] Batfalsky P, Malzbender J, Menzler NH. Post-operational characterization of solid oxide fuel cell stacks. Int J Hydrogen Energy 2016;41:11399–411.

[65] Cao X, Yang Y, Yan X, Geels NJ, Luo J-L, Yan N. Revitalizing" degraded solid oxide fuel cells in sour fuels for bifunctional oxygen catalysis in zinc–air batteries. Green Chem 2020;22:6075–83.

[66] Yokokawa H, Tu H, Iwanschitz B, Mai A. Fundamental mechanisms limiting solid oxide fuel cell durability. J Power Sources 2008;182:400–12. https://doi.org/10.1016/j.jpowsour.2008.02.016.

[67] Niu Y, Lv W, Chen D, Han J, He W. A model study on correlation between microstructure-gas diffusion and Cr deposition in porous LSM/YSZ cathodes of solid oxide fuel cells. Int J Hydrogen Energy 2019;44:18319–29. https://doi.org/10.1016/j.ijhydene.2019.05.115.

[68] Yokokawa H, Suzuki M, Yoda M, Suto T, Tomida K, Hiwatashi K, et al. Achievements of NEDO durability projects on SOFC stacks in the light of physicochemical mechanisms. Fuel Cell 2019;19:311–39. https://doi.org/10.1002/fuce.201800187.

[69] Wang F, Kishimoto H, Ishiyama T, Develos-Bagarinao K, Yamaji K, Horita T, et al. A review of sulfur poisoning of solid oxide fuel cell cathode materials for solid oxide fuel cells. J Power Sources 2020;478:228763.

[70] Wang F, Kishimoto H, Develos-Bagarinao K, Yamaji K, Horita T, Yokokawa H. Interrelation between sulfur poisoning and performance degradation of LSCF cathode for SOFCs. J Electrochem Soc 2016;163:F899.

[71] Wang CC, He S, Chen K, Rowles MR, Darvish S, Zhong Y. Effect of SO2 poisoning on the electrochemical activity of La0. 6Sr0. 4Co0. 2Fe0. 8O3-δ cathodes of solid oxide fuel cells. J Electrochem Soc 2017;164:F514.

[72] Budiman RA, Liu SS, Bagarinao KD, Ishiyama T, Kishimoto H, Yamaji K, et al. Determination of factors governing surface composition and degradation of La0.

6Sr0. 4Co0. 2Fe0. 8O3-δ electrode under sulfur-contained air. J Electrochem Soc 2019;166:F414.

[73] Xu C, Sun K, Yang X, Ma M, Ren R, Qiao J, et al. Highly active and CO2-tolerant Sr2Fe1. 3Ga0. 2Mo0. 5O6-δ cathode for intermediate-temperature solid oxide fuel cells. J Power Sources 2020;450:227722.

[74] He S, Saunders M, Chen K, Gao H, Suvorova A, Rickard WDA, et al. A FIB-STEM study of strontium segregation and interface formation of directly assembled La0. 6Sr0. 4Co0. 2Fe0. 8O3-δ cathode on Y2O3-ZrO2 electrolyte of solid oxide fuel cells. J Electrochem Soc 2018;165:F417.

[75] Karimaghaloo A, Koo J, Kang H-S, Song SA, Shim JH, Lee MH. Nanoscale surface and interface engineering of solid oxide fuel cells by atomic layer deposition. Int J Precis Eng Manuf Technol 2019;1–18.

[76] Koo B, Kim K, Kim JK, Kwon H, Han JW, Jung W. Sr segregation in perovskite oxides: why it happens and how it exists. Joule 2018;2:1476–99.

[77] Anjum U, Agarwal M, Khan TS, Gupta RK, Haider MA. Controlling surface cation segregation in a nanostructured double perovskite GdBaCo 2 O 5+ δ electrode for solid oxide fuel cells. Nanoscale 2019;11:21404–18.

[78] Chen Y, Yoo S, Li X, Ding D, Pei K, Chen D, et al. An effective strategy to enhancing tolerance to contaminants poisoning of solid oxide fuel cell cathodes. Nano Energy 2018;47:474–80. https://doi.org/10.1016/j.nanoen.2018.03.043.

[79] Shah M, Voorhees PW, Barnett SA. Time-dependent performance changes in LSCF-infiltrated SOFC cathodes: the role of nano-particle coarsening. Solid State Ionics 2011;187:64–7. https://doi.org/10.1016/j.ssi.2011.02.003.

[80] Park K, Yu S, Bae J, Kim H, Ko Y. Fast performance degradation of SOFC caused by cathode delamination in long-term testing. Int J Hydrogen Energy 2010;35:8670–7. https://doi.org/10.1016/j.ijhydene.2010.05.005.

[81] Sreedhar I, Agarwal B, Goyal P, Agarwal A. An overview of degradation in solid oxide fuel cells-potential clean power sources. J Solid State Electrochem 2020.

[82] Yoshikawa M, Yamamoto T, Yasumoto K, Mugikura Y. Degradation analysis of SOFC stack performance: investigation of cathode sulfur poisoning due to contamination in air. ECS Trans 2017;78:2347.

[83] Gao K, Liu X, Wang Z, Liang C, Xiong Y. An effective approach to protect the Sm0.5Sr0.5Co3−δ (SSC) cathode from SO2 in SOFCs. RSC Adv 2016;6:42447–51. https://doi.org/10.1039/C6RA05309B.

[84] Wang CC, Luo D, Jiang SP, Lin B. Highly sulfur poisoning-tolerant BaCeO3-impregnated La0.6Sr0.4Co0.2Fe0.8O3-δ cathodes for solid oxide fuel cells. J Phys D Appl Phys 2018;51. https://doi.org/10.1088/1361-6463/aadf4c.

[85] Wang CC, Luo D, Hou B. Effect of BaO impregnation on sulfur tolerance of La0. 6Sr0. 4Co0. 2Fe0. 8O3− δ cathodes of solid oxide fuel cells. Mater Res Express 2019;6:75504.

[86] Devanathan R, Weber WJ, Singhal SC, Gale JD. Computer simulation of defects and oxygen transport in yttria-stabilized zirconia. Solid State Ionics 2006;177:1251–8. https://doi.org/10.1016/j.ssi.2006.06.030.

[87] Butz B, Kruse P, Störmer H, Gerthsen D, Müller A, Weber A, et al. Correlation between microstructure and degradation in conductivity for cubic Y2O3-doped ZrO2. Solid State Ionics 2006;177:3275–84. https://doi.org/10.1016/j.ssi.2006.09.003.

[88] Hattori M, Takeda Y, Sakaki Y, Nakanishi A, Ohara S, Mukai K, et al. Effect of aging on conductivity of yttria stabilized zirconia. J Power Sources 2004;126:23–7. https://doi.org/10.1016/j.jpowsour.2003.08.018.

[89] Zakaria Z, Kamarudin SK. Advanced modification of scandia-stabilized zirconia electrolytes for solid oxide fuel cells application—a review. Int J Energy Res 2020.

[90] Gao P, Bolon A, Taneja M, Xie Z, Orlovskaya N, Radovic M. Thermal expansion and elastic moduli of electrolyte materials for high and intermediate temperature solid oxide fuel cell. Solid State Ionics 2017;300:1–9. https://doi.org/10.1016/j.ssi.2016.11.015.

[91] Sun Y, He S, Saunders M, Chen K, Shao Z, Jiang SP. A comparative study of surface segregation and interface of La0·6Sr0·4Co0·2Fe0·8O3-δ electrode on GDC and YSZ electrolytes of solid oxide fuel cells. Int J Hydrogen Energy 2021;46:2606–16. https://doi.org/10.1016/j.ijhydene.2020.10.113.

[92] Brandon N. Solid oxide fuel cell lifetime and reliability: critical challenges in fuel cells. Academic Press; 2017.

[93] Jang I, Kim S, Kim C, Lee H, Yoon H, Song T, et al. Interface engineering of yttrium stabilized zirconia/gadolinium doped ceria bi-layer electrolyte solid oxide fuel cell for boosting electrochemical performance. J Power Sources 2019;435:226776. https://doi.org/10.1016/j.jpowsour.2019.226776.

[94] Kim Y-D, Yang J, Lee J-I, Saqib M, Shin J-S, Park K, et al. Degradation studies of ceria-based solid oxide fuel cells at intermediate temperature under various load conditions. J Power Sources 2020;452:227758. https://doi.org/10.1016/j.jpowsour.2020.227758.

[95] Jacobson AJ. Materials for solid oxide fuel cells. Chem Mater 2010;22:660–74.

[96] Liu L, Kim G-Y, Chandra A. Modeling of thermal stresses and lifetime prediction of planar solid oxide fuel cell under thermal cycling conditions. J Power Sources 2010;195:2310–8. https://doi.org/10.1016/j.jpowsour.2009.10.064.

[97] Selcuk A, Merere G, Atkinson A. The influence of electrodes on the strength of planar zirconia solid oxide fuel cells. J Mater Sci 2001;36:1173–82.

[98] Parhizkar T, Roshandel R. Long term performance degradation analysis and optimization of anode supported solid oxide fuel cell stacks. Energy Convers Manag 2017;133:20–30. https://doi.org/10.1016/j.enconman.2016.11.045.

[99] Wang F, Lyu Y, Chu D, Jin Z, Zhang G, Wang D. The electrolyte materials for SOFCs of low-intermediate temperature. Mater Sci Technol 2019;35:1551–62.

[100] Bishop SR. Chemical expansion of solid oxide fuel cell materials: a brief overview. Acta Mech Sin 2013;29:312–7.

[101] Zekri A, Herbrig K, Knipper M, Parisi J, Plaggenborg T. Nickel depletion and agglomeration in SOFC anodes during long-term operation. Fuel Cell 2017;17:359–66. https://doi.org/10.1002/fuce.201600220.

[102] Khan MZ, Mehran MT, Song R-H, Lee J-W, Lee S-B, Lim T-H. A simplified approach to predict performance degradation of a solid oxide fuel cell anode. J Power Sources 2018;391:94–105. https://doi.org/10.1016/j.jpowsour.2018.04.080.

[103] Jiao Z, Takagi N, Shikazono N, Kasagi N. Study on local morphological changes of nickel in solid oxide fuel cell anode using porous Ni pellet electrode. J Power Sources 2011;196:1019–29. https://doi.org/10.1016/j.jpowsour.2010.08.047.

[104] Xiang Y, Da Y, Shikazono N, Jiao Z. Quantitative study on solid oxide fuel cell anode microstructure stability based on 3D microstructure reconstructions. J Power Sources 2020;477:228653. https://doi.org/10.1016/j.jpowsour.2020.228653.

[105] Holzer L, Münch B, Iwanschitz B, Cantoni M, Hocker T, Graule T. Quantitative relationships between composition, particle size, triple phase boundary length and surface area in nickel-cermet anodes for Solid Oxide Fuel Cells. J Power Sources 2011;196:7076–89. https://doi.org/10.1016/j.jpowsour.2010.08.006.

[106] Jiao Z, Shikazono N, Kasagi N. Study on degradation of solid oxide fuel cell anode by using pure nickel electrode. J Power Sources 2011;196:8366–76. https://doi.org/10.1016/j.jpowsour.2011.06.069.

[107] Xu C, Zondlo JW, Finklea HO, Demircan O, Gong M, Liu X. The effect of phosphine in syngas on Ni–YSZ anode-supported solid oxide fuel cells. J Power Sources 2009;193:739–46.

[108] Subotić V, Schluckner C, Hochenauer C. An experimental and numerical study of performance of large planar ESC-SOFCs and experimental investigation of carbon depositions. J Energy Inst 2016;89:121–37. https://doi.org/10.1016/j.joei.2015.01.004.

[109] Subotić V, Schluckner C, Schroettner H, Hochenauer C. Analysis of possibilities for carbon removal from porous anode of solid oxide fuel cells after different failure modes. J Power Sources 2016;302:378–86. https://doi.org/10.1016/j.jpowsour.2015.10.071.

[110] Timmermann H, Sawady W, Campbell D, Weber A, Reimert R, Ivers-Tiffee E. Coke formation and degradation in SOFC operation with a model reformate from liquid hydrocarbons. J Electrochem Soc 2008;155:B356.

[111] Gür TM. Critical review of carbon conversion in "carbon fuel cells. Chem Rev 2013;113:6179–206.

[112] Kim T, Liu G, Boaro M, Lee S-I, Vohs JM, Gorte RJ, et al. A study of carbon formation and prevention in hydrocarbon-fueled SOFC. J Power Sources 2006;155:231–8. https://doi.org/10.1016/j.jpowsour.2005.05.001.

[113] Kan H, Lee H. Sn-doped Ni/YSZ anode catalysts with enhanced carbon deposition resistance for an intermediate temperature SOFC. Appl Catal B Environ 2010;97:108–14. https://doi.org/10.1016/j.apcatb.2010.03.029.

[114] Marina OA, Coyle CA, Thomsen EC, Edwards DJ, Coffey GW, Pederson LR. Degradation mechanisms of SOFC anodes in coal gas containing phosphorus. Solid State Ionics 2010;181:430–40. https://doi.org/10.1016/j.ssi.2010.01.018.

[115] Liu W, Sun X, Pederson LR, Marina OA, Khaleel MA. Effect of nickel–phosphorus interactions on structural integrity of anode-supported solid oxide fuel cells. J Power Sources 2010;195:7140–5. https://doi.org/10.1016/j.jpowsour.2010.06.015.

[116] Coyle CA, Marina OA, Thomsen EC, Edwards DJ, Cramer CD, Coffey GW, et al. Interactions of nickel/zirconia solid oxide fuel cell anodes with coal gas containing arsenic. J Power Sources 2009;193:730–8. https://doi.org/10.1016/j.jpowsour.2009.04.042.

[117] Marina OA, Pederson LR, Coyle CA, Thomsen EC, Edwards DJ. Polarization-induced interfacial reactions between nickel and selenium in Ni/zirconia SOFC anodes and comparison with sulfur poisoning. J Electrochem Soc 2010;158:B36.

[118] Sasaki K, Haga K, Yoshizumi T, Minematsu D, Yuki E, Liu R, et al. Chemical durability of solid oxide fuel cells: influence of impurities on long-term performance. J Power Sources 2011;196:9130–40. https://doi.org/10.1016/j.jpowsour.2010.09.122.

[119] Ryan EM, Xu W, Sun X, Khaleel MA. A damage model for degradation in the electrodes of solid oxide fuel cells: modeling the effects of sulfur and antimony in the anode. J Power Sources 2012;210:233–42. https://doi.org/10.1016/j.jpowsour.2012.02.091.

[120] Trembly JP, Marquez AI, Ohrn TR, Bayless DJ. Effects of coal syngas and H2S on the performance of solid oxide fuel cells: single-cell tests. J Power Sources 2006;158:263–73. https://doi.org/10.1016/j.jpowsour.2005.09.055.

[121] Kupecki J, Papurello D, Lanzini A, Naumovich Y, Motylinski K, Blesznowski M, et al. Numerical model of planar anode supported solid oxide fuel cell fed with fuel containing H2S operated in direct internal reforming mode (DIR-SOFC). Appl Energy 2018;230:1573–84. https://doi.org/10.1016/j.apenergy.2018.09.092.

[122] Li J, Wei B, Yue X, Su C, Lü Z. Investigations on sulfur poisoning mechanisms of a solid oxide fuel cell with niobium-doped ferrate perovskite anode. Electrochim Acta 2020;335:135703. https://doi.org/10.1016/j.electacta.2020.135703.

[123] Zhi M, Chen X, Finklea H, Celik I, Wu NQ. Electrochemical and microstructural analysis of nickel–yttria-stabilized zirconia electrode operated in phosphorus-containing syngas. J Power Sources 2008;183:485–90. https://doi.org/10.1016/j.jpowsour.2008.05.055.

[124] Cheng Z, Wang J-H, Choi Y, Yang L, Lin M-C, Liu M. From Ni-YSZ to sulfur-tolerant anode materials for SOFCs: electrochemical behavior, in situ characterization, modeling, and future perspectives. Energy Environ Sci 2011;4:4380–409.

[125] Marina OA, Pederson L, Gemmen R, Gerdes K, Finklea H, Celik I. Overview of SOFC anode interactions with coal gas impurities. ECS Trans 2019;26:363–70. https://doi.org/10.1149/1.3429009.

[126] Marina OA, Pederson LR, Coyle CA, Thomsen EC, Coffey GW. Ni/YSZ anode interactions with impurities in coal gas. ECS Trans 2009;25:2125.

[127] Madi H, Lanzini A, Papurello D, Diethelm S, Ludwig C, Santarelli M, et al. Solid oxide fuel cell anode degradation by the effect of hydrogen chloride in stack and single cell environments. J Power Sources 2016;326:349–56. https://doi.org/10.1016/j.jpowsour.2016.07.003.

[128] Haga K, Shiratori Y, Ito K, Sasaki K. Chlorine poisoning of SOFC Ni-cermet anodes. J Electrochem Soc 2008;155:B1233.

[129] Marina OA, Pederson LR, Coyle CA, Thomsen EC, Nachimuthu P, Edwards DJ. Electrochemical, structural and surface characterization of nickel/zirconia solid oxide fuel cell anodes in coal gas containing antimony. J Power Sources 2011;196:4911–22. https://doi.org/10.1016/j.jpowsour.2011.02.027.

[130] Heenan TMM, Lu X, Iacoviello F, Robinson JB, Brett DJL, Shearing PR. Thermally driven SOFC degradation in 4D: Part I. Microscale. J Electrochem Soc 2018;165:F921.

[131] Lu X, Heenan TMM, Bailey JJ, Li T, Li K, Brett DJL, et al. Correlation between triple phase boundary and the microstructure of Solid Oxide Fuel Cell anodes: the role of composition, porosity and Ni densification. J Power Sources 2017;365:210–9.

[132] Karczewski J, Dunst KJ, Jasinski P, Molin S. High temperature corrosion and corrosion protection of porous Ni22Cr alloys. Surf Coating Technol 2015;261:385–90. https://doi.org/10.1016/j.surfcoat.2014.10.051.

[133] Hassan MA, Mamat O Bin, Mehdi M. Review: influence of alloy addition and spinel coatings on Cr-based metallic interconnects of solid oxide fuel cells. Int J Hydrogen Energy 2020;45:25191–209. https://doi.org/10.1016/j.ijhydene.2020.06.234.

[134] Talic B, Falk-Windisch H, Venkatachalam V, Hendriksen PV, Wiik K, Lein HL. Effect of coating density on oxidation resistance and Cr vaporization from solid oxide fuel cell interconnects. J Power Sources 2017;354:57–67. https://doi.org/10.1016/j.jpowsour.2017.04.023.

[135] Masi A, Frangini S, Pumiglia D, Della Seta L, Masci A, McPhail SJ, et al. LaFeO3 perovskite conversion coatings grown on a 13Cr ferritic stainless steel: a corrosion degradation study in simulated solid oxide fuel cell (SOFC) interconnect conditions at 700° C. Mater Corros 2017;68:536–45.

[136] Yang Z, Walker MS, Singh P, Stevenson JW, Norby T. Oxidation behavior of ferritic stainless steels under SOFC interconnect exposure conditions. J Electrochem Soc 2004;151:B669.

[137] Niewolak L, Blum L, Peters R, Grüner D, Quadakkers WJ. Behavior of metallic components during 4,000 h operation of an SOFC stack with carbon containing fuel gas. Fuel Cell 2016;16:600–10.

[138] Sreedhar I, Agarwal B, Goyal P, Singh SA. Recent advances in material and performance aspects of solid oxide fuel cells. J Electroanal Chem 2019;848:113315.

[139] Bianco M, Caliandro P, Diethelm S, Yang S, Dellai A, Van herle J, et al. In-situ experimental benchmarking of solid oxide fuel cell metal interconnect solutions. J Power Sources 2020;461:228163. https://doi.org/10.1016/j.jpowsour.2020.228163.

[140] Kim BK, Kim D-I, Yi K-W. Suppression of Cr evaporation by Co electroplating and underlying Cr retention mechanisms for the 22wt.% Cr containing ferritic stainless steel. Corrosion Sci 2018;130:45–55. https://doi.org/10.1016/j.corsci.2017.10.019.

[141] Yang Z, Xia G-G, Stevenson JW. Evaluation of Ni–Cr-base alloys for SOFC interconnect applications. J Power Sources 2006;160:1104–10. https://doi.org/10.1016/j.jpowsour.2006.02.099.

[142] Garcia-Fresnillo L, Niewolak L, Quadakkers WJ, Meier GH. Influence of alloying elements on the behavior of different ferritic steels as candidate materials for SOFC interconnect. Oxid Met 2018;89:61–80.

[143] Zhang W, Hua B, Yang J, Chi B, Pu J, Jian L. Performance evaluation of a new Fe-Cr-Mn alloy in the reducing atmosphere of solid oxide fuel cells. J Alloys Compd 2018;769:866–72. https://doi.org/10.1016/j.jallcom.2018.08.002.

[144] Stanislowski M, Froitzheim J, Niewolak L, Quadakkers WJ, Hilpert K, Markus T, et al. Reduction of chromium vaporization from SOFC interconnectors by highly effective coatings. J Power Sources 2007;164:578–89.

[145] Fontana S, Amendola R, Chevalier S, Piccardo P, Caboche G, Viviani M, et al. Metallic interconnects for SOFC: characterisation of corrosion resistance and conductivity evaluation at operating temperature of differently coated alloys. J Power Sources 2007;171:652–62. https://doi.org/10.1016/j.jpowsour.2007.06.255.

[146] Palcut M, Mikkelsen L, Neufeld K, Chen M, Knibbe R, Hendriksen PV. Efficient dual layer interconnect coating for high temperature electrochemical devices. Int J Hydrogen Energy 2012;37:14501–10. https://doi.org/10.1016/j.ijhydene.2012.07.038.

[147] Lenka RK, Patro PK, Sharma J, Mahata T, Sinha PK. Evaluation of La0.75Sr0.25Cr0.5Mn0.5O3 protective coating on ferritic stainless steel interconnect for SOFC application. Int J Hydrogen Energy 2016;41:20365–72. https://doi.org/10.1016/j.ijhydene.2016.08.143.

[148] Chandra-ambhorn S, Homjabok W, Chandra-ambhorn W, Thublaor T, Siripongsakul T. Oxidation and volatilisation behaviour of a type 430 stainless steel coated by Mn-Co oxide by slurry method with pre-oxidation for SOFC interconnect application. Corrosion Sci 2021;187:109506. https://doi.org/10.1016/j.corsci.2021.109506.

[149] Aznam I, Mah JCW, Muchtar A, Somalu MR, Ghazali MJ. Electrophoretic deposition of (Cu,Mn,Co)3O4 spinel coating on SUS430 ferritic stainless steel: process and performance evaluation for solid oxide fuel cell interconnect applications. J Eur Ceram Soc 2021;41:1360–73. https://doi.org/10.1016/j.jeurceramsoc.2020.09.074.

[150] Brylewski T, Molin S, Marczyński M, Mazur Ł, Domaradzki K, Kryshtal O, et al. Influence of Gd deposition on the oxidation behavior and electrical properties of a layered system consisting of Crofer 22 APU and MnCo2O4 spinel. Int J Hydrogen Energy 2021;46:6775–91. https://doi.org/10.1016/j.ijhydene.2020.11.169.

[151] Molin S, Sabato AG, Bindi M, Leone P, Cempura G, Salvo M, et al. Microstructural and electrical characterization of Mn-Co spinel protective coatings for solid oxide cell interconnects. J Eur Ceram Soc 2017;37:4781–91. https://doi.org/10.1016/j.jeurceramsoc.2017.07.011.

[152] Thomann O, Pihlatie M, Rautanen M, Himanen O, Lagerbom J, Mäkinen M, et al. Development and application of HVOF sprayed spinel protective coating for SOFC interconnects. J Therm Spray Technol 2013;22:631–9.

[153] Zhao Q, Geng S, Chen G, Wang F. Effect of NiFe2 coating thickness on high temperature oxidation and electrical behavior of coated steel interconnect. J Alloys Compd 2021;858:157746. https://doi.org/10.1016/j.jallcom.2020.157746.

[154] Zhao Q, Geng S, Gao X, Chen G, Wang F. Ni/NiFe2 dual-layer coating for SOFC steel interconnects application. J Power Sources Adv 2020;2:100011. https://doi.org/10.1016/j.powera.2020.100011.

[155] Zhao Q, Geng S, Chen G, Wang F. Application of sputtered NiFe2 alloy coating for SOFC interconnect steel. J Alloys Compd 2018;769:120–9. https://doi.org/10.1016/j.jallcom.2018.07.333.

[156] Pan Y, Geng S, Chen G, Wang F. CuFe2O4/CuO coating for solid oxide fuel cell steel interconnects. Int J Hydrogen Energy 2021;46:22942–55. https://doi.org/10.1016/j.ijhydene.2021.04.117.

[157] Joshi S, Petric A. Nickel substituted CuMn2O4 spinel coatings for solid oxide fuel cell interconnects. Int J Hydrogen Energy 2017;42:5584–9. https://doi.org/10.1016/j.ijhydene.2016.08.075.

[158] Mah JCW, Muchtar A, Somalu MR, Ghazali MJ. Metallic interconnects for solid oxide fuel cell: a review on protective coating and deposition techniques. Int J Hydrogen Energy 2017;42:9219–29. https://doi.org/10.1016/j.ijhydene.2016.03.195.

[159] Zanchi E, Sabato AG, Molin S, Cempura G, Boccaccini AR, Smeacetto F. Recent advances on spinel-based protective coatings for solid oxide cell metallic interconnects produced by electrophoretic deposition. Mater Lett 2021;286:129229. https://doi.org/10.1016/j.matlet.2020.129229.

[160] Krainova DA, Saetova NS, Farlenkov AS, Khodimchuk AV, Polyakova IG, Kuzmin AV. Long-term stability of SOFC glass sealant under oxidising and reducing atmospheres. Ceram Int 2021;47:8973–9. https://doi.org/10.1016/j.ceramint.2020.12.019.

[161] Rautanen M, Thomann O, Himanen O, Tallgren J, Kiviaho J. Glass coated compressible solid oxide fuel cell seals. J Power Sources 2014;247:243–8. https://doi.org/10.1016/j.jpowsour.2013.08.085.

[162] Rautanen M, Himanen O, Saarinen V, Kiviaho J. Compression properties and leakage tests of mica-based seals for SOFC stacks. Fuel Cell 2009;9:753–9.

[163] Fergus JW. Sealants for solid oxide fuel cells. J Power Sources 2005;147:46–57. https://doi.org/10.1016/j.jpowsour.2005.05.002.

[164] Halinen M, Pennanen J. Analysis of leakages in a solid oxide fuel cell stack in a system environment. Fuel Cell 2015;15:434–44.

[165] Krainova DA, Saetova NS, Kuzmin AV, Raskovalov AA, Eremin VA, Ananyev MV, et al. Non-crystallising glass sealants for SOFC: effect of Y2O3 addition. Ceram Int 2020;46:5193–200. https://doi.org/10.1016/j.ceramint.2019.10.266.

[166] Chou Y-S, Stevenson JW, Chick LA. Ultra-low leak rate of hybrid compressive mica seals for solid oxide fuel cells. J Power Sources 2002;112:130–6. https://doi.org/10.1016/S0378-7753(02)00356-7.

[167] Chou Y-S, Stevenson JW. Novel infiltrated Phlogopite mica compressive seals for solid oxide fuel cells. J Power Sources 2004;135:72–8. https://doi.org/10.1016/j.jpowsour.2004.02.037.

[168] Schrödl N, Bucher E, Egger A, Kreiml P, Teichert C, Höschen T, et al. Long-term stability of the IT-SOFC cathode materials La0.6Sr0.4CoO3−δ and La2NiO4+δ against combined chromium and silicon poisoning. Solid State Ionics 2015;276:62–71. https://doi.org/10.1016/j.ssi.2015.03.035.

[169] Kiebach R, Agersted K, Zielke P, Ritucci I, Brock MB, Hendriksen PV. A novel SOFC/SOEC sealing glass with a low SiO2 content and a high thermal expansion coefficient. ECS Trans 2017;78:1739.

[170] Garai M, Karmakar B. Zr+4-controlled nucleation and microstructure in Si-Mg-Al-K-B-F glass-ceramic sealant (solid oxide fuel cell). Mater Today Energy 2020;18:100535. https://doi.org/10.1016/j.mtener.2020.100535.

[171] Lahl N, Singheiser L, Hilpert K, Singh K, Bahadur D. Aluminosilicate glass ceramics as sealant in SOFC stacks. ECS Proc 1999;1999:1057.

[172] Jiang SP, Christiansen L, Hughan B, Foger K. Effect of glass sealant materials on microstructure and performance of Sr-doped LaMnO3 cathodes. J Mater Sci Lett 2001;20:695–7.

[173] Maher RC, Duboviks V, Offer GJ, Kishimoto M, Brandon NP, Cohen LF. Raman spectroscopy of solid oxide fuel cells: technique overview and application to carbon deposition analysis. Fuel Cell 2013;13:455–69.

[174] Hajimolana SA, Hussain MA, Daud WMAW, Soroush M, Shamiri A. Mathematical modeling of solid oxide fuel cells: a review. Renew Sustain Energy Rev 2011;15:1893–917. https://doi.org/10.1016/j.rser.2010.12.011.

[175] Kakaç S, Pramuanjaroenkij A, Zhou XY. A review of numerical modeling of solid oxide fuel cells. Int J Hydrogen Energy 2007;32:761–86. https://doi.org/10.1016/j.ijhydene.2006.11.028.

[176] Asghar MI, Yao X, Jouttijärvi S, Hochreiner E, Virta R, Lund PD. Intriguing electrochemistry in low-temperature single layer ceramic fuel cells based on CuFe2O4. Int J Hydrogen Energy 2020;45:24083–92. https://doi.org/10.1016/j.ijhydene.2019.09.175.

[177] Kasyanova AV, Tarutina LR, Rudenko AO, Lyagaeva JG, Medvedev DA. Ba (Ce, Zr) O3-based electrodes for protonic ceramic electrochemical cells: towards highly compatible functionality and triple-conducting behavior. Russ Chem Rev 2020;89:667.

[178] Wang R, Sun Z, Pal UB, Gopalan S, Basu SN. Mitigation of chromium poisoning of cathodes in solid oxide fuel cells employing CuMn1.8O4 spinel coating on metallic interconnect. J Power Sources 2018;376:100–10. https://doi.org/10.1016/j.jpowsour.2017.11.069.

[179] Gazzarri JI, Kesler O. Short-stack modeling of degradation in solid oxide fuel cells: Part I. Contact degradation. J Power Sources 2008;176:138–54. https://doi.org/10.1016/j.jpowsour.2007.10.047.

[180] Yang B, Guo Z, Wang J, Wang J, Zhu T, Shu H, et al. Solid oxide fuel cell systems fault diagnosis: critical summarization, classification, and perspectives. J Energy Storage 2021;34:102153. https://doi.org/10.1016/j.est.2020.102153.

[181] Li J, Li J, Yan D, Pu J, Chi B, Jian L. Promoted Cr-poisoning tolerance of La2NiO4+δ-coated PrBa0.5Sr0.5Co1.5Fe0.5O5+δ cathode for intermediate temperature solid oxide fuel cells. Electrochim Acta 2018;270:294–301. https://doi.org/10.1016/j.electacta.2018.03.053.

[182] Subotić V, Stoeckl B, Lawlor V, Strasser J, Schroettner H, Hochenauer C. Towards a practical tool for online monitoring of solid oxide fuel cell operation: an experimental study and application of advanced data analysis approaches. Appl Energy 2018;222:748–61. https://doi.org/10.1016/j.apenergy.2018.03.182.

[183] Wei T, Qiu P, Yang J, Jia L, Chi B, Pu J, et al. High-performance direct carbon dioxide-methane solid oxide fuel cell with a structure-engineered double-layer anode. J Power Sources 2021;484:229199. https://doi.org/10.1016/j.jpowsour.2020.229199.

[184] Halinen M. Improving the performance of solid oxide fuel cell systems. 2015.

[185] Lee S, Choi J, Shin D. Microstructural stability of SSC fibrous cathode with embedded SDC particles for solid oxide fuel cells operating on hydrogen. Int J Hydrogen Energy 2018;43:11372–7. https://doi.org/10.1016/j.ijhydene.2018.03.041.

[186] Lu X, Faguy PW, Liu M. In situ potential-dependent FTIR emission spectroscopy: a novel probe for high temperature fuel cell interfaces. J Electrochem Soc 2002;149:A1293.

[187] Yokokawa H, Yamaji K, Brito ME, Kishimoto H, Horita T. General considerations on degradation of Solid Oxide Fuel Cell anodes and cathodes due to impurities in gases. J Power Sources 2011;196:7070–5. https://doi.org/10.1016/j.jpowsour.2010.07.093.

[188] Ploner A, Hagen A, Hauch A. Classical statistical methodology for accelerated testing of solid oxide fuel cells. J Power Sources 2018;395:379–85. https://doi.org/10.1016/j.jpowsour.2018.05.034.

[189] Pomfret MB, Owrutsky JC, Walker RA. In situ optical studies of solid-oxide fuel cells. Annu Rev Anal Chem 2010;3:151–74.

[190] Shearing P, Bradley R, Tariq F, Gelb J, Withers P, Brandon N. ECS meet. Abstr. In: In situ characterization of solid-oxide fuel cell electrode microstructure during high-temperature operation using X-ray computed nanotomography. IOP Publishing; 2011. p. 319.

[191] Blinn KS, Abernathy H, Li X, Liu M, Bottomley LA, Liu M. Raman spectroscopic monitoring of carbon deposition on hydrocarbon-fed solid oxide fuel cell anodes. Energy Environ Sci 2012;5:7913–7.

[192] Pomfret MB, Owrutsky JC, Walker RA. High-temperature Raman spectroscopy of solid oxide fuel cell materials and processes. J Phys Chem B 2006;110:17305–8.

[193] Eigenbrodt BC, Pomfret MB, Steinhurst DA, Owrutsky JC, Walker RA. Direct, in situ optical studies of Ni− YSZ anodes in solid oxide fuel cells operating with methanol and methane. J Phys Chem C 2011;115:2895–903.

[194] Kirtley JD, Steinhurst DA, Owrutsky JC, Pomfret MB, Walker RA. In situ optical studies of methane and simulated biogas oxidation on high temperature solid oxide fuel cell anodes. Phys Chem Chem Phys 2014;16:227–36.

[195] Kirtley J, Singh A, Halat D, Oswell T, Hill JM, Walker RA. In situ Raman studies of carbon removal from high temperature Ni–YSZ cermet anodes by gas phase reforming agents. J Phys Chem C 2013;117:25908–16.

[196] Pomfret MB, Marda J, Jackson GS, Eichhorn BW, Dean AM, Walker RA. Hydrocarbon fuels in solid oxide fuel cells: in situ Raman studies of graphite formation and oxidation. J Phys Chem C 2008;112:5232–40.

[197] Maher RC, Cohen LF, Lohsoontorn P, Brett DJL, Brandon NP. Raman spectroscopy as a probe of temperature and oxidation state for gadolinium-doped ceria used in solid oxide fuel cells. J Phys Chem 2008;112:1497–501.

[198] Eigenbrodt BC, Walker RA. High temperature mapping of surface electrolyte oxide concentration in solid oxide fuel cells with vibrational Raman spectroscopy. Anal Methods 2011;3:1478–84.

[199] Marina OA, Coyle CA, Engelhard MH, Pederson LR. Mitigation of sulfur poisoning of Ni/Zirconia SOFC anodes by antimony and tin. J Electrochem Soc 2011;158:B424.

[200] Cheng Z, Liu M. Characterization of sulfur poisoning of Ni–YSZ anodes for solid oxide fuel cells using in situ Raman microspectroscopy. Solid State Ionics 2007;178:925–35. https://doi.org/10.1016/j.ssi.2007.04.004.

[201] Cheng Z, Abernathy H, Liu M. Raman spectroscopy of nickel sulfide Ni3S2. J Phys Chem C 2007;111:17997–8000.

[202] Li X, Blinn K, Chen D, Liu M. In situ and surface-enhanced Raman spectroscopy study of electrode materials in solid oxide fuel cells. Electrochem Energy Rev 2018;1:433–59.

[203] Niu B, Jin F, Yang X, Feng T, He T. Resisting coking and sulfur poisoning of double perovskite Sr2TiFe0.5Mo0.5O6–δ anode material for solid oxide fuel cells. Int J Hydrogen Energy 2018;43:3280–90. https://doi.org/10.1016/j.ijhydene.2017.12.134.

[204] Feng T, Niu B, Liu J, He T. Sr- and Mo-deficiency Sr1.95TiMo1−xO6–δ double perovskites as anodes for solid-oxide fuel cells using H2S-containing syngas. Int J Hydrogen Energy 2020;45:23444–54. https://doi.org/10.1016/j.ijhydene.2020.06.115.

[205] Niu B, Jin F, Fu R, Feng T, Shen Y, Liu J, et al. Pd-impregnated Sr1.9VMoO6–δ double perovskite as an efficient and stable anode for solid-oxide fuel cells operating on sulfur-containing syngas. Electrochim Acta 2018;274:91–102. https://doi.org/10.1016/j.electacta.2018.04.066.

[206] Niu B, Jin F, Liu J, Zhang Y, Jiang P, Feng T, et al. Highly carbon– and sulfur–tolerant Sr2TiMoO6−δ double perovskite anode for solid oxide fuel cells. Int J Hydrogen Energy 2019;44:20404. https://doi.org/10.1016/j.ijhydene.2019.06.023. –15.

[207] Handal HT, Thangadurai V. Evaluation of chemical stability, thermal expansion coefficient, and electrical properties of solid state and wet-chemical synthesized Y and Mn-codoped CeO2 for solid oxide fuel cells. J Power Sources 2013;243:458–71.

[208] Reeping KW, Kirtley JD, Bohn JM, Steinhurst DA, Owrutsky JC, Walker RA. Chlorine-induced degradation in solid oxide fuel cells identified by operando optical methods. J Phys Chem C 2017;121:2588–96.

[209] Zhang Y, Gao X, Sunarso J, Liu B, Zhou W, Ni M, et al. Significantly improving the durability of single-chamber solid oxide fuel cells: a highly active CO2-resistant perovskite cathode. ACS Appl Energy Mater 2018;1:1337–43.

[210] Gu B, Sunarso J, Zhang Y, Song Y, Yang G, Zhou W, et al. A high performance composite cathode with enhanced CO2 resistance for low and intermediate-temperature solid oxide fuel cells. J Power Sources 2018;405:124–31.

[211] Kim SH, Shim KB, Kim CS, Chou JT, Oshima T, Shiratori Y, et al. Degradation of solid oxide fuel cell cathodes accelerated at a high water vapor concentration. J Fuel Cell Sci Technol 2010;7.

[212] Zhu Y, Sunarso J, Zhou W, Shao Z. Probing CO2 reaction mechanisms and effects on the SrNb0. 1Co0. 9− xFexO3− δ cathodes for solid oxide fuel cells. Appl Catal B Environ 2015;172:52–7.

[213] Benck JD, Rettenwander D, Jackson A, Young D, Chiang Y-M. Apparatus for operando x-ray diffraction of fuel electrodes in high temperature solid oxide electrochemical cells. Rev Sci Instrum 2019;90:23910.

[214] Jafari M, Salamati H, Zhiani M, Shahsavari E. Enhancement of an IT-SOFC cathode by introducing YSZ: electrical and electrochemical properties of La0.6Ca0.4Fe0.8Ni0.2O3-δ-YSZ composites. Int J Hydrogen Energy 2019;44:1953–66. https://doi.org/10.1016/j.ijhydene.2018.10.151.

[215] Wang Z, Yang Z, Song Y, Mao J, Liang F, Zhou W. Alkaline metal doped strontium cobalt ferrite perovskites as cathodes for intermediate-temperature solid oxide fuel cells. Int J Hydrogen Energy 2018;43:13420–9. https://doi.org/10.1016/j.ijhydene.2018.05.057.

[216] Niemczyk A, Olszewska A, Du Z, Zhang Z, Świerczek K, Zhao H. Assessment of layered La2-x(Sr,Ba)xCuO4-δ oxides as potential cathode materials for SOFCs. Int J Hydrogen Energy 2018;43:15492–504. https://doi.org/10.1016/j.ijhydene.2018.06.119.

[217] Wang J, Yang Z, Lv Y, Jiang F, Chen Y, Peng S. Effect of CO2 on La0.4Sr0.6Co0.2Fe0.7Nb0.1O3–δ cathode for solid oxide fuel cells. J Electroanal Chem 2019;847:113256. https://doi.org/10.1016/j.jelechem.2019.113256.

[218] Hong J, Heo SJ, Aphale AN, Hu B, Singh P. H2O absorption assisted Sr-segregation in strontium nickel oxide based chromium getter and encapsulation with SrCO3. J Electrochem Soc 2019;166:F59.

[219] Bu Y, Joo S, Zhang Y, Wang Y, Meng D, Ge X, et al. A highly efficient composite cathode for proton-conducting solid oxide fuel cells. J Power Sources 2020;451:227812. https://doi.org/10.1016/j.jpowsour.2020.227812.

[220] Dong F, Ni M, He W, Chen Y, Yang G, Chen D, et al. An efficient electrocatalyst as cathode material for solid oxide fuel cells: BaFe0·95Sn0·05O3−δ. J Power Sources 2016;326:459–65. https://doi.org/10.1016/j.jpowsour.2016.07.023.

[221] Simner SP, Anderson MD, Engelhard MH, Stevenson JW. Degradation mechanisms of La–Sr–Co–Fe–O3 SOFC cathodes. Electrochem Solid State Lett 2006;9:A478.

[222] Choi M, Ibrahim IAM, Kim K, Koo JY, Kim SJ, Son J-W, et al. Engineering of charged defects at perovskite oxide surfaces for exceptionally stable solid oxide fuel cell electrodes. ACS Appl Mater Interfaces 2020;12:21494–504.

[223] Shaheen K, Suo H, Shah Z, Hanif MB, Hussain Z, Ali S, et al. Electrochemical performance of multifuel based nanocomposite for solid oxide fuel cell. Ceram Int 2020;46:8832–8. https://doi.org/10.1016/j.ceramint.2019.12.127.

[224] Go D, Yang BC, Shin JW, Kim HJ, Lee S, Kye S, et al. Atomic layer deposited YSZ overlayer on Ru for direct methane utilization in solid oxide fuel cell. Ceram Int 2020;46:1705–10. https://doi.org/10.1016/j.ceramint.2019.09.143.

[225] Jang DY, Koo J, Choi HR, Kim JW, Jeong HJ, Prinz FB, et al. Coke-free oxidation of methanol in solid oxide fuel cells with heterogeneous nickel–palladium catalysts prepared by atomic layer deposition. ACS Sustainable Chem Eng 2020;8:10529–35.

[226] Rehman SU, Shaur A, Song R-H, Lim T-H, Hong J-E, Park S-J, et al. Nano-fabrication of a high-performance LaNiO3 cathode for solid oxide fuel cells using an electrochemical route. J Power Sources 2019;429:97–104. https://doi.org/10.1016/j.jpowsour.2019.05.007.

[227] Bozzini B, Previdi A, Amati M, Bevilacqua M, Cordaro G, Corva M, et al. In situ near-ambient pressure X-ray photoelectron spectroscopy discloses the surface composition of operating NdBaCo2O5+δ solid oxide fuel cell cathodes. J Power Sources 2019;436:226815. https://doi.org/10.1016/j.jpowsour.2019.226815.

[228] Song K, Yu Z, Luo X, Zhu S, Yang Y, Yang Q, et al. A simple Ce-doping strategy to enhance stability of hybrid symmetrical electrode for solid oxide fuel cells. Int J Hydrogen Energy 2020.

[229] Feng Z, Crumlin EJ, Hong WT, Lee D, Mutoro E, Biegalski MD, et al. In situ studies of the temperature-dependent surface structure and chemistry of single-crystalline (001)-oriented La0. 8Sr0. 2CoO3− δ perovskite thin films. J Phys Chem Lett 2013;4:1512–8.

[230] Opitz AK, Rameshan C, Kubicek M, Rupp GM, Nenning A, Götsch T, et al. The chemical evolution of the La 0.6 Sr 0.4 CoO 3− δ surface under SOFC operating conditions and its implications for electrochemical oxygen exchange activity. Top Catal 2018;61:2129–41.

[231] Horita T. Chromium poisoning for prolonged lifetime of electrodes in solid oxide fuel cells - Review. Ceram Int 2020. https://doi.org/10.1016/j.ceramint.2020.11.082.

[232] Wang H, Barnett SA. Sr surface segregation on La0. 6Sr0. 4Co0. 2Fe0. 8O3-δ porous solid oxide fuel cell cathodes. ECS Trans 2017;78:905.

[233] De Vero JC, Develos-Bagarinao K, Kishimoto H, Ishiyama T, Yamaji K, Horita T, et al. Enhanced stability of solid oxide fuel cells by employing a modified cathode-interlayer interface with a dense La0.6Sr0.4Co0.2Fe0.8O3-δ thin film. J Power Sources 2018;377:128–35. https://doi.org/10.1016/j.jpowsour.2017.12.010.

[234] Develos-Bagarinao K, Budiman RA, Liu S-S, Ishiyama T, Kishimoto H, Yamaji K. Evolution of cathode-interlayer interfaces and its effect on long-term degradation. J Power Sources 2020;453:227894. https://doi.org/10.1016/j.jpowsour.2020.227894.

[235] Kim SJ, Choi M-B, Park M, Kim H, Son J-W, Lee J-H, et al. Acceleration tests: degradation of anode-supported planar solid oxide fuel cells at elevated operating temperatures. J Power Sources 2017;360:284–93. https://doi.org/10.1016/j.jpowsour.2017.06.004.

[236] Tucker MC. Durability of symmetric-structured metal-supported solid oxide fuel cells. J Power Sources 2017;369:6–12. https://doi.org/10.1016/j.jpowsour.2017.09.075.

[237] Li Y, Na L, Lü Z, Li S. Sulfur poisoning and the regeneration of the solid oxide fuel cell with metal catalyst-impregnated La0. 75Sr0. 25Cr0. 5Mn0. 5O3-δ anode. Int J Hydrogen Energy 2020;45:15650–7.

[238] Lee JG, Jeon OS, Hwang HJ, Jang J, Lee Y, Hyun SH, et al. Durable and high-performance direct-methane fuel cells with coke-tolerant ceria-coated Ni catalysts at reduced temperatures. Electrochim Acta 2016;191:677–86.

[239] Song Y, Li H, Xu M, Yang G, Wang W, Ran R, et al. Infiltrated NiCo alloy nanoparticle decorated perovskite oxide: a highly active, stable, and antisintering anode for direct-ammonia solid oxide fuel cells. Small 2020;16:2001859.

[240] Sumi H, Shimada H, Yamaguchi Y, Yamaguchi T, Fujishiro Y. Degradation evaluation by distribution of relaxation times analysis for microtubular solid oxide fuel cells. Electrochim Acta 2020;339:135913.

[241] Li Y, Wang Z, Li J, Zhu X, Zhang Y, Huang X, et al. Sulfur poisoning and attempt of oxidative regeneration of La0.75Sr0.25Cr0.5Mn0.5O3−δ anode for solid oxide fuel cell. J Alloys Compd 2017;698:794–9. https://doi.org/10.1016/j.jallcom.2016.12.313.

[242] Torrell M, Morata A, Kayser P, Kendall M, Kendall K, Tarancón A. Performance and long term degradation of 7 W micro-tubular solid oxide fuel cells for portable applications. J Power Sources 2015;285:439–48. https://doi.org/10.1016/j.jpowsour.2015.03.030.

[243] Jony MR. A study of solid oxide fuel cell materials at high temperature using an environmental scanning electron microscope. 2017.

[244] Mehran MT, Khan MZ, Lim T-H, Lee S-B, Song R-H. Effect of nano-Al2O3 addition on mechanical durability of nickel-yttria stabilized zirconia anode support of solid oxide fuel cells. Ceram Int 2018;44:14824–33.

[245] Lee T-H, Park K-Y, Kim N-I, Song S-J, Hong K-H, Ahn D, et al. Robust NdBa0. 5Sr0. 5Co1. 5Fe0. 5O5+ δ cathode material and its degradation prevention operating logic for intermediate temperature-solid oxide fuel cells. J Power Sources 2016;331:495–506.

[246] Chen Y, Fan Y, Lee S, Hackett G, Abernathy H, Gerdes K, et al. Interface and grain boundary degradation in LSM-YSZ composite Solid Oxide Fuel Cell cathodes operated in humidified air. J Power Sources 2019;438:227043.

[247] Bucher E, Sitte W, Klauser F, Bertel E. Impact of humid atmospheres on oxygen exchange properties, surface-near elemental composition, and surface morphology of La0.6Sr0.4CoO3−δ. Solid State Ionics 2012;208:43–51. https://doi.org/10.1016/j.ssi.2011.12.005.

[248] Liu Y, Chi B, Pu J, Li J. Performance degradation of impregnated La0.6Sr0.4Co0.2Fe0.8O3+Y2O3 stabilized ZrO2 composite cathodes of intermediate temperature solid oxide fuel cells. Int J Hydrogen Energy 2012;37:4388–93. https://doi.org/10.1016/j.ijhydene.2011.11.151.

[249] Wilson JR, Kobsiriphat W, Mendoza R, Chen H-Y, Hiller JM, Miller DJ, et al. Three-dimensional reconstruction of a solid-oxide fuel-cell anode. Nat Mater 2006;5:541–4.

[250] Lee S, Lee S, Kim H-J, Choi SM, An H, Park MY, et al. Highly durable solid oxide fuel cells: suppressing chemical degradation via rational design of a diffusion-blocking layer. J Mater Chem 2018;6:15083–94.

[251] Bertei A, Ruiz-Trejo E, Kareh K, Yufit V, Wang X, Tariq F, et al. The fractal nature of the three-phase boundary: a heuristic approach to the degradation of nanostructured solid oxide fuel cell anodes. Nano Energy 2017;38:526–36.

[252] Harris WM, Lombardo JJ, Nelson GJ, Lai B, Wang S, Vila-Comamala J, et al. Three-dimensional microstructural imaging of sulfur poisoning-induced degradation in a Ni-YSZ anode of solid oxide fuel cells. Sci Rep 2014;4:1–7.

[253] Wankmüller F, Szász J, Joos J, Wilde V, Störmer H, Gerthsen D, et al. Correlative tomography at the cathode/electrolyte interfaces of solid oxide fuel cells. J Power Sources 2017;360:399–408.

[254] Yang X, Li R, Yang Y, Wen G, Tian D, Lu X, et al. Improving stability and electrochemical performance of Ba0. 5Sr0. 5Co0. 2Fe0. 8O3-δ electrode for symmetrical solid oxide fuel cells by Mo doping. J Alloys Compd 2020:154711.

[255] Zhang J, Li X, Zhang Z, Xu X, Chen Y, Song Y, et al. A new highly active and CO2-stable perovskite-type cathode material for solid oxide fuel cells developed from A- and B-site cation synergy. J Power Sources 2020;457:227995. https://doi.org/10.1016/j.jpowsour.2020.227995.

[256] Wang R, Würth M, Pal UB, Gopalan S, Basu SN. Roles of humidity and cathodic current in chromium poisoning of Sr-doped LaMnO3-based cathodes in solid oxide fuel cells. J Power Sources 2017;360:87–97. https://doi.org/10.1016/j.jpowsour.2017.06.005.

[257] Wang J, Fu L, Yang J, Wu K, Zhou J, Wu K. Cerium and ruthenium co-doped La0.7Sr0.3FeO3–δ as a high-efficiency electrode for symmetrical solid oxide fuel cell. J Rare Earths 2021. https://doi.org/10.1016/j.jre.2021.01.009.

[258] Asghar MI, Heikkilä M, Lund PD. Advanced low-temperature ceramic nanocomposite fuel cells using ultra high ionic conductivity electrolytes synthesized through freeze-dried method and solid-route. Mater Today Energy 2017;5:338–46.

[259] Lu H, Kim JP, Son SH, Park JH. Novel SrCo1− 2x (Fe, Nb) xO3− δ (x= 0.05, 0.10) oxides targeting CO2 capture and O2 enrichment: structural stability and oxygen sorption properties. Mater Lett 2011;65:2858–60.

[260] Amarsingh Bhabu K, Theerthagiri J, Madhavan J, Balu T, Rajasekaran TR. Superior oxide ion conductivity of novel acceptor doped cerium oxide electrolytes for intermediate-temperature solid oxide fuel cell applications. J Phys Chem C 2016;120:18452–61.

[261] Skutina LS, Vylkov AA, Kuznetsov DK, Medvedev DA, Shur VY. Tailoring Ni and Sr2Mg0. 25Ni0. 75MoO6− δ cermet compositions for designing the fuel electrodes of solid oxide electrochemical cells. Energies 2019;12:2394.

[262] Zhang Y, Chen B, Guan D, Xu M, Ran R, Ni M, et al. Thermal-expansion offset for high-performance fuel cell cathodes. Nature 2021;591:246–51.

[263] Khan MZ, Mehran MT, Song R-H, Lee S-B, Lim T-H. Effects of applied current density and thermal cycling on the degradation of a solid oxide fuel cell cathode. Int J Hydrogen Energy 2018;43:12346–57. https://doi.org/10.1016/j.ijhydene.2018.04.175.

[264] Öztürk B, Topcu A, Öztürk S, Cora ÖN. Oxidation, electrical and mechanical properties of Crofer®22 solid oxide fuel cell metallic interconnects manufactured through powder metallurgy. Int J Hydrogen Energy 2018;43:10822–33. https://doi.org/10.1016/j.ijhydene.2018.01.078.

[265] Li R, Liang X, Wang X, Zeng W, Yang J, Yan D, et al. Improvement of sealing performance for Al2O3 fiber-reinforced compressive seals for intermediate temperature solid oxide fuel cell. Ceram Int 2019;45:21953. https://doi.org/10.1016/j.ceramint.2019.07.209. –9.

[266] Celik S, Timurkutluk B, Toros S, Timurkutluk C. Mechanical and electrochemical behavior of novel electrolytes based on partially stabilized zirconia for solid oxide fuel cells. Ceram Int 2015;41:8785–90. https://doi.org/10.1016/j.ceramint.2015.03.104.

[267] Timurkutluk B, Dokuyucu S. The role of tape thickness on mechanical properties and performance of electrolyte supports in solid oxide fuel cells. Ceram Int 2018;44:17399–406. https://doi.org/10.1016/j.ceramint.2018.06.205.

[268] Morales M, Laguna-Bercero MA. Influence of anode functional layers on electrochemical performance and mechanical strength in microtubular solid oxide fuel cells fabricated by gel-casting. ACS Appl Energy Mater 2018;1:2024–31.

[269] Spivey BJ, Edgar TF. Dynamic modeling, simulation, and MIMO predictive control of a tubular solid oxide fuel cell. J Process Control 2012;22:1502–20. https://doi.org/10.1016/j.jprocont.2012.01.015.

[270] Zheng Y, Wu X, Zhao D, Xu Y, Wang B, Zu Y, et al. Data-driven fault diagnosis method for the safe and stable operation of solid oxide fuel cells system. J Power Sources 2021;490:229561. https://doi.org/10.1016/j.jpowsour.2021.229561.

[271] Fu Q, Li Z, Wei W, Liu F, Xu X, Liu Z. Performance degradation prediction of direct internal reforming solid oxide fuel cell due to Ni-particle coarsening in composite anode. Energy Convers Manag 2021;233:113902.

[272] Kim DH, Bae Y, Lee S, Son J-W, Shim JH, Hong J. Thermal analysis of a 1-kW hydrogen-fueled solid oxide fuel cell stack by three-dimensional numerical simulation. Energy Convers Manag 2020;222:113213. https://doi.org/10.1016/j.enconman.2020.113213.

[273] Bove R, Ubertini S. Modeling solid oxide fuel cells: methods, procedures and techniques. Springer Science & Business Media; 2008.

[274] Li A, Song C, Lin Z. A multiphysics fully coupled modeling tool for the design and operation analysis of planar solid oxide fuel cell stacks. Appl Energy 2017;190:1234–44. https://doi.org/10.1016/j.apenergy.2017.01.034.

[275] Zhu J, Lin Z. Degradations of the electrochemical performance of solid oxide fuel cell induced by material microstructure evolutions. Appl Energy 2018;231:22–8. https://doi.org/10.1016/j.apenergy.2018.09.127.

[276] Anjum U, Agarwal M, Khan TS, Haider MA. Mechanistic elucidation of surface cation segregation in double perovskite PrBaCo 2 O 5+ δ material using MD and DFT simulations for solid oxide fuel cells. Ionics 2020;26:1307–14.

[277] Xu H, Chen B, Tan P, Xuan J, Maroto-Valer MM, Farrusseng D, et al. Modeling of all-porous solid oxide fuel cells with a focus on the electrolyte porosity design. Appl Energy 2019;235:602–11. https://doi.org/10.1016/j.apenergy.2018.10.069.

[278] Wang CC, Darvish S, Chen K, Hou B, Zhang Q, Tan Z, et al. Combined Cr and S poisoning of La0.8Sr0.2MnO3-δ (LSM) cathode of solid oxide fuel cells. Electrochim Acta 2019;312:202–12. https://doi.org/10.1016/j.electacta.2019.04.116.

[279] Darvish S, Wang CC, Jiang SP, Zhong Y. Thermodynamic stability mapping and electrochemical study of La1-xSrxCo0.2Fe0.8O3±δ (x=0.2–0.4) as a cathode of solid oxide fuel cells in the presence of SO2. Electrochim Acta 2018;287:68–77. https://doi.org/10.1016/j.electacta.2018.04.039.

[280] Xu M, Li TS, Yang M, Andersson M, Fransson I, Larsson T, et al. Modeling of an anode supported solid oxide fuel cell focusing on thermal stresses. Int J Hydrogen Energy 2016;41:14927–40. https://doi.org/10.1016/j.ijhydene.2016.06.171.

[281] Saied M, Ahmed K, Ahmed M, Nemat-Alla M, El-Sebaie M. Investigations of solid oxide fuel cells with functionally graded electrodes for high performance and safe thermal stress. Int J Hydrogen Energy 2017;42:15887–902. https://doi.org/10.1016/j.ijhydene.2017.05.071.

[282] Osman S, Ahmed K, Ahmed M. Performance of two-dimensional functionally graded anode supported solid-oxide fuel cells. Energy Sustain 2021;84881. American Society of Mechanical Engineers V001T04A001.

[283] Hwang B, Kwon H, Ko J, Kim B-K, Han JW. Density functional theory study for the enhanced sulfur tolerance of Ni catalysts by surface alloying. Appl Surf Sci 2018;429:87–94. https://doi.org/10.1016/j.apsusc.2017.06.164.

[284] Guo M, Lin Z. Long-term evolution of mechanical performance of solid oxide fuel cell stack and the underlying mechanism. Int J Hydrogen Energy 2021;46:24293–304. https://doi.org/10.1016/j.ijhydene.2021.04.196.

[285] Babaie Rizvandi O, Miao X-Y, Frandsen HL. Multiscale modeling of degradation of full solid oxide fuel cell stacks. Int J Hydrogen Energy 2021;46:27709–30. https://doi.org/10.1016/j.ijhydene.2021.05.204.

[286] Kaur G, Homa D, Singh K, Pandey OP, Scott B, Pickrell G. Simulation of thermal stress within diffusion couple of composite seals with Crofer 22APU for solid oxide fuel cells applications. J Power Sources 2013;242:305–13. https://doi.org/10.1016/j.jpowsour.2013.05.094.

[287] Yan Z, He A, Hara S, Shikazono N. Modeling of solid oxide fuel cell (SOFC) electrodes from fabrication to operation: microstructure optimization via artificial neural networks and multi-objective genetic algorithms. Energy Convers Manag 2019;198:111916. https://doi.org/10.1016/j.enconman.2019.111916.

[288] Yan Z, He A, Hara S, Shikazono N. Modeling of solid oxide fuel cell (SOFC) electrodes from fabrication to operation: correlations between microstructures and electrochemical performances. Energy Convers Manag 2019;190:1–13. https://doi.org/10.1016/j.enconman.2019.04.002.

[289] Wang Y, Wu C, Du Q, Ni M, Jiao K, Zu B. Morphology and performance evolution of anode microstructure in solid oxide fuel cell: a model-based quantitative analysis. Appl Energy Combust Sci 2021;5:100016. https://doi.org/10.1016/j.jaecs.2020.100016.

[290] Offer GJ, Mermelstein J, Brightman E, Brandon NP. Thermodynamics and kinetics of the interaction of carbon and sulfur with solid oxide fuel cell anodes. J Am Ceram Soc 2009;92:763–80.

[291] Savioli J, Watson GW. Computational modelling of solid oxide fuel cells. Curr Opin Electrochem 2020;21:14–21. https://doi.org/10.1016/j.coelec.2019.12.007.

[292] Boldrin P, Ruiz-Trejo E, Mermelstein J, Bermúdez Menéndez JM, Ramírez Reina T, Brandon NP. Strategies for carbon and sulfur tolerant solid oxide fuel cell materials, incorporating lessons from heterogeneous catalysis. Chem Rev 2016;116:13633–84.

[293] Wang C, Xu Z, Koeppel B. A discrete element model simulation of structure and bonding at interfaces between cathode and cathode contact paste in solid oxide fuel cells. Renew Energy 2020;157:998–1007. https://doi.org/10.1016/j.renene.2020.05.111.

[294] Darvish S, Hu B, Singh P, Zhong Y. Thermodynamic and experimental evaluation of La 1− x Sr x MnO 3±δ cathode in presence of Cr-containing humidified air. JOM 2019;71:3814–24.

[295] Lee JG, Park JH, Shul YG. Tailoring gadolinium-doped ceria-based solid oxide fuel cells to achieve 2 W cm−2 at 550 °C. Nat Commun 2014;5:4045. https://doi.org/10.1038/ncomms5045.

[296] Yun B-H, Kim KJ, Joh DW, Chae MS, Lee JJ, Kim D, et al. Highly active and durable double-doped bismuth oxide-based oxygen electrodes for reversible solid oxide cells at reduced temperatures. J Mater Chem 2019;7:20558–66.

[297] Thaheem I, Kim KJ, Lee JJ, Joh DW, Jeong I, Lee KT. High performance Mn 1.3 Co 1.3 Cu 0.4 O 4 spinel based composite cathodes for intermediate temperature solid oxide fuel cells. J Mater Chem 2019;7:19696–703.

[298] Joh DW, Park JH, Kim D, Wachsman ED, Lee KT. Functionally graded bismuth oxide/zirconia bilayer electrolytes for high-performance intermediate-temperature solid oxide fuel cells (IT-SOFCs). ACS Appl Mater Interfaces 2017;9:8443–9.

[299] Ren H, Lee YH, Wu EA, Chung H, Meng YS, Fullerton EE, et al. Nano-ceramic cathodes via Co-sputtering of Gd–Ce alloy and lanthanum strontium cobaltite for low-temperature thin-film solid oxide fuel cells. ACS Appl Energy Mater 2020;3:8135–42. https://doi.org/10.1021/acsaem.0c01147.

[300] Dogdibegovic E, Wang R, Lau GY, Tucker MC. High performance metal-supported solid oxide fuel cells with infiltrated electrodes. J Power Sources 2019;410–411:91–8. https://doi.org/10.1016/j.jpowsour.2018.11.004.

[301] Lee YH, Ren H, Wu EA, Fullerton EE, Meng YS, Minh NQ. All-Sputtered, superior power density thin-film solid oxide fuel cells with a novel nanofibrous ceramic cathode. Nano Lett 2020;20:2943–9. https://doi.org/10.1021/acs.nanolett.9b02344.

[302] Lee KT, Lidie AA, Yoon HS, Wachsman ED. Rational design of lower-temperature solid oxide fuel cell cathodes via nanotailoring of Co-assembled composite structures. Angew Chem Int Ed 2014;53:13463–7. https://doi.org/10.1002/anie.201408210.

[303] Yamaguchi Y, Kagomiya I, Minami S, Shimada H, Sumi H, Ogura Y, et al. La0.65Ca0.35FeO3-δ as a novel Sr- and Co-free cathode material for solid oxide fuel cells. J Power Sources 2020;448:227426. https://doi.org/10.1016/j.jpowsour.2019.227426.

[304] Sunarso J, Hashim SS, Zhu N, Zhou W. Perovskite oxides applications in high temperature oxygen separation, solid oxide fuel cell and membrane reactor: a review. Prog Energy Combust Sci 2017;61:57–77.

[305] Green MA, Ho-Baillie A, Snaith HJ. The emergence of perovskite solar cells. Nat Photonics 2014;8:506–14.

[306] Hashim SS, Liang F, Zhou W, Sunarso J. Cobalt-free perovskite cathodes for solid oxide fuel cells. Chemelectrochem 2019;6:3549–69.

[307] Afroze S, Karim A, Cheok Q, Eriksson S, Azad AK. Latest development of double perovskite electrode materials for solid oxide fuel cells: a review. Front Energy 2019;13:770–97.

[308] Kaur P, Singh K. Review of perovskite-structure related cathode materials for solid oxide fuel cells. Ceram Int 2020;46:5521–35.

[309] Yang Y, Wang Y, Yang Z, Lei Z, Jin C, Liu Y, et al. Co-substituted Sr2Fe1.5Mo0.5O6-δ as anode materials for solid oxide fuel cells: achieving high performance via nanoparticle exsolution. J Power Sources 2019;438:226989. https://doi.org/10.1016/j.jpowsour.2019.226989.

[310] Li J, Fu Z, Wei B, Su C, Yue X, Lü Z. Tailoring tantalum doping into a perovskite ferrite to obtain a highly active and stable anode for solid oxide fuel cells. J Mater Chem 2020.

[311] Lu F, Xia T, Li Q, Sun L, Huo L, Zhao H. Ta-doped PrBa0.94Co2-xTaxO5+δ as promising oxygen electrodes: a focused study on catalytic oxygen reduction reaction activity, stability and CO2-durability. J Power Sources 2019;417:42–52. https://doi.org/10.1016/j.jpowsour.2019.02.009.

[312] Gao J, Li Q, Sun L, Huo L, Zhao H. Enhanced electrocatalytic activity and CO2 tolerant Bi0.5Sr0.5Fe1-xTaxO3-δ as cobalt-free cathode for intermediate-temperature solid oxide fuel cells. Ceram Int 2019;45:20226–33. https://doi.org/10.1016/j.ceramint.2019.06.295.

[313] Lu X, Yang Y, Ding Y, Chen Y, Gu Q, Tian D, et al. Mo-doped Pr0. 6Sr0. 4Fe0. 8Ni0. 2O3-δ as potential electrodes for intermediate-temperature symmetrical solid oxide fuel cells. Electrochim Acta 2017;227:33–40.

[314] Zhang P, Guan G, Khaerudini DS, Hao X, Xue C, Han M, et al. Mo doped Pr0. 4Sr0. 6Co0. 2Fe0. 8O3-δ cathode material with high catalytic activity for intermediate-temperature solid oxide fuel cells. Electrochim Acta 2014;146:591–7.

[315] Liu Y, Zhou F, Chen X, Wang C, Zhong S. Enhanced electrochemical activity and stability of LSCF cathodes by Mo doping for intermediate temperature solid oxide fuel cells. J Appl Electrochem 2021;51:425–33.

[316] Lu C, Niu B, Yu S, Yi W, Luo S, Xu B, et al. Efficient and stable symmetrical electrode La0. 6Sr0. 4Co0. 2Fe0. 7Mo0. 1O3–δ for direct hydrocarbon solid oxide fuel cells. Electrochim Acta 2019;323:134857.

[317] Zhang Z, Chen Y, Tade MO, Hao Y, Liu S, Shao Z. Tin-doped perovskite mixed conducting membrane for efficient air separation. J Mater Chem 2014;2:9666–74.

[318] Qian B, Chen Y, Tade MO, Shao Z. BaCo 0.6 Fe 0.3 Sn 0.1 O 3− δ perovskite as a new superior oxygen reduction electrode for intermediate-to-low temperature solid oxide fuel cells. J Mater Chem 2014;2:15078–86.

[319] Xia W, Li Q, Sun L, Huo L, Zhao H. Electrochemical performance of Sn-doped Bi0.5Sr0.5FeO3-δ perovskite as cathode electrocatalyst for solid oxide fuel cells. J Alloys Compd 2020;835:155406. https://doi.org/10.1016/j.jallcom.2020.155406.

[320] Xiang W, Wang J, Li S, Xia T, Wang G. Positive effects of calcium-doping on the cathode performance of layered perovskite Eu1-xCaxBaCo2O5+δ for intermediate-temperature solid oxide fuel cells. J Alloys Compd 2019;801:220–8. https://doi.org/10.1016/j.jallcom.2019.06.143.

[321] Zhu J, Guo S, Chu Z, Jin W. CO 2-tolerant oxygen-permeable perovskite-type membranes with high permeability. J Mater Chem 2015;3:22564–73.

[322] Zhang Z, Chen D, Wang J, Tan S, Yu X, Shao Z. Highly active and stable cobalt-free hafnium-doped SrFe0. 9Hf0. 1O3− δ perovskite cathode for solid oxide fuel cells. ACS Appl Energy Mater 2018;1:2134–42.

[323] Rehman AU, Li M, Knibbe R, Khan MS, Peterson VK, Brand HEA, et al. Enhancing oxygen reduction reaction activity and CO2 tolerance of cathode for low-temperature solid oxide fuel cells by in situ formation of carbonates. ACS Appl Mater Interfaces 2019;11:26909–19. https://doi.org/10.1021/acsami.9b07668.

[324] Bedon A, Rieu M, Viricelle J-P, Glisenti A. Rational development of IT-SOFC electrodes based on the nanofunctionalization of La0. 6Sr0. 4Ga0. 3Fe0. 7O3 with oxides. PART 1: cathodes by means of iron oxide. ACS Appl Energy Mater 2018;1:6840–50.

[325] Li J, Hou J, Lu Y, Wang Q, Xi X, Fan Y, et al. Ca-containing Ba0·95Ca0·05Co0·4Fe0·4Zr0·1Y0·1O3-δ cathode with high CO2-poisoning tolerance for proton-conducting solid oxide fuel cells. J Power Sources 2020;453:227909. https://doi.org/10.1016/j.jpowsour.2020.227909.

[326] Kim C, Lee H, Jang I, Kim S, Yoon H, Paik U, et al. Subcontinuous 2D La0. 6Sr0. 4CoO3-δ nanosheet as an efficient charge conductor for boosting the cathodic activity of solid oxide fuel cells. Electrochim Acta 2021;366:137371.

[327] Chen Y, Choi Y, Yoo S, Ding Y, Yan R, Pei K, et al. A highly efficient multi-phase catalyst dramatically enhances the rate of oxygen reduction. Joule 2018;2:938–49.

[328] Kan WH, Samson AJ, Thangadurai V. Trends in electrode development for next generation solid oxide fuel cells. J Mater Chem 2016;4:17913–32.

[329] Neagu D, Tsekouras G, Miller DN, Ménard H, Irvine JTS. In situ growth of nanoparticles through control of non-stoichiometry. Nat Chem 2013;5:916–23.

[330] Zhu T, Troiani HE, Mogni LV, Han M, Barnett SA. Ni-substituted Sr (Ti, Fe) O3 SOFC anodes: achieving high performance via metal alloy nanoparticle exsolution. Joule 2018;2:478–96.

[331] Fan W, Sun Z, Bai Y, Wu K, Zhou J, Cheng Y. In situ growth of nanoparticles in A-site deficient ferrite perovskite as an advanced electrode for symmetrical solid oxide fuel cells. J Power Sources 2020;456:228000.

[332] Fan W, Sun Z, Bai Y, Wu K, Cheng Y. Highly stable and efficient perovskite ferrite electrode for symmetrical solid oxide fuel cells. ACS Appl Mater Interfaces 2019; 11:23168–79.

[333] Lu F, Xia T, Li Q, Wang J, Huo L, Zhao H. Heterostructured simple perovskite nanorod-decorated double perovskite cathode for solid oxide fuel cells: highly catalytic activity, stability and CO2-durability for oxygen reduction reaction. Appl Catal B Environ 2019;249:19–31.

[334] Wang H, Zhang W, Guan K, Wei Z, Meng J, Meng J, et al. Enhancing activity and durability of A-site-deficient (La0.6Sr0.4)0.95Co0.2Fe0.8O3−δ cathode by surface modification with PrO2−δ nanoparticles. ACS Sustainable Chem Eng 2020;8:3367–80. https://doi.org/10.1021/acssuschemeng.9b07354.

[335] Ozmen O, Lee S, Hackett G, Abernathy H, Zondlo JW, Sabolsky EM. Efficient and controlled nano-catalyst solid-oxide fuel cell electrode infiltration with poly-norepinephrine surface modification. J Power Sources 2021;485:229232. https://doi.org/10.1016/j.jpowsour.2020.229232.

[336] Chen J, Yang X, Wan D, Li B, Lei L, Tian T, et al. Novel structured Sm0. 5Sr0. 5CoO3-δ cathode for intermediate and low temperature solid oxide fuel cells. Electrochim Acta 2020:136031.

[337] Muhoza SP, Lee S, Song X, Guan B, Yang T, Gross MD. Enhancing activity, charge transport, power production, and stability of commercial solid oxide fuel cells with yttria-stabilized zirconia nanoparticles. J Electrochem Soc 2020;167:24517.

[338] Qiu P, Lin J, Lei L, Yuan Z, Jia L, Li J, et al. Evaluation of Cr-tolerance of the Sr2Fe1.5Mo0.5O6−δ cathode for solid oxide fuel cells. ACS Appl Energy Mater 2019;2:7619–27. https://doi.org/10.1021/acsaem.9b01605.

[339] Qiu P, Li J, Jia L, Chi B, Pu J, Li J, et al. LaCoO3-δ coated Ba0.5Sr0.5Co0.8Fe0.2O3-δ cathode for intermediate temperature solid oxide fuel cells. Electrochim Acta 2019;319:981–9. https://doi.org/10.1016/j.electacta.2019.07.054.

[340] Qiu P, Yang X, Wang W, Wei T, Lu Y, Lin J, et al. Redox-reversible electrode material for direct hydrocarbon solid oxide fuel cells. ACS Appl Mater Interfaces 2020;12:13988. https://doi.org/10.1021/acsami.0c00922. –95.

[341] Tan T, Qin M, Li K, Zhou M, Liu T, Yang C, et al. In-situ exsolved NiFe alloy nanoparticles on Pr0.8Sr1.2(NiFe)O4-δ for direct hydrocarbon fuel solid oxide fuel cells. Int J Hydrogen Energy 2020. https://doi.org/10.1016/j.ijhydene.2020.07.250.

[342] Park JS, Choi HJ, Han GD, Koo J, Kang EH, Kim DH, et al. High–performance protonic ceramic fuel cells with a PrBa0. 5Sr0. 5Co1. 5Fe0. 5O5+ δ cathode with palladium–rich interface coating. J Power Sources 2021;482:229043.

[343] Kim SJ, Choi M, Lee J, Lee W. Modifying defect structures at interfaces for high-performance solid oxide fuel cells. J Eur Ceram Soc 2020;40:3089–97. https://doi.org/10.1016/j.jeurceramsoc.2020.03.009.

[344] Li J, Hou J, Lu Y, Wang Q, Xi X, Fan Y, et al. Ca-containing Ba0· 95Ca0· 05Co0· 4Fe0· 4Zr0· 1Y0· 1O3-δ cathode with high CO2-poisoning tolerance for proton-conducting solid oxide fuel cells. J Power Sources 2020;453:227909.

[345] Xu C, Sun W, Ren R, Yang X, Ma M, Qiao J, et al. A highly active and carbon-tolerant anode decorated with in situ grown cobalt nano-catalyst for intermediate-temperature solid oxide fuel cells. Appl Catal B Environ 2021;282: 119553.

[346] Yang Y, Bao H, Ni H, Ou X, Wang S, Lin B, et al. A novel facile strategy to suppress Sr segregation for high-entropy stabilized La0· 8Sr0· 2MnO3-δ cathode. J Power Sources 2021;482:228959.

[347] Zhang W, Zhou Y, Hussain AM, Song D, Miura Y, Chen Y, et al. High-performance, thermal cycling stable, coking-tolerant solid oxide fuel cells with nanostructured electrodes. ACS Appl Mater Interfaces 2021;13:4993–9.

[348] Zhang X, Xia T, Li Q, Sun L, Huo L, Zhao H. A highly active and CO2-tolerant perovskite cathode for solid oxide fuel cells operating below 700 °C. J Alloys Compd 2021;858:157743. https://doi.org/10.1016/j.jallcom.2020.157743.

[349] Xie D, Li K, Yang J, Yan D, Jia L, Chi B, et al. High-performance La0.5 (Ba0.75Ca0.25)0.5Co0.8Fe0.2O3-δ cathode for proton-conducting solid oxide fuel cells. Int J Hydrogen Energy 2021;46:10007–14. https://doi.org/10.1016/j.ijhydene.2020.01.014.

[350] da Silva AAA, Steil MC, Tabuti FN, Rabelo-Neto RC, Noronha FB, Mattos LV, et al. The role of the ceria dopant on Ni/doped-ceria anodic layer cermets for direct ethanol solid oxide fuel cell. Int J Hydrogen Energy 2021;46:4309–28. https://doi.org/10.1016/j.ijhydene.2020.10.155.

[351] He H, Huang X, Chen L. Sr-doped LaInO3 and its possible application in a single layer SOFC. Solid State Ionics 2000;130:183–93. https://doi.org/10.1016/S0167-2738(00)00666-4.

[352] Zhang W, Cai Y, Wang B, Xia C, Dong W, Li J, et al. Mixed ionic-electronic conductor membrane based fuel cells by incorporating semiconductor Ni0.8Co0.15Al0.05LiO2−δ into the Ce0.8Sm0.2O2−δ-Na2CO3 electrolyte. Int J Hydrogen Energy 2016;41:15346–53. https://doi.org/10.1016/j.ijhydene.2016.07.032.

[353] Jouttijärvi SV, Asghar MI, Lund PD. Investigation of factors affecting the performance of a single-layer nanocomposite fuel cell. Catal Today 2021;364: 104–10. https://doi.org/10.1016/j.cattod.2020.01.048.

[354] Lund PD, Zhu B, Li Y, Yun S, Nasibulin AG, Raza R, et al. Standardized procedures important for improving single-component ceramic fuel cell technology. ACS Energy Lett 2017;2:2752–5.

[355] Li P, Yang Q, Zhang H, Yao M, Yan F, Fu D. Effect of Fe, Ni and Zn dopants in La0·9Sr0·1CoO3 on the electrochemical performance of single-component solid oxide fuel cell. Int J Hydrogen Energy 2020;45:11802–13. https://doi.org/10.1016/j.ijhydene.2020.02.116.

[356] Zhu B, Fan L, Deng H, He Y, Afzal M, Dong W, et al. LiNiFe-based layered structure oxide and composite for advanced single layer fuel cells. J Power Sources 2016;316:37–43. https://doi.org/10.1016/j.jpowsour.2016.03.056.

[357] Xia C, Wang B, Ma Y, Cai Y, Afzal M, Liu Y, et al. Industrial-grade rare-earth and perovskite oxide for high-performance electrolyte layer-free fuel cell. J Power Sources 2016;307:270–9. https://doi.org/10.1016/j.jpowsour.2015.12.086.

[358] Deng H, Feng C, Zhang W, Mi Y, Wang X, Dong W, et al. The electrolyte-layer free fuel cell using a semiconductor-ionic Sr2Fe1.5Mo0.5O6-δ – Ce0.8Sm0.2O2-δ composite functional membrane. Int J Hydrogen Energy 2017;42:25001–7. https://doi.org/10.1016/j.ijhydene.2017.08.113.

[359] Gao J, Xu S, Akbar M, Xia C, Dong W, Liu C, et al. Single layer low-temperature SOFC based on Ce0.8Sm0.2O2-δ- La0.25Sr0.75Ti1O3-δ-Ni0.8Co0.15Al0.05LiO2-δ composite material. Int J Hydrogen Energy 2021;46:9775–81. https://doi.org/10.1016/j.ijhydene.2020.07.043.

[360] Hagen A, Barfod R, Hendriksen PV, Liu Y-L, Ramousse S. Degradation of anode supported SOFCs as a function of temperature and current load. J Electrochem Soc 2006;153:A1165.

[361] Fang Q, Frey CE, Menzler NH, Blum L. Electrochemical performance and preliminary post-mortem analysis of a solid oxide cell stack with 20,000 h of operation. J Electrochem Soc 2018;165:F38.

[362] Fang Q, Blum L, Stolten D. Electrochemical performance and degradation analysis of an SOFC short stack following operation of more than 100,000 hours. J Electrochem Soc 2019;166:F1320.

[363] Fang Q, Packbier U, Blum L. Long-term tests of a Jülich planar short stack with reversible solid oxide cells in both fuel cell and electrolysis modes. Int J Hydrogen Energy 2013;38:4281–90.

[364] Lashtabeg A, Skinner SJ. Solid oxide fuel cells—a challenge for materials chemists? J Mater Chem 2006;16:3161–70.